2-10 m Mid-infrared Supercontinuum Light Sources

Petersen, Christian Rosenberg

Publication date:
2016

Document Version
Publisher's PDF, also known as Version of record

DTU Fotonik
Department of Photonics Engineering

DTU

2-10 µm Mid-infrared Supercontinuum Light Sources

Ph.D. Dissertation

Christian Rosenberg Petersen

Department of Photonics Engineering
Technical University of Denmark

August 2016

TABLE OF CONTENTS

TABLE OF CONTENTS III
LIST OF ABBREVIATIONS VI

PREFACE VII

ACKNOWLEDGEMENTS VIII
ABSTRACT X
DANSK RESUMÉ (DANISH SUMMARY) XI
LIST OF PUBLICATIONS XII

INTRODUCTION 1

1.1 LIGHT AND FOOD 2
1.2 SCOPE AND OUTLINE 5

THEORY OF LIGHT-MATTER INTERACTION 5

2.1 LINEAR EFFECTS 6
2.1.1 ELECTRONIC RESPONSE 6
2.1.2 MOLECULAR RESPONSE 8
2.1.3 DISPERSION 11
2.1.4 OPTICAL ATTENUATION 12
2.1.5 OPTICAL AMPLIFICATION 13
2.2 LINEAR PULSE PROPAGATION IN OPTICAL FIBERS 15
2.2.1 MAXWELL'S EQUATIONS AND THE WAVE EQUATION 15
2.2.2 OPTICAL FIBERS AND PROPAGATION MODES 16
2.2.3 GROUP-VELOCITY DISPERSION 20
2.2.4 DISPERSIVE PULSE PROPAGATION 21
2.3 NONLINEAR EFFECTS 23
2.3.1 KERR EFFECT AND THE NONLINEAR SCHRÖDINGER EQUATION 24
2.3.2 SELF-PHASE AND CROSS-PHASE MODULATION 26
2.3.3 FOUR-WAVE MIXING 28
2.3.4 MODULATION INSTABILITY 30
2.3.5 RAMAN SCATTERING 31

2.3.6 Solitons and dispersive waves 34
2.4 The Generalized NLSE 36

MID-INFRARED OPTICAL FIBERS AND WAVEGUIDES 5

3.1 Mid-infrared materials and optical fibers 6
3.2 Optical fiber design 7
3.3 Waveguide dispersion measurements 9
3.3.1 Experimental results 11
3.4 Ultrafast laser inscribed waveguides 15
3.5 End-facet nanoimprint lithography 20
3.5.1 Experimental results 22
3.5.2 Nanoimprinting as a Tool for Fiber Inspection 28

SUPERCONTINUUM GENERATION IN CHALCOGENIDE FIBERS 5

4.1 Introduction 6
4.2 Megawatt-kilohertz pumping scheme 8
4.2.1 Introduction 8
4.2.2 Experimental results 11
4.2.3 Supercontinuum simulations 15
4.2.4 Conclusion 17
4.3 Kilowatt-Megahertz pumping scheme 19
4.3.1 Optical Parametric Generation 19
4.3.2 Step-Index Fiber 20
4.3.3 Suspended-Core Fiber 22
4.3.4 Photonic Crystal Fiber 25
4.4 Supercontinuum generation in tapered fibers 27
4.4.1 Introduction 27
4.4.2 Supercontinuum experiments 30
4.5 Cascaded supercontinuum generation 34
4.5.1 Introduction 34
4.5.2 Cascaded 2 μM laser pump scheme 35
4.5.3 Cascaded 1.55 μM Tm-Amplified laser pump scheme 38
4.5.4 Photonic Crystal Fiber 48
4.6 Summary and conclusion 50

APPLICATIONS IN SPECTROSCOPY AND IMAGING 5

5.1 INTRODUCTION 6
5.2 SKIN CANCER SCREENING 8
5.3 ULTRAFILTRATION MEMBRANES 12
5.4 LIQUID MILK 16

CONCLUSION AND OUTLOOK 5

STATE OF THE ART IN MID-IR SUPERCONTINUUM 7

REFERENCES 9

LIST OF ABBREVIATIONS

AR	Anti-reflection
AFM	Atomic force microscopy
BD-2	Black-diamond-2 (chalcogenide glass)
BW	Bandwidth
DW	Dispersive wave
FTIR	Fourier transform infrared (spectrometer)
FWM	Four-wave mixing
GLS	Gallium lanthanum sulphide
GNLSE	Generalized nonlinear Schrödinger Equation
GV	Group-velocity
GVD	Group-velocity dispersion
HOM	Higher-order mode
mid-IR	Mid-infrared
MOF	Microstructured optical fiber
NDFG	Non-collinear difference frequency generation
near-IR	Near-infrared
NIL	Nanoimprint lithography
NLSE	Nonlinear Schrödinger Equation
OPA	Optical parametric amplifier
OPG	Optical parametric generator
PCF	Photonic crystal fiber
SEM	Scanning electron microscopy
SC	Supercontinuum
SCG	Supercontinuum generation
SCF	Suspended-core fiber
SIF	Step-index fiber
SPM	Self-phase modulation
SRS	Stimulated Raman scattering
SSFS	Soliton self-frequency shift
THG	Third harmonic generation
TOD	Third-order dispersion
ULI	Ultrafast laser inscription
XPM	Cross-phase modulation
ZDW	Zero dispersion wavlength

Chapter X

Preface

"It is a capital mistake to theorize before one has data. Insensibly one begins to twist facts to suit theories, instead of theories to suit facts."

— Arthur Conan Doyle, Sherlock Holmes

This dissertation has been submitted to the Ph.D. school at the Department of Photonics Engineering as part of the requirements to obtain the degree of Ph.D. from the Technical University of Denmark.

The title of the dissertation is "2-10 μm mid-infrared supercontinuum sources", and it documents three years of Ph.D.-studies carried out at the Department of Photonics Engineering with professor Ole Bang as main supervisor, and with researcher Uffe Møller as co-supervisor during the first parts of the project. The project is part of the larger "Light and Food" project funded by the formerly Danish Advanced Technology Foundation (J.nr. 132-2012-3), which includes the project partners NKT Photonics, FOSS Analyticals, Copenhagen University (Department of Food Science), and Aarhus University (Department of Chemistry).

ACKNOWLEDGEMENTS

This dissertation and the work and results it represent would not have been possible without the contributions of all those involved. For this reason there are several key contributors that I would like to acknowledge.

First of all I would like to thank professor Ole Bang for giving me the opportunity to lead the group's activities in mid-infrared supercontinuum generation, and for giving me a large degree of freedom in which to operate and run the lab. It has meant great deal to me that I have been able to pursue different ideas without too much resistance, and to have such an experienced supervisor with a deeply theoretical background to balance the engineering experimentalist in me.

I would like to thank my current and former colleagues at DTU Fotonik: Binbin Zhou, Christos Markos, Irnis Kubat, and Uffe Møller, for not only assisting with invaluable help in technical matters, but also for making Fotonik a more fun place to work. Also, thanks to Jørgen Garnæs from DFM for taking time to help me with measurements on their atomic force microscope.

From NKT Photonics I would like to thank Peter Moselund for sharing his lab, time, and unique expertise with fiber optics and supercontinuum lasers with me, Christian Pedersen for his great help with my experiments at NKT, and Lasse Leick for his insights into project management and the commercial aspects of the technology.

I would also like to acknowledge our external chalcogenide fiber partners from Nottingham University, under Professor Angela Seddon, and from the company Selenoptics, Laurent Brilland and Johan Trolès, for whom without we would not have been able to demonstrate any of the results presented in this work.

During my studies I also had the pleasure of visiting Professor Moshe Tur at the Tel Aviv University in Israel, and I want to thank him and his group for their hospitality and help during my stay.

Also, the Innovation Fund Denmark and the remaining project partners within "Light and Food" deserves acknowledgement: Tine and Søren from KU Food for invaluable insights into the world of spectroscopy and chemometrics. Sune and Jacob from Aarhus for assisting me during my stay at the university, and Søren Keiding for always interesting comments and discussions. Thomas, Hans, Jonas, and Mikkel from

FOSS for invaluable discussions and input regarding spectroscopy on milk, and for lending us an FTIR instrument, which enabled us to extend our measurement capabilities.

Finally, I would like to say thank you to my loving and supportive wife Charlotte. Thank you for believing in me, for being proud of my achievements, and for supporting me throughout my studies.

ABSTRACT

Spectroscopy is the study of how light interacts with molecules, which can be used to identify various substances in for example foods and medicine, by observing which parts of the light is absorbed after interaction with the sample. Especially infrared light, more precisely the mid-infrared part of the spectrum, is of interest because almost all molecules display distinct absorption fingerprints in this region. Current instrumentation however relies on thermal light sources, much like the well-known incandescent light bulb, which has very limited brightness and limited possibilities for manipulating and using the light in different applications. This dissertation presents the past three years of my work with developing an alternative light source that has the broad spectral bandwidth of a lamp, and high power focused in a tight spot similar to a laser. Such a mid-infrared light source can be achieved through a process known as supercontinuum generation.

Supercontinuum generation is a spectacular process in which an intense single color laser line can generate new colors by propagation in a nonlinear medium, such as a glass optical fiber. The theory of supercontinuum generation is therefore presented as well as experimental and numerical results. Several different configurations of lasers and fibers are investigated, together with techniques for increasing the power, such as imprinting of anti-reflective structures and reducing the diameter of the fiber to increase the nonlinearity and thus efficiency of the supercontinuum generation. Finally the light sources are put to the test in a series of proof-of-concept demonstrations, designed to benefit from the unique properties of supercontinuum light sources. It is believed that such a source can find application within for example food analysis and diagnosis of early-stage skin cancer.

DANSK RESUMÉ (DANISH SUMMARY)

Spektroskopi er læren om lysets vekselvirkning med molekyler, og kan blandt andet bruges til at identificere specifikke stoffer i fødevarer eller medicin ved at studere hvilke dele af lyset der bliver absorberet efter vekselvirkning med en prøve. Især infrarødt lys, mere specifikt den midt-infrarøde del af spektret, er interessant fordi næsten alle molekyler har karakteristiske absorptions fingeraftryk i dette område. Nuværende instrumenter til spektroskopi benytter termiske lyskilder, meget lig de velkendte glødepærer, som udsender relativt svagt og ufokuseret lys, der kun kan benyttes under særlige forudsætninger. Denne Ph.D. afhandling præsenterer de seneste tre års arbejde med udvikling af en særlig lyskilde, der som en lampe dækker et bredt område at det infrarøde lysspektrum, og som en laser har alt lyset samlet i et lille punkt med høj intensitet. Sådan en midt-infrarød lyskilde kan skabes ved hjælp af en proces ved navn superkontinuum generering.

Superkontinuum generering dækker over en spektakulær proces hvorved en enkelt-farvet laser kan generere nye farver og brede dem ud i et kontinuum ved hjælp at et såkaldt ikke-linært medie, så som f.eks. en optisk fiber. Teorien bag superkontinuum bliver således præsenteret, sammen med eksperimentelle og numeriske resultater. Flere forskellige konfigurationer af lasere og fibre bliver undersøgt sammen med teknikker for at øge lysstyrken, som f.eks. ved at indprente anti-reflektive strukturer på fibrene, eller ved at reducere diameteren på fibrene for at øge ikke-lineariteten, og derved øge superkontinuum effektiviteten. Endeligt bliver den udviklede lyskilde benyttet i en række pilot eksperimenter, der er designet til at udnytte superkontinuum kildens gode egenskaber. Vi mener at denne type lyskilde vil kunne finde anvendelse inden for f.eks. fødevareanalyse eller diagnosticering af hudkræft i et tidligt stadie.

LIST OF PUBLICATIONS

Journal Papers

[I] G. Demetriou, J.-P. Bérubé, R. Vallée, Y. Messaddeq, C. R. Petersen, D. Jain, O. Bang, C. Craig, D. W. Hewak, and A. K. Kar, "Refractive index and dispersion control of ultrafast laser inscribed waveguides in gallium lanthanum sulphide for near and mid-infrared applications," Opt. Express **24**, 6350-6358 (2016).

[II] C. R. Petersen, P. M. Moselund, C. Petersen, U. Møller, and O. Bang, "Spectral-temporal composition matters when cascading supercontinua into the mid-infrared," Opt. Express **24**, 749-758. (2016).

[III] U. Møller, Y. Yu, I. Kubat, C. R. Petersen, X. Gai, L. Brilland, D. Méchin, C. Caillaud, J. Troles, B. Luther-Davies, and O. Bang, "Multi-milliwatt mid-infrared supercontinuum generation in a suspended core chalcogenide fiber," Opt. Express **23**, 3282–3291 (2015).

[IV] C. R. Petersen, U. Møller, I. Kubat, B. Zhou, S. Dupont, J. Ramsay, T. Benson, S. Sujecki, N. Abdel-Moneim, Z. Tang, D. Furniss, A. Seddon, and O. Bang, "Mid-infrared supercontinuum covering the 1.4–13.3 μm molecular fingerprint region using ultra-high NA chalcogenide step-index fiber," Nat. Photonics **8**, 830–834 (2014).

[V] I. Kubat, C. R. Petersen, U. V. Møller, A. Seddon, T. Benson, L. Brilland, D. Méchin, P. M. Moselund, and O. Bang, "Thulium pumped mid-infrared 0.9–9μm supercontinuum generation in concatenated fluoride and chalcogenide glass fibers," Opt. Express **22**, 3959–3967 (2014).

Conference Papers

[i] C. R. Petersen, P. M. Moselund, C. Petersen, U. Møller, O. Bang, "Mid-IR supercontinuum generation beyond 7 μm using a silica-fluoride-chalcogenide fiber cascade", in *SPIE BiOS,* vol. 9703, paper 97030A (2016).

[ii] *(Invited)* A. B. Seddon, T. M. Benson, S. Sujecki, N. Abdel-Moneim, Z. Tang, D. Furniss, L. Sojka, N. Stone, N. Jayakrupakar, G. R. Lloyd, I. Lindsay, J. Ward, M. Farries, P. M. Moselund, B. Napier, S. Lamrini, U. Møller, I. Kubat, C. R. Petersen, O. Bang, "Towards the mid-infrared optical biopsy," in *SPIE BiOS*, vol. 9703, no. 0, p. 970302, 2016.

[iii] B. Luther-Davies, Y. Yu, B. Zhang, X. Gai, C. Zhai, S. Qi, W. Guo, Z. Yang, R. Wang, D. Choi, S. Madden, U. Møller, I. Kubat, C. Petersen, L. Brilland, D. Méchin, C. Caillaud, J. Troles, and O. Bang, "Mid infrared supercontinuum generation from chalcogenide glass waveguides and fibers," in *Nonlinear Optics*, paper NTu1A.4 (2015).

[iv] *(Invited)* C. R. Petersen, U. Møller, I. Kubat, B. Zhou, S. Dupont, J. Ramsay, T. Benson, S. Sujecki, N. Abdel-Moneim, Z. Tang, D. Furniss, A. Seddon, and O. Bang, "Mid-Infrared Supercontinuum Generation Spanning More Than 11 μm in a Chalcogenide Step-Index Fiber," in *CLEO: 2015*, paper SF2D.7 (2015).

[v] U. Møller, C. R. Petersen, I. Kubat, Y. Yu, X. Gai, L. Brilland, D. Méchin, C. Caillaud, J. Troles, B. Luther-Davies, and O. Bang, "Two-Octave Mid-Infrared Supercontinuum Generation in As-Se Suspended Core Fibers," in *CLEO: 2015*, paper SW1L.7 (2015).

[vi] U. Møller, Y. Yu, C. R. Petersen, I. Kubat, D. Mechin, L. Brilland, J. Troles, B. Luther-Davies, and O. Bang, "High Average Power Mid-infrared Supercontinuum Generation in a Suspended Core Chalcogenide Fiber," in *Advanced Photonics*, paper JM5A.54 (2014).

[vii] I. Kubat, C. R. Petersen, U. Møller, A. Seddon, T. Benson, L. Brilland, D. Mechin, P. Moselund, and O. Bang, "Mid-infrared supercontinu-

um generation in concatenated fluoride and chalcogenide glass fibers covering more than three octaves," in *CLEO: 2014*, paper STh3N.1 (2014).

Other and Future Planned Contributions

(Accepted) M. R. Lotz, C. R. Petersen, M. H. Jakobsen, R. Taborysk, "Nanoimprinting on chalcogenide mid-IR-fiber end-facets to reduce coupling losses", Poster presentation at Micro and Nano Engineering, Vienna, Austria, Sep. 19-23, 2016.

The results of Chapter 4.4 with supercontinuum generation in tapered GeAsSe photonic crystal fiber is due for publication shortly after handing in this dissertation.

Invited talk on "Generation and Applications of High Average Power Mid-IR Supercontinuum in Chalcogenide Fibres", at Frontiers in Optics, Rochester, NY, US, Oct. 17-21, 2016.

Invited talk on "Mid-infrared supercontinuum generation (TBA)", at CLEO 2017, San Jose, CA, US, May 14-19, 2017.

Peer-reviewed 23 journal papers.

Chapter 1

Introduction

"Any sufficiently advanced technology is indistinguishable from magic."

— Arthur C. Clarke, Profiles of the Future.

Beyond the colors of light that our human eye can perceive is an entire spectrum of invisible light, the so-called infrared light Infrared light was first discovered by Sir Frederick William Herschel in 1800 when studying the difference in temperature induced by the individual colors of light [1]. He did this by passing sunlight through a prism to separate the colors into a spectrum and then measure the individual colors with a thermometer. He discovered that going from violet to red the temperature increased, but to his surprise the temperature increased even further just beyond the visible red light, and so he had discovered what would later be known as infrared radiation. The term infrared in general refers to the region of the electromagnetic spectrum between visible and microwave radiation. The distinction between light and radiation is somewhat of a philosophical nature, nevertheless infrared light is generally perceived as radiation that is undetectable by the human eye, specifically light with a wavelength between 0.7-1000 μm. Objects on this scale include everything from bacteria and cells to the diameter of a human hair and a grain of sand. The properties and applications of light over the entire infrared spectrum is equally diverse, so to more precisely state the region of interest for a specific application the region is often divided into multiple sub-bands according to some division scheme. One such scheme is ISO 20473, which divides the infrared into three spectral regions: The near-infrared (0.78-3 μm), mid-infrared (3-50 μm), and far-infrared (50-1000 μm).

The infrared spectral region is of interest in the field of infrared spectroscopy, which is a chemical analytical method for investigating the chemical composition of substances by interpreting how infrared light interacts with the sample. It has been known for several decades that parts of the infrared light is connected to the vibrations of molecules, and that the interaction of this infrared light with molecules causes parts of the light to be absorbed. The parts of the light that is missing after interacting with the molecule then forms a distinct *fingerprint* that is unique to that specific molecule, and therefore can be used to identify it. Especially the 2.5-25 μm part of the mid-infrared (mid-IR) is of interest because practically all molecules display highly distinctive spectral absorption fingerprints in this region, allowing the unambiguous identification of chemical substances in various samples. For this reason this reason it is often referred to as the fingerprint region. Infrared spectroscopy has been employed extensively in such diverse areas as early cancer diagnostics [2–5], protein dynamics [6–8], trace gas detection [9,10], and food quality assurance and process monitoring. Applications within food production are elaborated in the following section.

1.1 Light and Food

This dissertation is based on the PhD Project "Light and Food" funded by the Innovation Fund Denmark (formerly Danish Advanced Technology Foundation) (J.nr. 132-2012-3) with the goal of developing a platform of analytical solutions for the food industry based on bright and broad infrared light sources. Through sensitive real-time measurements of quality parameters, such analytical instruments can provide a solution for enabling demanding on-line process monitoring, fiber distributed sensing, microspectroscopy, and non-destructive testing. The hypothesis is that when combining new IR-sources with spectroscopy, chemometrics, and processing expertise, the technology will enable faster, more sensitive and flexible analysis of grains, soils and dairy products. We believe that the future of food production is based on molecular insights in all branches of the value chain, from the field and the sorting of raw materials to the process control in production and quality control at the consumer end. Examples of infrared spectroscopy applied in the context of food analysis include:

- **Adulterant identification** such as detection of melamine added in milk to give the appearance of high protein content [11].
- **Quantitative analysis** such as identifying the concentration of protein, glucose, or other constituents in food products used in pricing or assessment of food quality [12].
- **Process monitoring** such as monitoring phenolic compounds during fermentation of wine that affect the taste and color [1].
- **Waste reduction** such as reducing process water waste in the dairy industry [13,14], or monitoring the staling of bread [15].
- **Sorting and selective breeding** such as identifying barley phenotypes with higher levels of beta glucan for potential health benefits [16].
- **Food safety** such as detecting mycotoxins in the food and feed chains [17], identification of foodborne pathogens [18], or determination of acetone in cow milk [19].

Unfortunately many applications in mid-IR spectroscopy has been limited by the maturity of mid-IR technology and availability of light sources. Conventional mid-IR instruments have relied on thermal radiation from e.g. a glowing silicon carbide rod (Globar) because they are cheap, stable, and a reliable source of infrared radiation. However, thermal emitters have low emission power spectral density, and radiates in all directions, i.e. spatially incoherent, limiting the minimum focused spot size that can be probed and maximum path length light can travel in a medium. One area that has traditionally been very difficult is analysis of aqueous samples, such as milk. Water has very high absorption across the mid-IR region, which means that the sample volume has to be very small for light to penetrate the sample, and even then water may obstruct some spectral features of other constituents. Figure 1.1.1 shows the absorption of liquid water from 0.2-15 μm along with the position of a few spectral fingerprints of interest in the context of milk analysis, which clearly illustrates the challenges of the mid-IR. As an example, to measure the Amide I peak of protein at 6.05 μm requires detection of a signal that is attenuated by a factor of 2,600 per centimeter, which is why transmission cells for such measurements are limited to around 7 μm path length to avoid total absorption from water [7].

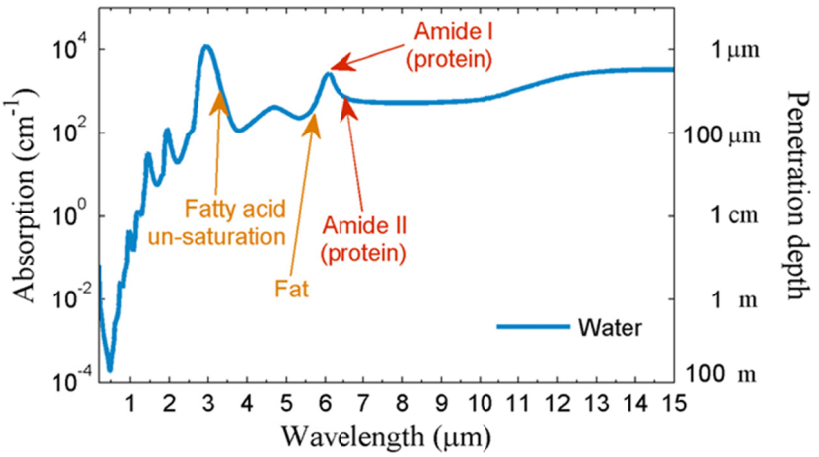

Figure 1.1.1: Absorption of liquid water from 0.2-15 μm (data from D. Segelstein [20]) together with a few arrows indicating absorption bands from fat and protein in milk. The presence of water can thus cause complete absorption of infrared light making it impossible to detect other substances. The approximate penetration depth of light is indicated on the right-hand axis.

For these reasons there is a need for spatially coherent light sources with a high power spectral density (PSD) across a broad bandwidth in the mid-IR region. One way of obtaining such a source is by utilizing synchrotron radiation from ring accelerators or free-electron lasers, however, such sources are quite elaborate and costly, with many users and limited flexibility, and thus mainly suitable for purely academic demonstrations. On the other hand the development of tunable quantum cascade lasers (QCL) has shown great potential within certain mid-IR applications in imaging, spectroscopy, and optical coherence tomography (OCT) due to several orders of magnitude improvement in PSD [7,21–23]. However, the tuning range for a single QCL is usually limited to a few hundred wavenumbers, and so several QCLs are required to span the mid-IR region making such a system potentially very costly [24]. Another promising technology is so-called supercontinuum generation (SCG), which refers to the spectral broadening of a laser due to complex light-matter interaction inside a nonlinear medium, such as an optical fiber. Supercontinuum (SC) sources based on silica glass optical fibers are commercially available for covering the visible and near-infrared (near-IR) spectral range, and these have been applied in a wide range of applications, such as fluorescence microscopy [25], OCT [26,27], and photoacoustic imaging [28]. Moving SC sources into

the mid-IR represents a significant challenge, due to the need for new exotic glasses, components, and laser sources. It is the goal of my Ph.D. studies to be on the forefront of the development of mid-IR SC sources, and to identify and demonstrate the potential applications and of these sources.

1.2 Scope and Outline

The main focus of the dissertation is the research and development of fiber-based mid-IR SC light sources, with an emphasis on obtaining high average output power and a broad bandwidth for use in spectroscopic applications, and mainly within food analysis.

The dissertation is organized in the following way:

- **Chapter 2: Theory of Light-Matter Interaction**
  The basic theory regarding propagation of light and the linear and nonlinear effects governing supercontinuum generation in optical fibers is presented. Through basic understanding of how light interacts with electrons and molecules, several insights into material properties and optical phenomena are made. Finally, the nonlinear Schrödinger equation is developed, which is used to numerically investigate supercontinuum generation.

- **Chapter 3: Mid-Infrared Materials and Waveguides**
  An overview of the various materials and waveguides suitable for the mid-IR spectral region is presented. Then the methodology of how we measure the important dispersion parameter in fibers and waveguides is shown, which later in Chapter 4.5.3 is demonstrated to have critical impact on cascaded supercontinuum generation. The chapter continues with the characterization of ultrafast laser inscribed waveguides manufactured at Heriot-Watt University, which was published in journal paper [I], and ends with our work with nanoimprint lithography of fiber end-facets to obtain antireflective properties.

- **Chapter 4: Supercontinuum Generation in Chalcogenide Fibers**
  In this chapter results with mid-IR supercontinuum generation in various fiber- and pump configurations is presented. First the results of journal paper [IV] is presented, which at the time of publication represented the broadest spectrum ever recorded in an optical fiber. The chapter proceeds to our work on simultaneously achieving high average output power and the broadest possible bandwidth, using a MHz pump source and various different fibers (Includes excerpts from papers [III],[iii],[v], and [vi]). Finally the results with cascaded supercontinuum generation are presented. Cascading in chalcogenide fibers was initially presented in the numerical papers [V] and [vii], and later experimentally verified in papers [II] and [i].

- **Chapter 5: Applications in Spectroscopy and Imaging**
  The strengths and weaknesses are discussed in this chapter in order to identify potential applications and pitfalls within spectroscopy and imaging. Three experimental proof-of-concept demonstrations are presented for transmission/diffuse reflectance of skin, and transmission spectroscopy on whey protein ultrafiltration membranes and liquid milk.

- **Chapter 6: Conclusion and Outlook**
  We take a step back and look at what has been accomplished, what was the major issues, and how do we proceed to overcome these in the future.

Chapter 2

Theory of Light-Matter Interaction

"Very simple was my explanation, and plausible enough - as most wrong theories are!"

— H.G. Wells, The Time Machine

The linear and nonlinear response of a material to an applied field is the basis for understanding vibrational spectroscopy and SCG. The optical response of a material has multiple sources, including: electronic response from the anharmonic motion of bound electrons, vibrational response from molecular motion, and possibly acoustic motion due to electrostriction. There are also molecular rotational modes but these are only found in liquids and gasses, and will therefore not be covered in this work. As a starting point the electronic and vibrational response is elucidated from the harmonic oscillator model and the induced polarization elaborated through basic quantum theory. From the basics understanding of electronic and vibrational resonances, we can then start to explain specific material properties, such as dispersion and attenuation. Once the linear effects have been established, the reader is introduced to Maxwell's equations and the wave equation that governs propagation of light in optical fibers. Finally, the nonlinear phenomena that are most relevant to SCG in fibers are explained, and placed in the context of the generalized nonlinear Schrödinger equation used for modelling SCG.

2.1 Linear Effects

2.1.1 Electronic Response

(Based on F. Pedrotti et al. (2007) [29] and M. Fox (2010) [30])

The complex interaction of light with isotropic dielectrics, such as glasses, can to some extent be explained by the classical harmonic oscillator model. Light incident on a medium causes displacement of the charged particles of the atoms in response to the applied electric field. This causes a shift of the position of the electron cloud $\bar{\boldsymbol{r}}$ relative to the nucleus, creating an induced dipole, and the collective dipole moment of N electronic charges of magnitude e per unit volume is then referred to as the induced polarization $\bar{\boldsymbol{P}}$ of the material:

$$\bar{\boldsymbol{P}} = -Ne\bar{\boldsymbol{r}} \tag{2.1.1}$$

The bound electrons will have a restoring spring-like force proportional to the displacement from the effectively static nuclei, and a friction-like dampening force proportional to the velocity due loss of energy from interaction with neighboring atoms, and from radiation due to forced oscillations, as depicted in Figure 2.1.1.

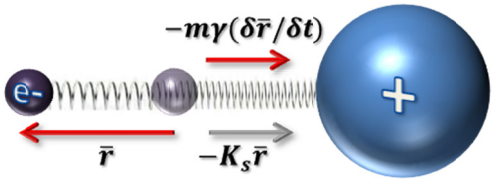

Figure 2.1.1: Illustration of harmonic oscillator model for electronic oscillations in response to an applied electric field. The large nucleus (+) may be assumed to be static due to the larger relative mass, thus only the electron (e-) oscillates about its equilibrium experiencing restoring forces proportional to the displacement and velocity.

Applying Hooke's law to Newton's second law then leads to the damped harmonic oscillator model for describing the motion of electron displacement with respect to time t:

$$-\frac{\delta^2\bar{\boldsymbol{r}}}{\delta t^2}m - m\gamma\frac{\delta\bar{\boldsymbol{r}}}{\delta t} - K_s\bar{\boldsymbol{r}} = e\bar{\boldsymbol{E}} \tag{2.1.2}$$

where γ is a frictional constant, K_s is the spring constant, m is the electronic mass, and $\bar{\boldsymbol{E}}$ is the electric field. Assuming a harmonic electric field $\bar{\boldsymbol{E}} = \bar{\boldsymbol{E}}_0 e^{-i\omega t}$ oscillating in time t at the frequency ω, and a similar harmonic response $\bar{\boldsymbol{r}} = \bar{\boldsymbol{r}}_0 e^{-i\omega t}$, the derivatives of equation (2.1.2) become trivial, leading to the solution:

$$\bar{\boldsymbol{r}} = \frac{-e\bar{\boldsymbol{E}}}{-m\omega^2 - im\omega\gamma + K_s} \tag{2.1.3}$$

Inserting eq. (2.1.3) into eq. (2.1.1), and accounting for the contribution to the local electric field from all other dipoles in the medium, given by $\bar{\boldsymbol{P}}/3\epsilon_0$ where ϵ_0 is the vacuum permittivity, the induced polarization becomes:

$$\bar{\boldsymbol{P}} = \left(\frac{Ne^2}{-m\omega^2 - im\omega\gamma + K_s}\right)\left(\bar{\boldsymbol{E}} + \frac{\bar{\boldsymbol{P}}}{3\epsilon_0}\right) \tag{2.1.4}$$

Defining the quantity $\omega_0^2 = K_s/m - Ne^2/3m\epsilon_0$, and rewriting equation (2.1.4) to solve for $\bar{\boldsymbol{P}}$:

$$\bar{\boldsymbol{P}} = \left(\frac{Ne^2/m}{\omega_0^2 - \omega^2 - i\omega\gamma}\right)\bar{\boldsymbol{E}} \tag{2.1.5}$$

The magnitude of the polarization is then given by:

$$|\bar{\boldsymbol{P}}| = \left(\frac{Ne^2/m}{\sqrt{(\omega_0^2 - \omega^2)^2 + \omega^2\gamma^2}}\right)|\bar{\boldsymbol{E}}| \tag{2.1.6}$$

It is now evident that besides being proportional to the magnitude of the electric field, the magnitude of the induced polarization is also frequency dependent and increases as $\omega \to \omega_0$, so that ω_0 represents a resonance frequency of the atom. At this frequency energy is transferred very efficiently from the electric field to polarize the atom, leading to a sharp electronic absorption line. In quantum theory the resonant electronic absorption corresponds to the excitation of an electron from the ground state to an excited state, which can only occur at a discrete quan-

tized energy level $E_p = \hbar\omega = E_2 - E_1$, where $\hbar$ is the reduced Planck's constant, and E_p, E_1, and E_2 are the energies of the photon, ground, and excited states, respectively. The excited electron will then undergo a series of radiative and/or non-radiative relaxation transitions back to the ground state. For single atoms and very small molecules the electronic transitions usually occur in the ultraviolet region due to the small mass, whereas larger molecules will tend to have electronic transitions in the visible to near-infrared. In optical waveguides the electronic absorption of the host glass effectively determines the lower transmission edge of the waveguide due to an exponential increase in absorption below the bandgap known as the Urbach tail.

2.1.2 Molecular Response

Similar to the case of electronic oscillations the harmonic oscillator model can be applied to describe ionic oscillations, namely the vibrational stretching of a heteronuclear diatomic molecule. In this case the two atoms both vibrate about their molecular equilibrium with amplitudes inversely proportional to their respective masses m_1 and m_2, thus maintaining a stationary center of mass. The characteristic oscillation frequency of this system is given by [31]:

$$\nu = \frac{1}{2\pi}\sqrt{K_s\left(\frac{1}{m_1}+\frac{1}{m_2}\right)} = \frac{1}{2\pi}\sqrt{\frac{K_s}{\mu}} \tag{2.1.7}$$

Here μ is the reduced mass of the diatomic molecule. For example the stretching vibrational resonance frequency in wavenumbers ($\tilde{\nu}_0 = \nu/c$) of isotope 35 of the H-Cl molecule can be approximated from the reduced mass $\mu = 0.98$ amu $= 1.62733 \times 10^{-27}$kg and bond strength constant $K_s = 480$ N m^{-1} [1]:

$$\tilde{\nu}_{0,HCL} = \frac{1}{2\pi c}\sqrt{\frac{K_s}{\mu}} = \frac{1}{2\pi\ 2.99792 \times 10^{10}\text{cm s}^{-1}} \times \sqrt{\frac{480\ \frac{\text{kg m}}{\text{s}^2}\ \text{m}^{-1}}{1.62733 \times 10^{-27}\ \text{kg}}} \approx 2883\ \text{cm}^{-1} \tag{2.1.8}$$

One limitation of the harmonic oscillator model is that only transitions of quantum number $\Delta n = \pm 1$ are allowed from applying quantum mechanical selection rules to a harmonic potential. In the classical picture it may be understood by noting that a transition of $\Delta n = +2$ for instance would require a photon of double the frequency, and since the vibration is harmonic there is no dipole moment component vibrating at this frequency [32]. However, most polyatomic molecules exhibit anharmonic motion, i.e. restoring forces that vary nonlinearly with displacement, which allow for overtone transitions $\Delta n > \pm 1$ due the transition probability becoming nonzero when the higher-order terms of the anharmonic potential is included. The anharmonic potential may be approximated by the so-called Morse potential, and the potential energy function of the harmonic and Morse potential is given by Eq. (2.1.9) and illustrated in Figure 2.1.2 [32]:

$$\begin{aligned} &\text{Harmonic potential:} && \tfrac{1}{2}K_s r^2 \\ &\text{Morse potential:} && D_e(1 - e^{-ar})^2 \end{aligned} \tag{2.1.9}$$

Here $a = \sqrt{2}/2 \times \sqrt{K_s/D_e}$, is a factor which scales the width of the potential function.

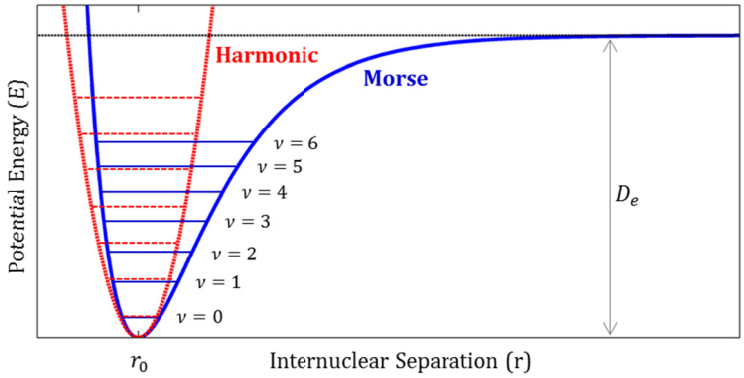

Figure 2.1.2: Illustration of the difference between harmonic and anharmonic potential energy functions. For small oscillations the harmonic oscillator is a good approximation, but for increasing internuclear separation the distance between energy levels become smaller for the Morse potential, converging towards the dissociation energy D_e where the two atoms are no longer bound to each other. Inspired by Fig. 1.13 in ref. [32].

The existence of higher-order transitions result in overtone absorption lines at shorter wavelengths compared to the fundamental, as illustrated in Figure 2.1.3. These overtones are not exact harmonics of the fundamental resonance due to anharmonicity, but will occur for slightly lower energy and hence higher wavelength.

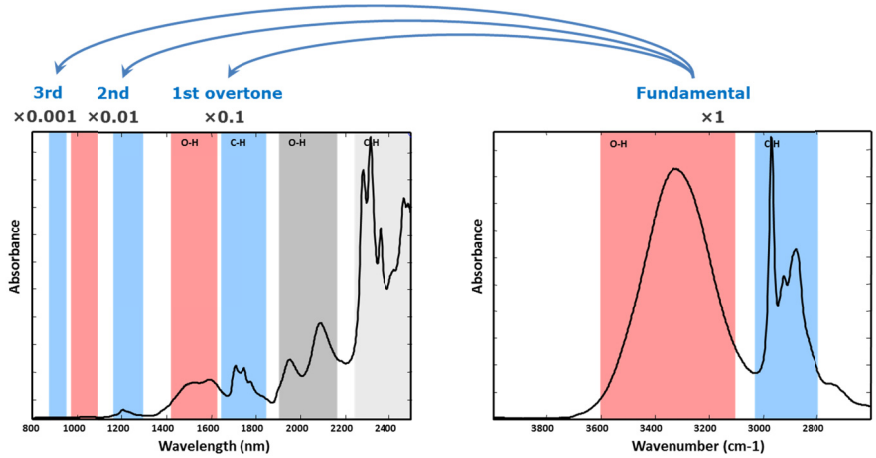

Figure 2.1.3: Illustration of overtone absorption lines of O-H and C-H. In effect the same information is repeated over and over across the spectrum albeit with lower absorbance, an effect sometimes referred to as the holographic dilution. Adapted with permission from Søren Balling, KU FOOD.

Furthermore anharmonicity allows for combination transitions through e.g. a three-phonon process where two phonons at ω_1 and ω_2 generate a new phonon at $\omega_3 = \omega_1 + \omega_2$ [30]. The white and gray bands of absorption features in Figure 2.1.3 are combination bands of C-H and O-H vibrations, respectively. The overtone and combination transitions have much lower probability compared to the fundamental transition and thus manifest as weaker absorption lines in the infrared spectrum [31]. The fundamental transition of molecules corresponds to photon energies in the mid-IR, whereas higher-order overtone and combination transitions are associated with the higher photon energy of near-IR radiation.

In general polyatomic molecules will have multiple vibrational resonances of varying strength governed by the individual atomic bond strengths, the translational/vibrational degrees of freedom, and probability of allowed transitions. Complex matrices, such as foods, consist of many different substances including hydrocarbons, proteins, and fats,

making interpretation of the absorption spectrum challenging. Applications of absorption spectroscopy in e.g. foods will be elaborated in Chapter 5.

2.1.3 DISPERSION

Refractive index dispersion is the frequency dependence $n(\omega)$ that originates from the wings of the electronic and vibrational absorption resonances, due to the mutual relation between refractive index and absorption coefficient through the Kramers-Kronig relations [30]. Away from resonances the refractive index may be well approximated by the Sellmeier equation [33,34]:

$$n^2(\omega) = 1 + \sum_{j=1}^{m} \frac{B_j \omega_j^2}{\omega_j^2 - \omega^2} \tag{2.1.10}$$

Where ω_j is the resonance frequencies of the material, and B_j is the resonance strength for the j'th resonance. In practice the B_j coefficients are found by fitting measured data to Eq. (2.1.10). The dispersion is said to be normal if the refractive index increases with frequency, and anomalous if it decreases. As a result different frequencies of light have slightly different index of refraction, and different phase-velocity $v_{ph} = c/n(\omega)$ when propagating in a medium. By propagating light of finite spectral width through a material thus causes its constituent frequency components to spread apart, an effect which will prove crucial in relation to SCG.

In waveguides the effective mode index is lower than the material index, which means that the total dispersion of the waveguide depends not only on the material properties, but also on the fiber structure. In standard SIFs the waveguide dispersion is usually weak compared to the material dispersion, but by utilizing microstructured designs the dispersion can be significantly modified. This will be covered briefly in Section 2.2.2.

2.1.4 Optical Attenuation

Light propagating in a medium is inevitably attenuated by a number of effects that depend on both the wavelength of light and properties of the medium. One source of attenuation is the electronic and molecular absorption of photons already covered in Sections 2.1 and 2.1.2, which gives rise to the short- and long-wavelength transmission edges of the material defined by electron and phonon resonances, as well as absorption due to the presence of defects and impurities.

The other primary source of attenuation in optical fibers is scattering due to either structural or material inhomogeneities. Scattering due to structural inhomogeneities is sometimes referred to as microdeformation loss, because it is caused by variations in the structure of the fiber, such as the core diameter [35]. As a result light is scattered between co-propagating modes in the core and/or cladding, which can lead to significant losses in microstructured fibers or SIFs with high index contrast, because the tension between regions of different glasses can lead to more inhomogeneities in the core.

Material inhomogeneities is another way of describing photons that are scattered by collision with the medium's constituent molecules, also known as Rayleigh scattering. In optical fibers this is often expressed in a macroscopic sense as fluctuations in the refractive index. It is referred to as a quasi-elastic scattering event since it induces no frequency shift [36], and it can be understood in a microscopic sense by analogy to the induced dipole introduced in Section 2.1.2. In this picture Rayleigh scattering is understood as the incoherent radiation of bound electrons due to a time-varying induced dipole. It may be quantized through the total scattering cross-section σ, describing the total scattered power of a linearly polarized field over all solid angles [36]:

$$\sigma = \frac{e^4\omega^4}{6\pi\epsilon_0 m^2 c^4[(\omega_0^2 - \omega^2)^2 + 4\omega^2\gamma^2]} \tag{2.1.11}$$

The scattered power is assumed to scale linearly with σ and intensity I_0, so $\boldsymbol{P_s} = I_0\sigma$, and so the scattered power is seen to increase as the fourth power of the optical frequency in the limit $\omega \ll \omega_0$. This also partly explains why the sky is blue, because the shorter blue wavelengths experi-

ence increased scattering by molecules in the atmosphere compared to the red.

Figure 2.1.4 show real data for light attenuation in various multimode SIFs made from different optical materials. The various loss mechanisms are indicated for the silica fiber (blue curve), including O-H impurity absorption at 1.4 µm. For the mid-IR fibers it is perhaps interesting to notice that the baseline loss is significantly higher than in silica, despite the lower relative contribution from Rayleigh scattering at longer wavelengths, which indicates that scattering from inhomogeneities of the glass and fiber structure is much more pronounced for mid-IR glasses.

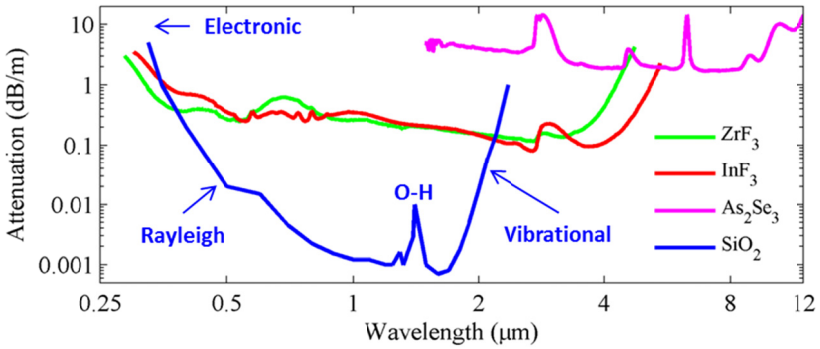

Figure 2.1.4: Attenuation curves for multimode fibers made from silica, zirconium fluoride, indium fluoride, and arsenic selenide. For the silica fiber the loss mechanisms are indicated, including O-H impurity absorption at 1.4 µm. Note the double log scale. (Data sources: Thorlabs: SiO_2, ZrF_3, InF_3; and [37]: As_2Se_3).

2.1.5 Optical Amplification

To compensate for the attenuation of light in a fiber, or simply to obtain higher signal power, optical signals may be amplified through a number of different gain processes, including: Raman gain, parametric gain, and stimulated emission. The first two are based on nonlinear processes, which will be partly covered in Sections 2.3.3 and 2.3.5, but the latter is a linear process governed by the absorption of a pump followed by the subsequent stimulated emission of photons at the signal wavelength. The principle is based on introducing luminescence centers to a host material, such as optically-active ions like the trivalent lanthanides, also known as rare-earth dopants, which include e.g. Yb^{3+}, Er^{3+}, and

Tm^{3+} [30]. In glass optical fibers the dopants become part of the amorphous glass matrix, and as such the electronic transitions of the dopant couple to the vibrational states of the host glass, giving rise to so-called vibronic bands. The vibronic coupling results in non-radiative intraband transitions, i.e. excitation of phonons, which introduces a Stokes shift between the absorption and emission energies [30]. Figure 2.1.5 shows the absorption and emission cross sections of Tm^{3+} (left) together with a partial energy level diagram (right), which shows some of the relevant transitions for Tm^{3+}-doped fibers.

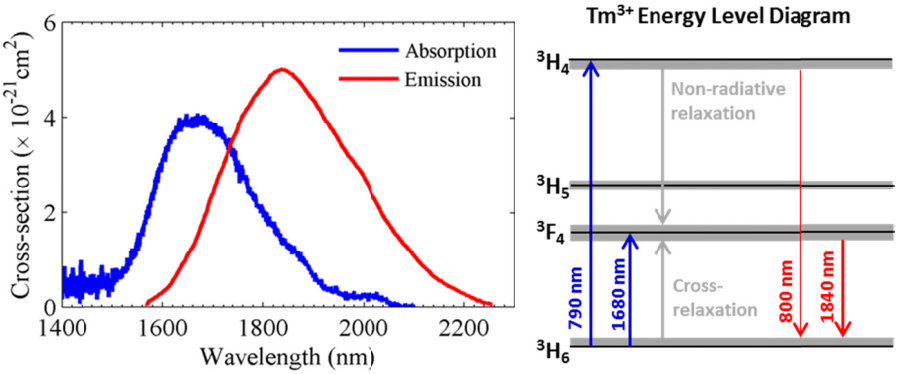

Figure 2.1.5: (Left) Example absorption and emission cross-sections for the Tm^{3+} ion near 1800 nm (data from the Thorlabs website), and (right) a diagram of the corresponding vibronic transitions including possible transitions around 800 nm, for which efficient pumping of the $^3F_4$ level may be obtained through cross-relaxation processes.

The figure shows that broadband emission in the region around 1840 nm can be achieved by pumping the $^3H_6 \rightarrow {}^3F_4$ transition at 1680 nm, but it is also possible by pumping at 790 nm because of fast non-radiative relaxation transitions from $^3H_4 \rightarrow {}^3F_4$, meaning that the 800 nm emission has a very low quantum efficiency [38]. In fact, pumping at 790 nm is very attractive due to the presence of cross-relaxation, which is a process in which a Tm-ion in the excited $^3H_4$ state excites a neighboring Tm-ion by splitting the energy between them so both end up in the $^3F_4$ state, thus obtaining two laser photons per pump photon [38]. Furthermore, cross-relaxation increases with dopant concentration, making Tm-doped amplifiers highly efficient.

2.2 LINEAR PULSE PROPAGATION IN OPTICAL FIBERS

(Based on G. Agrawal (2013) [33] and R. W. Boyd (2008) [36])

2.2.1 MAXWELL'S EQUATIONS AND THE WAVE EQUATION

Propagation of an electromagnetic field in an optical medium is governed by Maxwell's equations, and in the case of optical fibers where there is no current ($\bar{\mathbf{J}} = 0$) or charge density ($\rho = 0$) of the medium, the equations may be written in their differential form as:

$$\begin{aligned} \nabla \times \bar{\mathbf{E}} &= -\frac{\partial \bar{\mathbf{B}}}{\partial \mathrm{t}} \\ \nabla \times \bar{\mathbf{H}} &= \bar{\mathbf{J}} + \frac{\partial \bar{\mathbf{D}}}{\partial \mathrm{t}} = \frac{\partial \bar{\mathbf{D}}}{\partial \mathrm{t}} \\ \nabla \cdot \bar{\mathbf{D}} &= \rho = 0 \\ \nabla \cdot \bar{\mathbf{B}} &= 0 \end{aligned} \tag{2.2.1}$$

where $\bar{\mathbf{E}}$ and $\bar{\mathbf{H}}$ are vectors representing the electric and magnetic field, and $\bar{\mathbf{B}}$ and $\bar{\mathbf{D}}$ are the electric and magnetic flux densities, respectively. The equations relate the rate of changes of the electric and magnetic flux densities in response to an applied field according to the following relations:

$$\begin{aligned} \bar{\mathbf{D}} &= \epsilon_0 \bar{\mathbf{E}} + \bar{\mathbf{P}} \\ \bar{\mathbf{B}} &= \mu_0 \bar{\mathbf{H}} + \bar{\mathbf{M}} \end{aligned} \tag{2.2.2}$$

where μ_0 and ϵ_0 are the vacuum permeability and permittiviy, and $\bar{\mathbf{M}}$ is the magnetic induced polarization, which is zero in the case of a non-magnetic medium. From the equations in (2.2.1) and (2.2.2) the wave equation may be derived as:

$$\nabla^2 \bar{\mathbf{E}} = \frac{1}{c^2}\frac{\partial^2 \bar{\mathbf{E}}}{\partial t^2} + \frac{1}{\epsilon_0 c^2}\frac{\partial^2 \bar{\mathbf{P}}}{\partial t^2} \tag{2.2.3}$$

where the definition of the speed of light in vacuum $c = 1/\sqrt{\mu_0 \epsilon_0}$ and the following relations $\nabla \times \nabla \times E = \nabla(\nabla \cdot \mathrm{E}) - \nabla^2 \mathrm{E} = -\nabla^2 E$, and

$\nabla \cdot \mathrm{D} = \nabla \cdot \mathrm{E}\epsilon = 0$, was used. In the linear propagation regime Eq. (2.2.3) may be simplified by expressing $\bar{\mathbf{P}}$ in terms of the electric field, and convert to the frequency domain by Fourier transformation (denoted with the symbol ~) to apply the convolution theorem:

$$\bar{\mathbf{P}} = \epsilon_0 \int_{-\infty}^{\mathrm{t}} \chi(t-t')\bar{\mathbf{E}}(t')\,dt' = \tilde{\chi}(\omega)\tilde{\boldsymbol{E}}(\omega) \tag{2.2.4}$$

$$\tilde{\boldsymbol{E}}(\omega) = \int_{-\infty}^{\infty} \bar{\mathbf{E}}(t)\exp(i\omega t)\,dt \tag{2.2.5}$$

The wave equation may now be expressed in the frequency domain as:

$$\nabla^2\tilde{\boldsymbol{E}}(\omega) = \epsilon(\omega)\frac{\omega^2}{c^2}\tilde{\boldsymbol{E}}(\omega) \tag{2.2.6}$$

where $\epsilon(\omega) = 1 + \tilde{\chi}(\omega) = n^2(\omega)$, assuming a lossless medium. Eq. (2.2.6) now has the form of the Helmholtz equation [39], and solutions to this equation will be discussed in the following sections.

2.2.2 Optical fibers and propagation modes

The simplest type of optical fiber is the step-index fiber (SIF), in which a circular core of refractive index n_{core} is enclosed by a circular cladding of lower refractive index n_{clad}, as is shown in Figure 2.2.1.

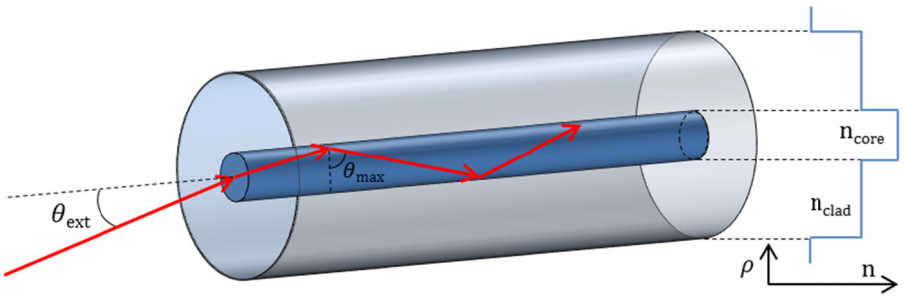

Figure 2.2.1: Geometry and ray-guiding picture of an optical fiber showing refraction at the air-glass interface (neglecting reflection), and total internal reflection at the core-cladding interface. The step-index contrast between the core and cladding refractive indices is indicated to the right as a function of the radial coordinate ρ.

In the ray optics picture such a structure allows for light to be guided by total internal reflection according to Snell's law of refraction. Total internal reflection occurs at a maximum incident angle of $\sin(\theta_{max}) = n_{\text{clad}}/n_{\text{core}}$, and from trigonometry the acceptance angle of the fiber for which this condition is fulfilled is then given by the numerical aperture (NA) [39,40]:

$$\sin(\theta_{ext}) = \sqrt{n_{\text{core}}^2 - n_{\text{clad}}^2} = \text{NA} \tag{2.2.7}$$

This formalism gives a nice intuitive understanding of how optical fibers work, however, to more accurately understand the guiding properties of a SIF in the context of wave optics, it requires solving the wave equation (2.2.6) derived in the previous section. This is most easily done by adopting a scalar approach assuming that the electric field is linearly polarized with unit vector $\bar{x}$ along the radial coordinate ρ, and by separating the rapidly varying part of the electric field, such that:

$$\mathbf{E}(\boldsymbol{r}, t) = \frac{1}{2}\bar{x}[\mathrm{E}(\boldsymbol{r}, t)\exp(-i\omega_0 t) + c.c.] \tag{2.2.8}$$

where $\mathrm{E}(r, t)$ is a slowly varying function of time relative to the optical period, ω_0 is the carrier frequency, and c.c. is short for the complex conjugate. Eq. (2.2.6) can then be solved by separation of variables to yield a solution of the form:

$$\widetilde{\mathrm{E}}(\mathbf{r}, \omega - \omega_0) = \bar{x}\,\mathrm{F}(x, y)\widetilde{\mathrm{A}}(z, \omega - \omega_0)\exp(i\beta_0 z) \tag{2.2.9}$$

where $\tilde{A}(z, \omega)$ is assumed to be a slowly varying function of z, and β_0 is the propagation constant of the wave. $\mathrm{F}(x, y)$ describes the transverse spatial distribution of the electric field. For optical fibers it is common to describe the mode by its effective area, defined by [33]:

$$A_{\text{eff}} = \frac{\left(\iint_{-\infty}^{\infty} |F(x, y)|^2 \,\mathrm{dx}\,\mathrm{dy}\right)^2}{\iint_{-\infty}^{\infty} |F(x, y)|^4 \,\mathrm{dx}\,\mathrm{dy}} \tag{2.2.10}$$

The effective area is an important factor when considering nonlinearities in pulse propagation in Section 2.3. Since the SIF possesses cylindrical symmetry the mode distribution it is most conveniently found by adopting cylindrical coordinates [33]:

$$\frac{\partial^2 \mathrm{F}}{\partial \rho^2} + \frac{1}{\rho}\frac{\partial \mathrm{F}}{\partial \rho} + \left(n^2 k_0^2 - \beta^2 - \frac{m^2}{\rho^2}\right)\mathrm{F} = 0 \tag{2.2.11}$$

Solutions to Eq. (2.2.11) are linear combinations of Bessel functions for the core region, and modified Bessel functions for the cladding, and can be found by applying the boundary conditions that $\bar{\mathbf{E}}$ and $\bar{\mathbf{H}}$ should be continuous at the core-cladding interface, and decay exponentially in the cladding region with increasing radial distance. This leads to an eigenvalue equation that has several (l) solutions for β for each integer value of m. Each eigenvalue describes a fiber mode, denoted β_{ml}, and only modes that fulfil $k_0 n_{clad} < \beta < k_0 n_{core}$ are guided by the fiber. The number of modes supported by a fiber depends on several parameters, namely the NA, the core radius (a), and the excitation wavelength. A useful parameter in this respect is the normalized frequency or V-parameter, which can be used in combination with the aforementioned eigenvalue equation to identify when different modes are no longer supported by the fiber [33].

$$V = \frac{2\pi a}{\lambda}\mathrm{NA} \tag{2.2.12}$$

Equation (2.2.12) is used to define the single-mode cut-off criteria $V < V_c$, for which only a single mode is supported. This cut-off frequency is found as the smallest solution to the Bessel function, $J_0(V_c) = 0$, which occurs for $V_c = 2.405$ [33]. As an example, using the parameters for the zirconium fluoride SIF in Section 3.3.1 ($\mathrm{NA} = 0.265, a = 3.4$ µm), the fiber is found to be single-mode for wavelengths longer than 2.4 µm, while the arsenic selenide fiber from Section 4.2.1 ($\mathrm{NA} = 0.99, a = 8$ µm) only becomes single-mode for wavelengths longer than 20.7 µm.

Photonic Crystal Fiber

One fiber design that revolutionized the field of nonlinear fiber optics and SCG is the photonic crystal fiber (PCF), also known as *holey fibers*

and the more elusive term *microstructured optical fibers*. The typical design is based on a periodic, hexagonal lattice of capillaries forming a cladding region with one or more missing capillaries in the center forming the core, as depicted in Figure 2.2.2.

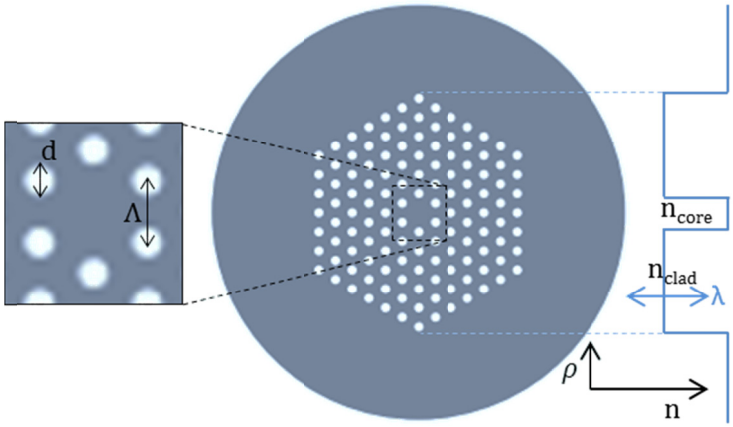

Figure 2.2.2: Geometry of the hexagonal PCF with a single-cell core and air capillary cladding. The capillary diameter and pitch is indicated in the zoomed-in region of the core. The refractive index profile to the right indicates that the glass-air hole structure results in an effective cladding index that is lower than the core and changes with wavelength.

The capillaries are often made of air and are maintained down the longitudinal direction of the fiber to create a low-index region, and thus the fiber guides by index guiding similar to the SIF. However, unlike SIFs the effective refractive index of the microstructured cladding is highly wavelength dependent, and is determined by the properties of the fundamental-space-filling mode (β_{fsm}), i.e. cladding mode. For comparison the corresponding normalized frequency may be calculated as [41]:

$$V_{\text{eff}} = a\sqrt{k^2 n_{core}^2 - \beta_{fsm}^2} \tag{2.2.13}$$

The primary difference compared to Eq. (2.2.12) is that V_{eff}, although not immediately apparent from Eq. (2.2.13), converges towards a stationary value in the high frequency limit because of a vanishing core-cladding index contrast, and the value depends only on the ratio between the capillary diameter (d) and the lattice pitch or distance between adjacent capillaries (Λ) [41]. The second-order mode cut-off oc-

curs for $V_{\text{eff}} < 4.2$, and so by designing PCFs specifically with $d/\Lambda < 0.45$, it has been found that V_{eff} converge towards a value below the cut-off making the fiber endlessly single-moded [41]. The primary implication is that the core diameter may be scaled without introducing guided higher-order modes (HOMs), and that the dispersion can be significantly altered by tuning the values of d and Λ.

2.2.3 GROUP-VELOCITY DISPERSION

The effect of dispersion on fiber propagation is usually included by performing a Taylor expansion of the propagation coefficient around some center frequency ω_0 [33]:

$$\beta(\omega) = \beta_0 + \beta_1(\omega - \omega_0) + \frac{1}{2}\beta_2(\omega - \omega_0)^2 + \cdots + \frac{1}{m!}\beta_m(\omega - \omega_0)^m \tag{2.2.14}$$

For a pulse of some finite spectral bandwidth the envelope of the pulse can be said to travels as a wave packet with group-velocity: $v_g = 1/\beta_1$, and β_2 then represents the group-velocity dispersion (GVD), which is often expressed through the dispersion parameter D, defined as:

$$D = \frac{\partial \beta_1}{\partial \lambda} = -\frac{2\pi c}{\lambda^2}\beta_2 \tag{2.2.15}$$

The dispersion is said to be normal when $\beta_2 > 0$, so that the group velocity decreases with wavelength, and anomalous when $\beta_2 < 0$. When gauging the impact of dispersion it is useful to define the two following characteristic length scales [33]:

$$L_D = \frac{T_0^2}{|\beta_2|} \quad , \quad L_W = \frac{T_0}{|\beta_1(\omega_2) - \beta_1(\omega_1)|} \tag{2.2.16}$$

L_D is the dispersion length, which describes the length of fiber over which dispersion causes a pulse of duration T_0 ($1/e^2$ of maximum intensity) to broaden by a factor of $\sqrt{2}$. L_W is the walk-off length associated with the group-velocity mismatch of two pulses overlapping in time but

off-set in frequency at ω_1 and ω_2, which defines the propagation length after which the pulse interaction is negligible.

Even at the wavelength where $\beta_2 = 0$, known as the zero dispersion wavelength (ZDW), third-order dispersion (TOD) from the β_3 term can cause asymmetric pulse broadening [33]. The primary impact of TOD on SCG is to introduce a perturbation to the stability of solitary waves, known as solitons, resulting in the break-up of the soliton and the generation of resonant radiation, known as dispersive waves (DW) [42]. This subject is covered in section 2.3.6.

2.2.4 Dispersive Pulse Propagation

Returning to the solution to the Helmholtz equation in Eq. (2.2.9), the envelope or amplitude term $\tilde{\mathrm{A}}(z,\omega)$ was assumed to be a slowly varying function compared to the carrier frequency. The slowly varying envelope approximation in the time domain is equivalent to the condition that the bandwidth of the optical field is much smaller than the carrier frequency, so that the second-order derivatives may be neglected and $\tilde{\mathrm{A}}(z,\omega)$ may be adhere to [33]:

$$2i\beta_0 \frac{\partial \tilde{\mathrm{A}}}{\partial z} + (\beta^2 - \beta_0^2)\tilde{\mathrm{A}} = 0 \tag{2.2.17}$$

And by making use of the approximation $\beta^2 - \beta_0^2 \approx 2\beta_0(\beta - \beta_0)$, Eq. (2.2.17) becomes [33]:

$$\frac{\partial \tilde{\mathrm{A}}}{\partial z} = i(\beta(\omega) - \beta_0)\tilde{\mathrm{A}} \tag{2.2.18}$$

Including the expansion terms of the propagation constant up to second order (thus ignoring TOD for now), the β_0 term cancels out, and taking the inverse Fourier transform then yields the following envelope equation for linear and lossless propagation [33]:

$$\frac{\partial \mathrm{A}}{\partial z} = -\beta_1 \frac{\partial \mathrm{A}}{\partial t} - \frac{i\beta_2}{2}\frac{\partial^2 \mathrm{A}}{\partial t^2} \tag{2.2.19}$$

Losses can be included by adding the term $-(\alpha/2)A$ to the RHS of Eq. (2.2.19). Eq. (2.2.19) can be used to illustrate the basic features of linear and scalar pulse propagation in optical fibers, in particularly the effect of GVD. By rewriting the equation in a retarded time frame moving at the GV of the pulse ($T = t - z/v_g$) the simplified equation becomes:

$$\frac{\partial \mathrm{A}}{\partial z} = -\frac{i\beta_2}{2}\frac{\partial^2 \mathrm{A}}{\partial T^2} \tag{2.2.20}$$

Eq. (2.2.20) is most easily solved in the frequency domain since the derivatives $\partial/\partial t \to -i\omega$. Taking the Fourier transform then yields:

$$\frac{\partial \widetilde{\mathrm{A}}}{\partial z} = \frac{i\beta_2}{2}\omega^2 \tilde{A} \tag{2.2.21}$$

With the solution:

$$\widetilde{\mathrm{A}}(z,\omega) = \exp\left(\frac{i\beta_2}{2}\omega^2 z\right)\tilde{A}(0,\omega) \tag{2.2.22}$$

It is seen from the above equation that effect of GVD is to impose a phase shift on the pulse through the imaginary exponent, depending on both frequency and propagation length. It is also clear that it does not change the spectral shape of the pulse, however, it does change the temporal shape. Eq. (2.2.22) can be visualized through a numerical routine that calculates the Fourier transform of an arbitrary waveform. Using a Gaussian pulse with $T_0 = 1$ ps, the pulse amplitude and spectrum was calculated for various propagation lengths between zero and four times the dispersion length. It is seen from Figure 2.2.3(a) that the spectral shape is unchanged, and Figure 2.2.3(b) displays the linear chirp across the broadened pulse.

Including nonlinear interaction to the equation is the subject of the following sections.

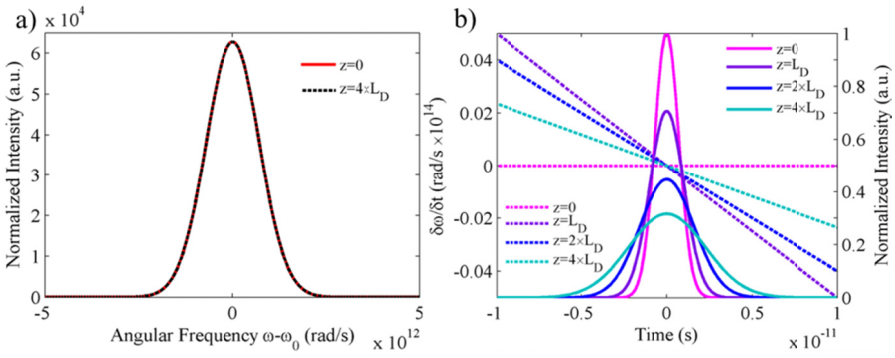

Figure 2.2.3: (a) Calculated spectrum of a 1 ps Gaussian pulse after propagating $z = 4 \times L_D$, which is overlapping the $z = 0$ curve. (b) Calculated pulse broadening (solid curve) and frequency chirp (dashed curve) for $z = 0, z = L_D, z = 2L_D, z = 4L_D$.

2.3 Nonlinear Effects

Spectral broadening in SCG is related to the nonlinear response of a dielectric material to an applied electric field with sufficiently high peak field strength, and the fact that a time-varying polarization can act as the source of new components of the electromagnetic field. This relation can be seen from the nonlinear wave equation for an isotropic media [36]:

$$\nabla^2 \overline{\boldsymbol{E}} - \frac{\epsilon_r}{c^2}\frac{\partial^2 \overline{\boldsymbol{E}}}{\partial t^2} = \frac{1}{\epsilon_0 c^2}\frac{\partial^2 \overline{\boldsymbol{P}}_{NL}}{\partial t^2} \tag{2.3.1}$$

where $\overline{\boldsymbol{P}}_{NL}$ is the nonlinear part of the induced polarization that arises because the induced polarization is not linear with the applied field strength as described by eq. (2.1.6), but can instead be described as a power series [36]:

$$\overline{\boldsymbol{P}} = \epsilon_0\left(\chi^{(1)}\overline{\boldsymbol{E}} + \chi^{(2)}\overline{\boldsymbol{E}}^2 + \chi^{(3)}\overline{\boldsymbol{E}}^3 + \cdots + \chi^{(n)}\overline{\boldsymbol{E}}^n\right) \tag{2.3.2}$$

where $\chi^{(n)}$ is a rank n+1 material response tensor known as the susceptibility. The first term accounts for the linear response, which is dominating at low field strength, and for isotropic centro-symmetric materials, such as glasses, the second-order susceptibility $\chi^{(2)}$ term vanishes, so the first and most significant higher-order polarization term in such systems is due to third-order $\chi^{(3)}$ nonlinearity. The induced polarization

can therefore be split into the linear contribution from $\chi^{(1)}$ and the nonlinear contribution from $\chi^{(3)}$ [33]:

$$\bar{\boldsymbol{P}}_L(\boldsymbol{r},t) = \epsilon_0 \int_{-\infty}^{t} \chi^{(1)}(t-t')\bar{\boldsymbol{E}}(\boldsymbol{r},t')dt' \tag{2.3.3}$$

$$\bar{\boldsymbol{P}}_{NL}(\boldsymbol{r},t) = \epsilon_0 \iiint_{-\infty}^{t} \chi^{(3)}(t,t_1,t_2,t_3)\bar{\boldsymbol{E}}(\boldsymbol{r},t_1)\bar{\boldsymbol{E}}(\boldsymbol{r},t_2)\bar{\boldsymbol{E}}(\boldsymbol{r},t_3)dt_1dt_2dt_3 \tag{2.3.4}$$

Eq. (2.3.4) is a generalized description of third-order nonlinear effects, but due to its complexity it is instructive to initially make the assumption that the response is instantaneous, i.e. only of electronic origin. If the rapidly varying part of the electric is again separated, as in Eq. (2.2.8) the third-order nonlinear contribution becomes [33]:

$$\bar{\boldsymbol{P}}^{(3)} = \epsilon_0\chi^{(3)}\left(\frac{1}{2}\left[\bar{\boldsymbol{E}}_1 e^{-i\omega_1 t} + \bar{\boldsymbol{E}}_2 e^{-i\omega_2 t} + \bar{\boldsymbol{E}}_3 e^{-i\omega_3 t} + c.c.\right]\right)^3 \tag{2.3.5}$$

Expanding Eq. (2.3.5) reveals a large number of combination terms that describe multiple nonlinear processes, including: The optical Kerr effect, which is the source of self-phase modulation (SPM) and cross-phase modulation (XPM), third harmonic generation (THG), and four-wave mixing (FWM). Because the vibrational response has been neglected in Eq. (2.3.5) it does not include such effects as Raman scattering or Brillouin scattering, but will be introduced later in the chapter. All of the above mentioned effects are treated separately below with the exception of THG and Brillouin scattering, which are negligible effects in short-pulsed SCG in optical fibers due to phase matching requirements and long electrostrictive response time [36], respectively.

2.3.1 Kerr effect and the Nonlinear Schrödinger Equation

The Kerr effect, also known as nonlinear refraction, refers to the field intensity dependence of the refractive index. If losses are neglected, the nonlinear refraction follows the equation [33]:

$$n(\omega, I) = n_0(\omega) + n_2 I = n_0(\omega) + n_2|\boldsymbol{E}|^2 \tag{2.3.6}$$

where n_2 is the nonlinear refractive index coefficient. Nonlinear refraction can be included in Eq. (2.2.19) by considering the Kerr effect as a small perturbation to the refractive index (Δn). According to first-order perturbation theory Δn does not affect the modal distribution $F(x,y)$, but the propagation constant becomes modified as [33]:

$$\tilde{\beta}(\omega) = \beta(\omega) + \Delta\beta(\omega) \tag{2.3.7}$$

$$\Delta\beta(\omega) = \frac{\omega^2 n(\omega)}{c^2 \beta(\omega)} \frac{\iint_{-\infty}^{\infty} \Delta n(\omega) |F(x,y)|^2 \mathrm{dx\ dy}}{\iint_{-\infty}^{\infty} |F(x,y)|^2 \mathrm{dx\ dy}} \tag{2.3.8}$$

Eq. (2.2.19) then becomes:

$$\frac{\partial \mathrm{A}}{\partial z} + \frac{i\beta_2}{2} \frac{\partial^2 \mathrm{A}}{\partial T^2} = i\Delta\beta \mathrm{A} \tag{2.3.9}$$

By neglecting loss the relation $\Delta n(\omega) = n_2 |\boldsymbol{E}|^2$ may be used, and by assuming $\beta(\omega) \approx n(\omega)\omega/c$, and that the modal area is unchanged the perturbation is reduced to:

$$\Delta\beta(\omega) = \gamma |A|^2 \tag{2.3.10}$$

$$\gamma = \frac{n_2 \omega_0}{c A_{\mathrm{eff}}} \tag{2.3.11}$$

Taylor expansion of $\Delta\beta$ can be omitted because of the quasi-monochromatic assumption ($\Delta\omega \ll \omega_0$), so the perturbation reduces to $\Delta\beta \approx \Delta\beta_0$, resulting in [33]:

$$\frac{\partial \mathrm{A}}{\partial z} + \frac{i\beta_2}{2} \frac{\partial^2 \mathrm{A}}{\partial T^2} = i\gamma |A|^2 \mathrm{A} \tag{2.3.12}$$

The pulse propagation eq. (2.3.12) is referred to as the nonlinear Schrödinger equation (NLSE), because it resembles the Schrödinger equation with a nonlinear potential.

Another consequence of the Kerr effect is the intensity dependence of the group-velocity, which causes the more intense pulse peak to propagate slower than the wings, and thus shift towards the trailing edge of

the pulse. It causes a steepening of the pulse, which is why it is referred to as self-steepening, eventually leading to an optical shock wave and wave-breaking. However, GVD acts against the steepening, and so it requires numerical simulations to investigate further. Self-steepening will be included into the NLSE in Section 2.4

2.3.2 Self-phase and Cross-phase Modulation

The effect of nonlinear refraction on pulse propagation becomes apparent when considering that the accumulated phase of a pulse ϕ over a distance z is given by [33]:

$$\phi = nk_0 z = (n_0 + n_2|\boldsymbol{E}|^2)k_0 z \tag{2.3.13}$$

where $k_0 = 2\pi/\lambda_0$. A pulse propagating in a fiber will thus experience a self-induced nonlinear phase shift $\phi_{NL} = n_2|\boldsymbol{E}|^2 k_0 z$ over the temporal envelope, known as self-phase modulation (SPM). It leads to a shift in the instantaneous frequency, i.e. the frequency of the pulse at a specific time instance of the pulse envelope, which is intuitively understood from the relation between the rate of change of the nonlinear phase shift and instantaneous frequency [33]:

$$\frac{\partial \omega}{\partial t} = -\frac{\partial \phi_{NL}}{\partial t} \tag{2.3.14}$$

At the leading edge of the pulse the intensity and thus nonlinear phase increases, resulting in a positive derivative and thus a decrease in instantaneous frequency, and vice versa for the trailing edge. The result is a nonlinear frequency chirp across the pulse, and the generation of new frequency components accumulating over the length of the fiber. The spectral broadening and induced nonlinear frequency chirp can be visualized by numerically solving Eq. (2.3.12) with $\beta_2 = 0$. The result is plotted in Figure 2.3.1 for a 1 ps Gaussian pulse in terms of the nonlinear length, defined as:

$$L_{NL} = \frac{1}{\gamma P_0} \tag{2.3.15}$$

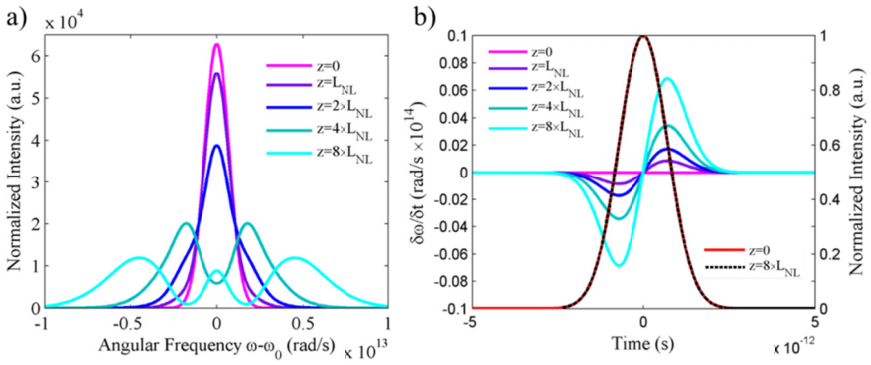

Figure 2.3.1: (a) Illustration of SPM spectral broadening of a pulse with increasing propagation length in an optical fiber from $z = 0$ to $z = 8L_{NL}$. (b) Evolution of the nonlinear frequency chirp over the pulse envelope with increasing propagation length. The pulse shape is preserved during propagation.

Cross-phase modulation (XPM) refers to the nonlinear phase shift due to interaction between pulses overlapping in time. In the case of two co-propagating pulses at ω_1 and ω_2 eq. (2.3.5) is of the form [33]:

$$\overline{\boldsymbol{P}}^{(3)} = \epsilon_0 \chi^{(3)} \left(\frac{1}{2}\left[E_1 e^{-i\omega_1 t} + E_2 e^{-i\omega_2 t} + c.c.\right]\right)^3 \tag{2.3.16}$$

The expansion of the brackets result in six terms, where only the two terms with exclusively $\omega_1$and $\omega_2$are considered here [36]:

$$\begin{aligned} \overline{\boldsymbol{P}}^{(3)}(\omega_1) &= \frac{\epsilon_0 \chi^{(3)}}{4}(3\overline{\boldsymbol{E}}_1\overline{\boldsymbol{E}}_1^* + 6\overline{\boldsymbol{E}}_2\overline{\boldsymbol{E}}_2^*)\overline{\boldsymbol{E}}_1 = \chi_{eff}^{(3)}(|\overline{\boldsymbol{E}}_1|^2 + 2|\overline{\boldsymbol{E}}_2|^2)\overline{\boldsymbol{E}}_1 \\ \overline{\boldsymbol{P}}^{(3)}(\omega_2) &= \frac{\epsilon_0 \chi^{(3)}}{4}(3\overline{\boldsymbol{E}}_2\overline{\boldsymbol{E}}_2^* + 6\overline{\boldsymbol{E}}_1\overline{\boldsymbol{E}}_1^*)\overline{\boldsymbol{E}}_2 = \chi_{eff}^{(3)}(|\overline{\boldsymbol{E}}_2|^2 + 2|\overline{\boldsymbol{E}}_1|^2)\overline{\boldsymbol{E}}_2 \end{aligned} \tag{2.3.17}$$

Where $\chi_{eff}^{(3)} = (3\epsilon_0\chi^{(3)}/4)$ and the relation of the electric field and its complex conjugate $\overline{\boldsymbol{E}}\overline{\boldsymbol{E}}^* = |\overline{\boldsymbol{E}}|^2$ was used. The second terms in the brackets of Eqs. (2.3.17) are due to XPM, which is seen to have twice the magnitude of the first SPM term. The induced nonlinear phase shift of the two pulses can thus be expressed as [33]:

$$\begin{aligned} \phi_{NL,\omega_1} &= n_2 k_0 z(|\overline{\boldsymbol{E}}_1|^2 + 2|\overline{\boldsymbol{E}}_2|^2) \\ \phi_{NL,\omega_2} &= n_2 k_0 z(|\overline{\boldsymbol{E}}_2|^2 + 2|\overline{\boldsymbol{E}}_1|^2) \end{aligned} \tag{2.3.18}$$

The importance of XPM in SCG will be further elaborated on in section 2.3.6 on the discussion of soliton dynamics.

2.3.3 FOUR-WAVE MIXING

In Eqs. (2.3.17) the remaining four terms from the expansion of eq. (2.3.16) was neglected, because they contained either combination terms of ω_1 and ω_2 or third harmonic terms. These terms represent so-called four-wave mixing (FWM). FWM is a third-order parametric process that occurs when photons from one or more waves are annihilated to create photons at new frequencies, while conserving the net energy and momentum during the parametric interaction [33]. The efficiency of the process therefore requires both frequency and wave vector matching between the interacting waves, also known as phase matching. There are basically two types of phase-matched FWM, where the first involves three photons at frequencies ω_1, ω_2, and ω_3 transferring energy to a fourth photon at the frequency $\omega_4 = \omega_1 + \omega_2 + \omega_3$. This is the case of THG ($\omega_1 = \omega_2 = \omega_3$), or frequency conversion ($\omega_1 = \omega_2 \neq \omega_3$). However, in these processes it is difficult to achieve phase matching with $\Delta\beta = (\beta_{\omega 1} + \beta_{\omega 2} + \beta_{\omega 3} - \beta_{\omega 4}) = 0$ due to dispersion walk-off. The other type involves the simultaneous annihilation and generation of two photons, such that $\omega_3 + \omega_4 = \omega_1 + \omega_2$. For this process it is easier to satisfy the phase matching condition since now $\Delta\beta = (\beta_{\omega 3} + \beta_{\omega 4} - \beta_{\omega 1} - \beta_{\omega 2}) = 0$ [33].

The degenerate case of $\omega_1 = \omega_2$ illustrated in Figure 2.3.2 is the most relevant for SCG, where a pump at ω_p creates two sidebands at frequencies ω_s (Stokes/signal) and ω_i (anti-Stokes/idler), such that the Stokes frequency-shift is $\Omega_s = \omega_p - \omega_s = \omega_i - \omega_p$. This degenerate case can also be used for parametric amplification by providing gain to a signal at ω_s through pumping at ω_p. The maximum gain of the parametric amplification can be approximated as $g_{max}=2\pi n_2 P_\mathrm{p}/(\lambda_\mathrm{p} A_{eff})$, where P_p is the pump power, and λ_p is the pump wavelength [33].

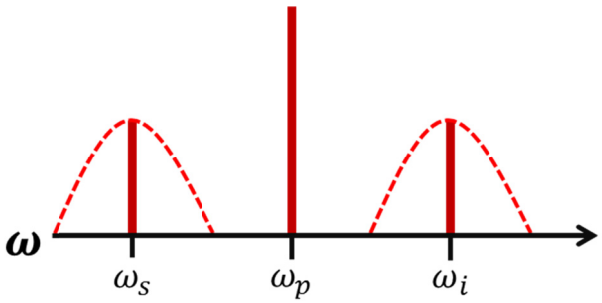

Figure 2.3.2: Illustration of degenerate FWM where two pump photons at ω_p are annihilated to create a photon at the signal (ω_s) and idler (ω_i) frequencies. The dashed line illustrate the formation of lobes due to the non-zero gain at $\Delta\beta \neq 0$.

By assuming a slowly varying envelope and single transverse mode the interacting waves can be described in terms of the complex amplitude $A(z)$ [43]:

$$\begin{aligned}
\frac{\delta A_p}{\delta z} &= i\gamma\left[\left(|A_p|^2 + 2(|A_s|^2 + |A_i|^2)\right)A_p + 2A_sA_iA_p^* \exp(i\Delta\beta z)\right] - \frac{\alpha}{2}A_P \\
\frac{\delta A_s}{\delta z} &= i\gamma\left[\left(|A_s|^2 + 2\left(|A_i|^2 + |A_p|^2\right)\right)A_s + A_i^*A_p^2 \exp(-i\Delta\beta z)\right] - \frac{\alpha}{2}A_s \\
\frac{\delta A_i}{\delta z} &= i\gamma\left[\left(|A_i|^2 + 2\left(|A_s|^2 + |A_p|^2\right)\right)A_i + A_s^*A_p^2 \exp(-i\Delta\beta z)\right] - \frac{\alpha}{2}A_i
\end{aligned} \tag{2.3.19}$$

where A_p, A_s, and A_i are the pump, signal and idler amplitude components, respectively, * denotes the complex conjugate, z is the propagation length in the fiber and α is the attenuation coefficient. The first two terms on the RHS of the equations describe SPM and XPM, respectively. The third term describes the transfer of energy between the interacting waves, which is seen to depend strongly on the phase-mismatch $\Delta\beta$ [43]. Furthermore, the accumulation of phase from SPM and XPM adds to the phase-mismatch, so that phase-matching requires $\Delta\beta + 2\gamma P_p = 0$. If fourth- and a higher-order terms are neglected , $\Delta\beta$ can, at the ZDW, be expressed as [43]:

$$\Delta\beta = \beta_3(\omega_p - \omega_{ZDW})(\omega_p - \omega_s)^2 \tag{2.3.20}$$

In the normal dispersion regime $\Delta\beta > 0$, which means that the total phase mismatch will increase with separation of the pump from the ZDW. It should be noted that in multimode or highly birefringent fibers it is possible to obtain phase-matching even in the normal dispersion

regime due to the substantially different waveguide dispersion of different modes. In the anomalous dispersion regime $\Delta\beta < 0$, and phase matching can thus be achieved, resulting in the formation of two gain lobes on each side of the pump with peak gain at $\Delta\beta = -2\gamma P_p$. The parametric process thus establishes a balance between GVD and the Kerr effect, which is identical to the phenomenon known as modulation instability, which is treated in the next section.

2.3.4 MODULATION INSTABILITY

Modulation instability (MI) is the exponential growth of a perturbation to the waveform, which can arise from e.g. pump noise or fiber inhomogeneities. MI can be thought of as a four-wave mixing process phase-matched by SPM, which leads to a temporal modulation of the pulse. In the frequency domain Fourier theory dictates that the temporal modulation results in the generation of sidebands at the modulation frequency on each side of the pump. It can be shown from adding a perturbation term to the NLSE that such a perturbation leads to a perturbation of the wavenumber (K) and frequency (Ω) [33]:

$$K = \pm\frac{1}{2}|\beta_2\Omega|\sqrt{\Omega^2 + \mathrm{sgn}(\beta_2)4\gamma P_0/|\beta_2|} \tag{2.3.21}$$

If $\beta_2 < 0$ the wavenumber becomes imaginary, leading to an exponential growth of the perturbation wave, similar to what was found in the analysis of SPM-phase-matched FWM. Although there are special cases where it is possible to observe MI in the normal dispersion regime, it is outside the scope of this work. The peak position of the sidebands and maximum gain is given by [33]:

$$\Omega_{\max} = \pm\sqrt{\frac{2\gamma P_0}{|\beta_2|}} \quad , \quad g_{max} = 2\gamma P_0 \tag{2.3.22}$$

As the sidebands grow in power they may also develop sidebands creating a cascade of MI peaks, and ultimately MI leads to the total break-up of the pulse into a train of short sub-pulses [33]. These sub-pulses are stable solutions known as solitons that balance the chirp of GVD and

SPM throughout propagation. This concept will be elaborated in Section 2.3.6.

2.3.5 RAMAN SCATTERING

Unlike Rayleigh scattering covered in Section 2.1.4, Raman scattering is the inelastic scattering of photons from molecules, which means that the photon energy is not preserved in the process. Physically it is understood as a non-resonant vibrational response, which unlike absorption involves a virtual upper energy state, and thus occurs irrespective of the optical pump frequency [33,36]. Figure 2.3.3 shows an energy level diagram of the two possible spontaneous Raman scattering processes [36].

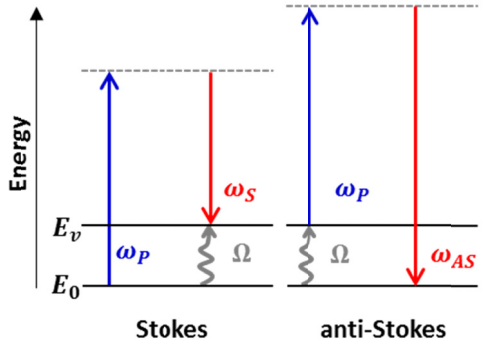

Figure 2.3.3: Energy level diagram displaying the principles the Stokes- and anti-Stokes frequency shifts due to Raman scattering.

In the Stokes process pump photons excite vibrational quanta in the medium, i.e. phonons, resulting in a loss of photon energy and a corresponding Stokes frequency shift. On the contrary, the anti-Stokes process involves scattering from an already excited vibrational state of the medium, resulting in a net energy gain of the photon and subsequent anti-Stokes frequency shift. As such, the Stokes shift is more commonly observed in experiments because materials in thermal equilibrium have a higher population in the ground state compared to the excited state given by the Boltzmann factor $\exp(\hbar\Omega/k_B T)$ [36]. If no photons are present at the Stokes frequency the process is known as spontaneous Raman scattering, but if the process is stimulated by a seed through either SPM, FWM, or indeed build-up from spontaneous Raman, it leads to significant amplification of the seed [33]. Indeed, one application of stimu-

lated Raman scattering (SRS) is to provide distributed amplification to a signal propagating in an optical fiber together with a high-power continuous-wave (CW) Raman pump separated in frequency by the Stokes shift. From the same argument it is apparent that a sufficiently broadband pulse will experience self-amplification of the low-frequency components, an effect known as intra-pulse Raman scattering (IPRS). IPRS is a very important effect in SCG which can lead to substantial red-shifting of sub-picosecond pulses. This will be further elaborated in Section 2.3.6 on solitons and dispersive waves.

SRS is a $\chi^{(3)}$ process, thus contributing to the third-order induced nonlinear polarization through a delayed vibrational response. To include the delayed response the causal, time-dependent nature of the nonlinear induced polarization from Eq. (2.3.4) must be taken into account. The nonlinear induced polarization then takes the form:

$$\boldsymbol{P_{NL}} = \epsilon_0 \chi^{(3)} \boldsymbol{E}(\boldsymbol{r}, t) \int R(t - t') \boldsymbol{E}^2(\boldsymbol{r}, t') dt' \tag{2.3.23}$$

In the above equation $R(t)$ is the normalized nonlinear-response function including both the effectively instantaneous electronic response, usually modelled as a delta-function $\delta(t)$, and the delayed vibrational response $h_R(t)$:

$$R(t) = (1 - f_R)\delta(t - t_e) + f_R h_R(t) \tag{2.3.24}$$

Here f_R is the fraction of the Raman response to the total response. The delayed response may be determined from the Raman-gain spectrum, which in turn is related to the imaginary part of the Fourier transform of $h_R(t)$.

Figure 2.3.4 shows an example of the Raman Stokes shift (equivalent to the gain spectrum) observed from the excitation of a $Ge_{10}As_{22}Se_{68}$ glass fiber with a 780 nm laser, which is just beyond the electronic resonance band [34].

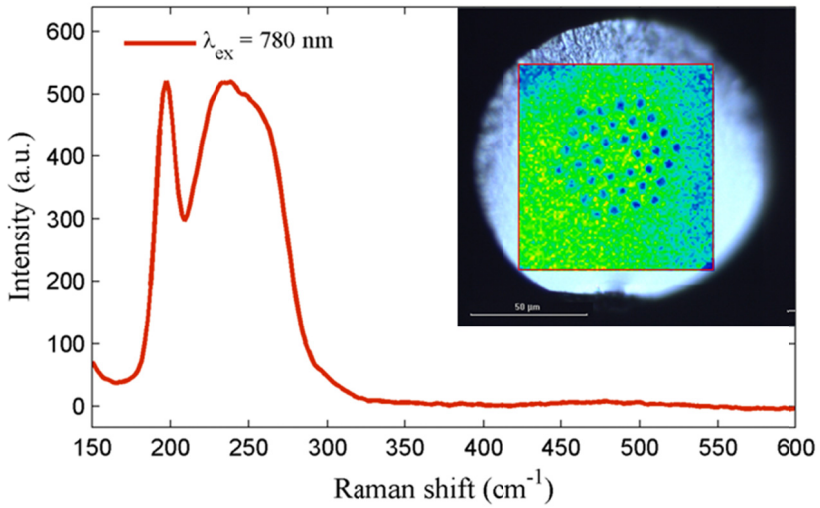

Figure 2.3.4: Raman spectrum of a $Ge_{10}As_{22}Se_{68}$ glass fiber excited with a 780 nm laser just beyond the electronic resonance. The multi-peak structure is due to the various vibrational modes of the amorphous glass matrix. The peaks in cm^{-1} corresponds to: 190 cm^{-1} = 5.780 THz, and 235 cm^{-1} = 7.174 THz. The entire Raman gain spectrum spans from 175-300 cm^{-1} = 5.317-9.207 THz. Inset: Raman map showing the relative intensity of the Raman signal from the fiber. (Data measured by C. Markos, DTU Fotonik).

The spectrum exhibits a multi-peak structure due to the various vibrational modes of the glass. In this example the Raman peaks at 195 cm^{-1} and 213 cm^{-1}, are from modes of the $GeSe_{4/2}$ tetrahedral units, the 230 cm^{-1} and 268cm-1 are from the $AsSe_{3/2}$ pyramidal units, and the peak at 250 cm^{-1} is due to the vibrational modes of Se chains or rings [44]. The intensity and position of the peaks thus reveals intricate information about the structure and composition of a material, a feature which is utilized extensively in the field of Raman spectroscopy, but it may also be used in the interpretation of SC spectra. Since the Raman Stokes shift is independent of excitation wavelength, SRS in a $Ge_{10}As_{22}Se_{68}$ glass fiber will appear in an optical spectrum shifted approximately 5.3-9.2 THz from the pump wavelength, corresponding to a Raman shift of 175-300 cm^{-1}.

Inclusion of the vibrational response changes the perturbation to the refractive index Δn and therefore $\Delta\beta$ and the solution of Eq. (2.3.10). The inclusion of SRS to the NLSE is performed in Section 2.4.

2.3.6 SOLITONS AND DISPERSIVE WAVES

From Figure 2.2.3(b) and Figure 2.3.1(b) it may be apparent that the chirp arising from GVD and SPM can be made to cancel each other if the right values for β_2 and P_0 peak power can be maintained so that $L_D = L_N$. This gives rise to the following relation [33]:

$$N^2 = \frac{L_D}{L_{NL}} = \frac{\gamma P_0 T_0^2}{|\beta_2|} \tag{2.3.25}$$

Where N is the integer soliton number, which results in N = 1 at the above mentioned balance between dispersion and nonlinearity, known as the fundamental soliton. If N<1 the nonlinearity from γP_0 is too weak, and the dispersion will enforce pulse broadening without soliton formation. If 2>N>1 the pulse propagating in the anomalous dispersion regime will adjust its shape with propagation in order to achieve this balance, and eventually evolve into a secant-hyperbolic (sech) pulse, irrespective of the input pulse shape. As a result, if loss, Raman, and TOD is neglected, the soliton will maintain its temporal and spectral shape throughout propagation, and is relatively stable against small perturbations. For N>2 higher-order solitons can be generated that does not maintain its shape, but rather has a periodic evolution over a propagation length known as the soliton period $z_0 = \pi L_D/2$. The higher-order soliton solution corresponds to a bound state superposition of N fundamental solitons that propagate together at the same GV. The duration and peak power of these fundamental solitons is related to the input pulse duration T_0 and peak power P_0 as [33]:

$$T_k = \frac{T_0}{2N + 1 - 2k} \quad , \qquad P_k = \frac{(2N + 1 - 2k)^2}{N^2} P_0 \tag{2.3.26}$$

Where k is an integer from 1 to N. The first ejected solitons is therefore the one with the shortest duration and highest peak power, and the subsequent will each in turn be longer and weaker. However, the degeneracy of the bound state is lifted in the presence of asymmetric perturbations, such as TOD, self-steepening, and intra-pulse Raman. If we accept that the N-soliton behaves as a superposition of N fundamental solitons it is easy to understand why TOD and intra-pulse Raman effects are likely to initiate soliton fission, because both effects force the solitons to

travel at different GV. As a result the soliton steady-state is perturbed, and the N-order soliton is split up into N fundamental solitons in a process known as soliton fission [45,46]. Soliton fission is not an instantaneous process, but rather develops over a length referred to as the fission length [42]:

$$L_{\text{fiss}} = L_D/N \tag{2.3.27}$$

From Eq. (2.3.26) it is clear that solitons with very short duration may be generated, and for durations of 1 ps or shorter the spectral width of the soliton is broad enough that the high-frequency components can amplify the low-frequency components through stimulated Raman scattering. This causes a continuous transfer of energy to longer wavelengths, causing an increasing red-shift of the soliton with propagation. This effect is known as soliton self-frequency shifting (SSFS), and is the main effect in combination with soliton fission that causes strong spectral broadening towards longer wavelengths. The first ejected soliton will experience the strongest degree of SSFS due to the increased peak power, and the following solitons will then experience a decreasing shift, thus forming a continuum of spectrally separated solitons.

Another consequence of higher-order dispersion is the generation of so-called dispersive waves (DW). Due to TOD, solitons ejected from the fission process will transfer part of their energy to a narrow-band resonance in the normal dispersion regime [42,45]. The resonance frequency can be calculated from a phase-matching argument involving the soliton linear and nonlinear phase, and the linear phase of a quasi-CW component at a different frequency. For a soliton of peak power P_s, frequency ω_s, and group velocity $v_{g,s}$ a DW is generated at the frequency ω_{DW} according to [42]:

$$\beta(\omega_s) - \frac{\omega_S}{v_{g,s}} + (1 - f_R)\gamma P_s = \beta(\omega_{DW}) - \omega_{DW}/v_{g,s} \tag{2.3.28}$$

The frequency shift $\Omega = \omega_s - \omega_{DW}$ between soliton and DW can be approximated if fourth-order dispersion is neglected [33]:

$$\Omega \approx -\frac{3\beta_2}{\beta_3} + \frac{\gamma P_s \beta_3}{3\beta_2^2} \tag{2.3.29}$$

For solitons propagating in a region of positive dispersion slope ($\beta_3 > 0$), the frequency shift is positive, meaning that the DW will be generated in the normal dispersion regime at shorter wavelengths. If on the other hand the dispersion slope is negative ($\beta_3 < 0$), the soliton approaches the normal dispersion regime on the long-wavelength side, and subsequently DW generation will occur for longer wavelengths. Interesting dynamics occur in the limit where SSFS has shifted the solitons close to the ZDW, however, this will be elaborated in Section 4.5.3 on cascaded SCG.

Lastly, the generated DWs will initially overlap with the solitons in time, allowing for interaction through XPM and FWM to generate new spectral components, but it may also lead to a soliton-like two-frequency soliton-DW state. Specifically, the Kerr and Raman effects may together with a varying local GVD lead to a localized non-dispersive trapped state of the DWs, in which they continuously blue-shift in response to the red-shifting solitons [47]. This mechanism may be explained by the soliton imposing a potential on the DW which is trapped on one side by the nonlinear refractive-index change induced by the intense solitons, and on the other side by a linear potential originating from the fact that the soliton moves with acceleration (changing GVD). As the soliton changes its GV during the red-shift, the trapped DW blue-shifts in order to maintain its GV, and the two are then said to be GV-matched. However, the trapping potential imposed by the soliton is not infinite, and thus the DWs inevitably leak radiation as they shift and may completely dissociate from the soliton.

Modelling of these higher-order effects requires a generalized form of the NLSE, which will be briefly presented in the following section.

2.4 The Generalized NLSE

A more accurate model than the NLSE presented in Eq. (2.3.12) is the generalized NLSE (GNLSE), which includes the vibrational contribution to the nonlinear induced polarization through the delayed response function $R(t)$, self-steepening through the $(i/\omega_0)\partial/\partial T$ term, and higher-order dispersion terms [33]:

$$\frac{\partial A}{\partial z} = i\sum_{m\geq 2}\frac{i^m\beta_m}{m!}\frac{\partial^m A}{\partial T^m} - \frac{\alpha}{2}A + i\gamma\left(1+\frac{i}{\omega_0}\frac{\partial}{\partial T}\right)\ldots \times\left(A(z,t)\int_{-\infty}^{\infty}R(T')|A(z,T-T')|^2dT'\right) \tag{2.4.1}$$

Inclusion of these terms is needed to explain the highly complex spectral-temporal evolution of SCG. Details about the implementation of the GNLSE used in this work are given in Section 4.2.3.

Chapter 3

Mid-Infrared Optical Fibers and Waveguides

"We are stuck with technology when what we really want is just stuff that works."

— Douglas Adams, The Salmon of Doubt

Many applications in sensing [48], near-field spectroscopy [49], endoscopy [50], and imaging [51–53] requires the delivery and collection of light over several tens of centimeters or even meters between the light source, point of interest, and detection system, which necessitates the use of optical fibers with low transmission loss over the signal bandwidth. Furthermore, nonlinear applications such as all-optical signal processing and supercontinuum generation requires specific tailored properties of the waveguides, such as dispersion, nonlinear coefficient, and numerical aperture (NA) [42,54]. For this reason, the pursuit of suitable host materials and waveguide designs for the mid-IR spectral region has intensified in recent years. This chapter provides a brief introduction to materials and designs used for mid-IR optical fibers and waveguides.

3.1 MID-INFRARED MATERIALS AND OPTICAL FIBERS

Optical fibers are usually drawn from glasses, which defines a wide range of amorphous solids that exhibit a glass transition when heated towards a liquid state, and so they are intrinsically isotropic and can be drawn over a wide temperature range [55,56]. Applications in the visible and near-IR has benefited from the low loss of fused silica (SiO_2) glass optical fibers, but due to phonon absorption from overtones and combination bands of Si-O-Si and O-H resonances, transmission in practical lengths of silica fiber is limited to below 2.4 μm, even in high-purity fibers with low O-H content [57,58]. In general to extend the infrared transmission of glasses heavier atoms with lower phonon energies are required. Fluoride glasses, such as ZrF4-BaF2-LaF3-AlF3-NaF (ZBLAN), can transmit light from 0.2-8 μm, but are still limited to below 4.75 μm in practical lengths of fiber [59–63]. Chalcogenide glasses, on the other hand, have been shown to transmit light out to 25 μm and furthermore possess strong optical nonlinearities up to several hundred times greater than that of silica, making them promising candidates for mid-IR fibers for SCG [54,55,64–66]. Chalcogenide glasses contain one or more of the chalcogen elements S, Se, and Te, in a glass matrix with structural elements like Ge, As, Ga, and Sb [56]. The properties of the glass can thus be engineered by changing the ratio of its constituent elements. A list of properties of some common chalcogenide materials relevant to this study is listed in Table 1.

Besides the broad transmission bandwidth and high nonlinear coefficient Table 1 shows another remarkable property of chalcogenide glasses, namely their low glass transition temperature (T_g). The implication of having T_g<200°C is that it allows for various processing of the glass at practical temperatures, such as hot embossing of structures or waveguides, but it also makes the glasses vulnerable to thermal effects, such as thermal optical damage [67], crystallization, oxidation and hydrolysis [68,69]. Hot embossing of chalcogenide waveguides from thin-film substrates has been demonstrated in As_2Se_3As2Se3 on $Ge_{17}As_{18}Se_{65}$ substrate, where the ~50°C higher T_g of the substrate allowed for shaping of the waveguide without deforming the substrate [70]. Hot imprinting of sub-wavelength structures has also been demonstrated to improve the damage threshold and reduce the Fresnel losses caused by the high refractive index of chalcogenide glass-

es [71–76]. The latter is especially useful since e.g. a refractive index of 2.82 of $As_{40}Se_{60}$ leads to ~23 % Fresnel reflection at each air-glass interface. Imprinting of chalcogenide glasses and fibers will be further elaborated in section 3.5.

Glass	n	n_2 ($10^{-20}m^2W^{-1}$)	T_g (°C)	ZDW (µm)	TBW (µm)
Silica	1.45 [59]	2.7 [59]	1215 [55] ~1200 [59]	1.26 [55,59]	0.3-3.5 [55] 0.24-3 [59]
ZBLAN	1.49 [55] 1.48-1.53 [59]	2.55 [59] 2.1 [77]	260 [55] 230-300 [59]	1.71 [55] 1.62 [59]	0.3-7.5 [55] 0.3-8 [59]
$As_{40}S_{60}$	2.5 [55] 2.42[g] [59,64]	400-600 [64] 540 [55] 300 [59]	187 [55] 185 [59,64] 215 [56]	4.81 [55] ~5 [59]	0.6-12.0 [55] 0.8-7 [59] 0.6-9.5 [64]
$As_{40}Se_{60}$	2.82 [34,37] 2.83 [59] 2.9 [55]	489.3[a] [37] 1620 [55] 1400-3000 [64] 1500 [59]	178 [64] 185 [70] 180 [78]	7.4 [34,37] 7.2 [59]	1.0-15.0 [55] 1-10 [59] 0.85-17.5 [64]
$As_{38}Se_{62}$	2.81[e]	1100[e]	165 [68]	--	--
$Te_{20}As_{30}Se_{50}$	2.9 [64] ~2.98 [79]	>2000 [64] 1898 [56]	137 [79] 140 [64]	>7.5 [55]	1.5-12+ [79] 1.23-18.52 [64]
$Ge_{10}As_{23.4}Se_{66.6}$	2.62 [34,37]	--	180 [78]	7.0 [34]	2-16[c] [67] 1.3-10+ [68]
$Ge_{10}As_{22}Se_{68}$	2.62[e] 2.62[b] [68]	880[e]	180 [68]	--	1.3-10+ [68]
GaLaS	2.38 [80] 2.41[d] [81]	216[d] [81]	560 [81]	3.61 [80]	0.5-10 [80,81]

Table 1: Comparison of bulk material properties of different glasses used for mid-IR fibers and waveguides (TBW: Transmission bandwidth). Parameters are measured at 1.55µm if not stated otherwise. (a) Calculated for 6.3 µm, (b) for Ge10As22Se68 glass, (c) for Ge12As24Se64 glass, (d) Measured at 1.52 µm, (e) data from manufacturer (Selenoptics), (f) Ge10As20Se70 glass, (g) Measured at 3 µm.

3.2 Optical fiber design

The broad transmission bandwidth and high nonlinear index of chalcogenide glasses enables the use of very short segments of fiber in broadband SCG, which allows for a small foot-print and significantly reduces

the impact of fiber losses [37,67,82,83]. However, the improved mid-IR bandwidth comes at the expense of a longer material ZDW, e.g. >7 μm in some Se-based glasses, which makes it challenging to fabricate fibers with a ZDW that is close to practical high peak power pump lasers for efficient SCG. Consequently, efforts have been made to reduce the ZDW of chalcogenide fibers by utilizing microstructured design, tapering, or by tuning the NA vs. core diameter in SIFs. The latter design optimization is elaborated on in Section 4.3.2.

Single-glass microstructured optical fibers (MOF) allow for engineering of the waveguide dispersion, while maintaining relatively simple fabrication, thus making them an attractive choice for commercial SCG fibers [54,84]. As an example, by using suspended-core fiber (SCF) and photonic crystal fiber (PCF) geometries, as seen in Figure 3.2.1, the ZDW of $As_{38}Se_{62}$ fibers has been reduced to 3.5 μm and 5.1 μm, respectively [82,85].

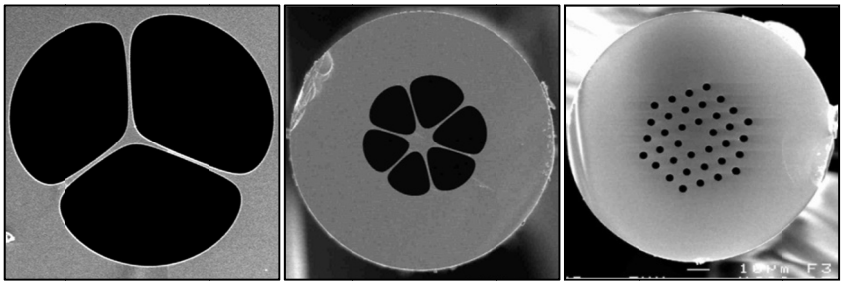

Figure 3.2.1: Single-material MOFs. Left: Suspended core structure. Middle: Wagon-wheel structure. Right: 3-ring hexagonal air-hole PCF (*Source:* Perfos chalcogenide fiber data sheet).

Due to the geometry of the SCF the core and suspending struts are thermally isolated, making them susceptible to thermal optical damage. Furthermore, the fiber supports multiple modes and is slightly birefringent, but the high air-filling fraction of the structure also results in a high NA enabling tight mode confinement and relatively short ZDW [82,86]. The PCF guiding properties depend mainly on the hole diameter and pitch, such that when the $d/\Lambda < 0.45$ the fiber is endlessly single-moded. The single-mode of the PCF structure is an especially desirable trait, since it improves the output beam quality and increases spectral broadening in SCG [87,88]. The hexagonal air-hole cladding also

enables relatively high NA, while improving the thermal dissipation from the core compared to the suspended-core.

Tapering has also been employed extensively in relation to chalcogenide fibers to obtain a shorter ZDW below 2 μm for pumping with standard 1.55 μm or 2 μm laser sources [89–93]. While tapering can effectively lower the ZDW, it may also have adverse effects on SCG by steepening the dispersion curve, and possibly creating a second ZDW [85,89,90,94,95]. The latter, as will be explained in Section 4.5.3, effectively limits spectral broadening and is thus in most cases undesirable. For this reason it is important to verify the dispersion of waveguides for SCG. In many cases the dispersion can be calculated using numerical modelling based on the fiber geometry and Sellmeier coefficients for the refractive index. However, often there is no refractive index data for the specific glass, and the exact compositional stoichiometry and geometry of novel glasses may be difficult to control, so it was vital to our activities that we were able to measure the dispersion of the actual drawn fibers. The following section presents our work with measuring and calculating the dispersion of fibers and waveguides.

3.3 WAVEGUIDE DISPERSION MEASUREMENTS

There are many techniques for measuring the refractive index of bulk materials, such as ellipsometry, refractometry, and phase-contrast microscopy. It has long been standard approach to measure the refractive index of bulk glasses, and then use these values to calculate the dispersion of fibers and waveguides, but one possible issue with surface techniques, such as ellipsometry, is that even high quality polished glasses have a top layer of oxidized glass, which could lead to faulty measurements. In any case it is of great interest to be able to measure not only bulk glasses, but also waveguides, which may be achieved using white-light interferometry. The experimental setup we adopted for measuring the dispersion is shown in Figure 3.3.1, and comprises a broadband mid-IR SC source from NKT Photonics (~1.3-4.5 μm), a balanced Mach-Zehnder free-space interferometer, and a fiber-coupled scanning spectrometer (0.4-5.0 μm).

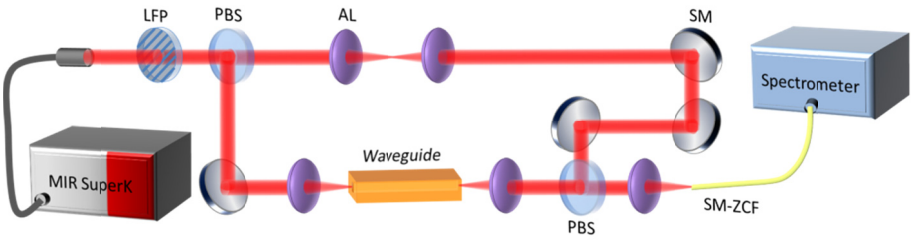

Figure 3.3.1: Experimental setup for measuring waveguide dispersion using a mid-IR supercontinuum source and a balanced Mach-Zehnder interferometer (LFP: Linear film polarizer, PBS: Plate beam splitter, AL: Aspheric lens, SM: Silver mirror, SM-ZCF: Single-mode ZBLAN collecting fiber).

The principle works by splitting the beam into a reference and sample arm that travels through the air and sample, respectively. The optical path difference (OPD) between the two arms is then given by:

$$\mathrm{OPD}(\lambda) = L - l - n(\lambda)\mathrm{z} \tag{3.3.1}$$

where L is the path length in air of the reference arm, l is the path length in air of the sample arm, and z is the sample length. When the two arms are combined the difference in phase-delay over the bandwidth of the source due to dispersion of the sample gives rise to a wavelength dependent interference pattern [96–98]:

$$I(\lambda) = I_r(\lambda) + I_s(\lambda) + 2\sqrt{I_r(\lambda)I_s(\lambda)}\cos(\Phi(\lambda)) \tag{3.3.2}$$

The resulting interference maxima satisfies the relation [98]:

$$\mathrm{OPD}(\lambda) = m\lambda \tag{3.3.3}$$

where m is the integer 2π-ambiguous interference order of a given maxima. The period of the interference fringes becomes greater as the OPD is reduced, and becomes infinite at the so-called phase equalization wavelength (λ_{eq}), where the OPD of the two beams are the same.

The effective refractive index can be well approximated by a Laurent polynomial [98]:

$$n(\lambda) = A_1\lambda^{-4} + A_2\lambda^{-2} + A_3 + A_4\lambda^2 + A_5\lambda^4 \tag{3.3.4}$$

And by combining eqs. (3.3.1), (3.3.3), and (3.3.4) the following expression is given:

$$a_1\lambda^{-5} + a_2\lambda^{-3} + a_3\lambda^{-1} + a_4\lambda + a_5\lambda^3 = m \tag{3.3.5}$$

where $a_1 = -A_1 z, a_2 = -A_2 z, a_3 = L - l - A_3 z,$ and $a_4 = -A_4 z$. By least squares fitting of eq. (3.3.5) with the wavelength dependence of the interference maxima, the dispersion can be evaluated from the relation [98]:

$$D(\lambda) = \frac{1}{c}(-20A_1\lambda^{-5} - 6A_2\lambda^{-3} - 2A_4\lambda - 12A_5\lambda^3) \tag{3.3.6}$$

Thus, using this technique one needs simply record a single the interference spectrum and measure the length of the sample to calculate the dispersion. The benefit of this method is dense wavelength sampling, and measurement speed. The accuracy of this technique evidently depends on the quality of the fit, which is affected by the number of visible fringes and the shape of the phase function. The accuracy also deteriorates towards the boundaries of the fit due to increasing shape uncertainty and limitations of the fit. This uncertainty can to some degree be mitigated by averaging over multiple measurements with different λ_{eq}, each of which should result in a slightly different shape near the ends of the dispersion curve, thus providing a gauge of the uncertainty and a most probable mean value.

3.3.1 Experimental results

As outlined in Figure 3.3.1 light was coupled to and collimated from the waveguides by aspheric lenses, and the two interfering beams were collected using a single-mode ZBLAN optical fiber. To avoid contribution to the measured dispersion from the optics, the interferometer was balanced by placing the same two aspheric lenses in the reference beam path, and by having each beam transmitted and reflected the same number of times from the beam splitters. Proper guiding was verified by a PbSe focal plane array camera and the transmission was optimized by rotating the polarizer before the first beam splitter.

Figure 3.3.2 shows a typical interference spectrum obtained by placing a step-index ZBLAN fiber in the sample arm, and then changing λ_{eq} by moving the reference mirror. The movement of λ_{eq} with respect to mirror displacement can be used to obtain the sign of the dispersion [99]. Several such ZBLAN fibers with varying core diameters were tested, and the results are summarized in Table 2 and Figure 3.3.3.

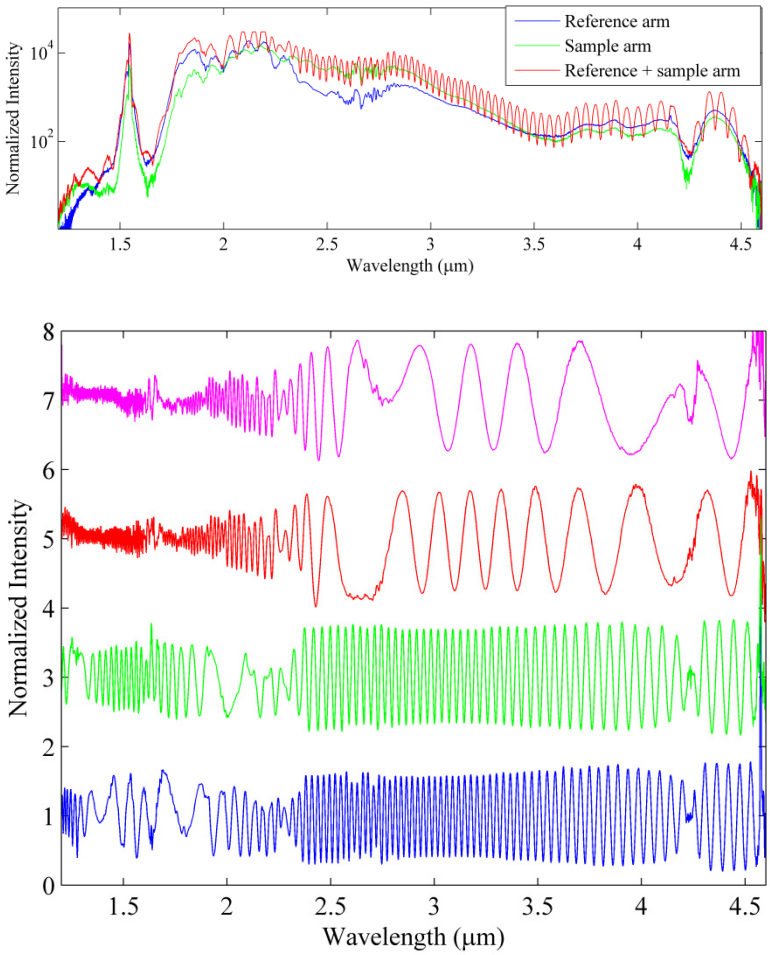

Figure 3.3.2: (Top) Typical spectrum of the reference arm, sample arm, and the interference spectrum from the combination of the two. (Bottom) Normalized interference spectra for four different positions of the reference arm mirror showing the movement of λ_{eq} and corresponding change of the modulation frequency. The spectral feature at 4.2 μm is due to CO2 absorption in the air.

Fiber	D_{core}	±	NA	±	2nd ZDW
ZBLAN A	6	0.3	0.265	0.01	all-normal
ZBLAN B	6.4	0.1	0.265	0.01	3.57
ZBLAN C	6.5	0.1	0.265	0.01	3.97
ZBLAN D	6.7	0.2	0.265	0.01	4.13
ZBLAN E	6.8	0.2	0.265	0.01	4.50
ZBLAN F	6.9	0.7	0.265	0.01	4.43
ZBLAN G	6.9	0.7	0.265	0.01	4.61

Table 2: ZBLAN fiber geometric parameters including specified deviations (±) and measured 2nd ZDW. The results show a steady increase in ZDW with core diameter, as expected.

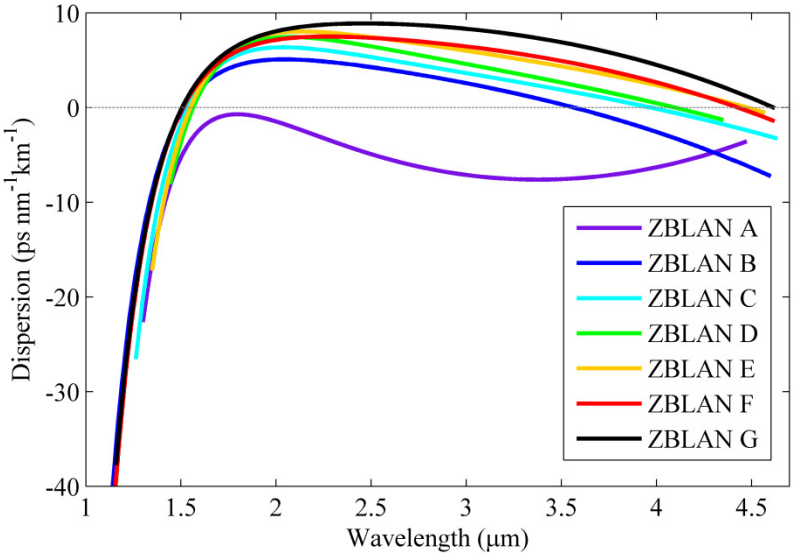

Figure 3.3.3: Dispersion curves for the ZBLAN fibers listed in Table 2, taken over an average of 3-6 dispersion measurements on each fiber.

It can be seen from Figure 3.3.3 that all the fibers, with the exception of ZBLAN A, was found to exhibit a second ZDW, which increased steadily with the core diameter. This was the first time a 2nd ZDW was measured in step-index ZBLAN fibers, and interestingly it was in direct contradiction to the calculated dispersion profiles based on Sellmeier coefficients from Gan et al. [100]. Figure 3.3.4(b) taken from ref. [94] by I. Kubat et al. shows that based on the Sellmeier coefficients from Gan and NA=0.265, there should not be a 2nd ZDW for a core diameter above 5.83

μm, and that the fiber should become all-normal below a core diameter of 5.77 μm. However, the experimental results show clearly a 2nd ZDW in all cases, except for the all-normal case with 6 μm core diameter. This result emphasizes the importance of measuring the actual dispersion of fibers. The reason for this discrepancy is accredited to the complexity of the ZBLAN glass matrix, which means that even slight changes to the glass composition affects the refractive index, and thus NA and dispersion. The impact of the 2nd ZDW in SCG is further elaborated in Section 4.5.3 on cascaded SCG.

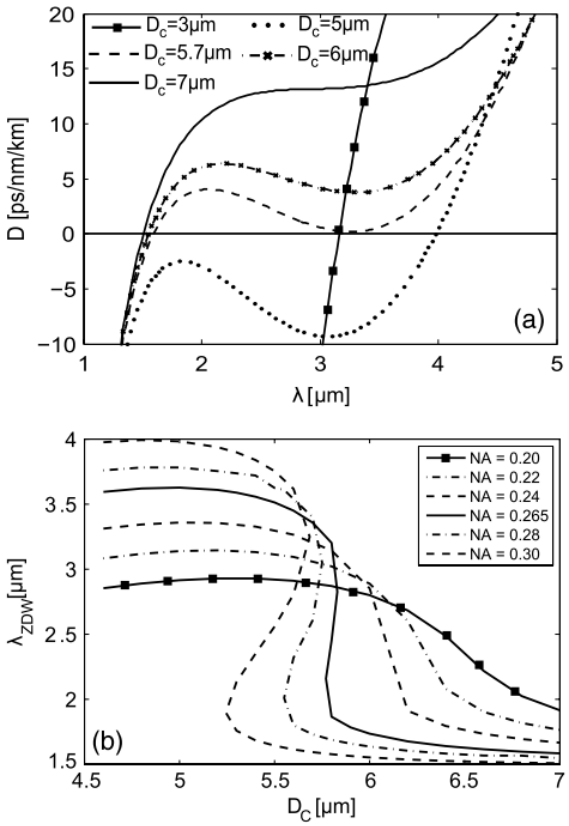

Figure 3.3.4: (Figure by Kubat et al. [94]) Dispersion of ZBLAN fibers modelled using Sellmeier coefficients based on the $(ZrF_4)_{53}(BaF_2)_{20}(LaF_2)_4(AlF_3)_3(NaF)_{20}$ glass matrix, where the subscript denotes % mol. mass. (a) Dispersion for a fiber with NA=0.30 and D_c between 3 and 7 μm. (b) Zero dispersion wavelength λZDW for NA between 0.20 and 0.30 and D_c between 4.5 and 7 μm.

3.4 ULTRAFAST LASER INSCRIBED WAVEGUIDES

(Based on journal paper [I], Ref. [80]*)*

An alternative to thermal drawing, hot embossing and vapor deposition methods for waveguide fabrication is to directly inscribe a waveguide into a bulk glass sample using a technique known as ultrafast laser inscription (ULI). ULI is a powerful technique that relies on the nonlinear interaction of sub-bandgap photons with a transparent dielectric material to induce a permanent increase in refractive index, thus enabling the confinement and guiding of light [101]. The inscription process involves the use of ultrashort pulses focused within a bulk substrate to generate very high intensities at the focal region, thus leading to multiphoton absorption and ionization effects [102]. As a consequence the index modification is highly localized to the focal region, which means that three dimensional structures can be inscribed by translating the sample in x,y,z-directions. However, due to the complex nonlinear spatio-temporal light-matter interaction, the geometrical distribution of the index modification is difficult to control, and the dependence of the refractive index profile with writing parameters, such as scan speed, number of repeated scans, beam power and focusing, is not well understood. For this reason the index modification and dispersion was characterized for a series of gallium lanthanum sulphide (GLS) waveguides fabricated at Heriot-Watt University. The waveguides were fabricated using a mode-locked ytterbium (Yb) doped fiber laser delivering 360 fs pulses with a central wavelength of 1.045 μm and repetition rate of 500 kHz. The substrates were mounted on air bearing Aerotech stages and the beam was focused inside the substrates to a depth of 240 μm from the top surface using either 0.4 NA or 0.6 NA aspheric lenses. The pulse energies incident on the sample varied from 52 to 110 nJ and four different translation speeds of 1, 4, 8, and 12 mm/s was used with the substrates being moved perpendicular to the laser beam direction. The multi-scan inscription technique was used yielding waveguides with rectangular cross-sections. After fabrication the input and output facets of the substrates were polished to optical quality.

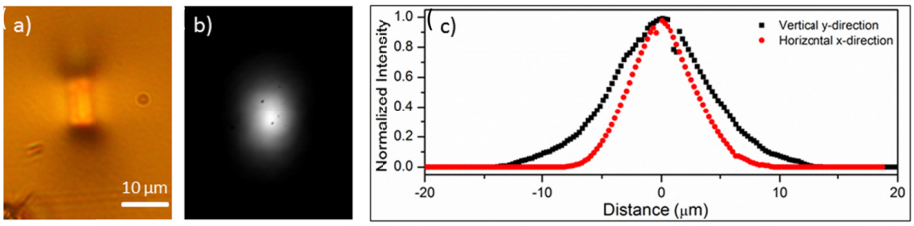

Figure 3.4.1: (a) Microscope image of a ULI waveguide 3 taken in transmission mode, (b) near-field profile of the waveguide pumped at 1.55 µm, and (c) the corresponding intensity cross-sections at 1.55 µm.

Figure 3.4.1 shows a microscope image of a rectangular waveguide inscribed in GLS along with the near-field profile and intensity cross-section. It is apparent from Figure 3.4.1(a) that besides the rectangular modification that represents the waveguide, there is some additional modification of the material along the edges of the waveguide. The index variation was investigated by quantitative phase microscopy along the horizontal axis of the waveguide, as seen in Figure 3.4.2(c), and the result for five waveguides of increasing width, but otherwise identical writing parameters, is shown in Figure 3.4.2(a). It is clear from the graphs that the refractive index is modified beyond the geometrical boundaries of the waveguides, and the oscillation of the refractive index below and then above the bulk refractive index is ascribed to the induced stress from the densification of the waveguide region [48].

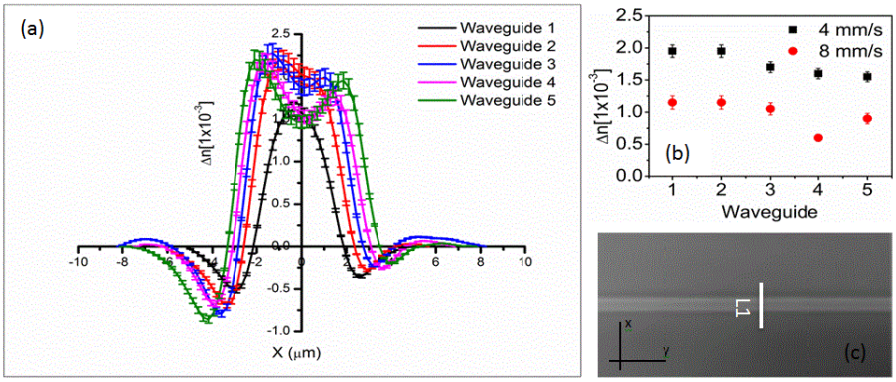

Figure 3.4.2: (a) Refractive index profiles along the line L1 shown in (c) of 5 waveguides of different widths inscribed with pulse energy 72nJ and translation speed 12mm/s using a 0.6 NA aspheric lens. (b) Maximum Refractive index increase of two sets of waveguides (red and black) inscribed with different translation speeds using again a 0.6 NA aspheric lens and a pulse energy of 94 nJ. (c) Top view of a GLS waveguide with the line L1 along which the refractive index profile Δn(x) is measured.

The waveguides were inscribed with a pulse energy of 72 nJ and a sample translation speed of 12mm/s using a 0.6 NA aspheric lens. Each waveguide was fabricated with a different number of scans thus yielding waveguides of different sizes with waveguide 1 having the smallest cross-section and waveguide 5 having the largest cross-section. Waveguide 1 was measured to have a width of about 4 μm and every subsequent waveguide was 0.66 μm wider than the previous one so that the widest waveguide had a width of about 6.6 μm. The height was the same for all waveguides, about 18 μm. Figure 3.4.2(b) presents the maximum index modification of the five waveguides using a different translation speed of 4 and 8 mm/s, which shows the increase in refractive index modification due to the longer exposure time.

The confinement properties of the fabricated waveguides was investigated by importing the measured x-axis refractive index profiles into the commercially available COMSOL Multiphysics software. Figure 3.4.3(a) shows the imported refractive index profile of waveguide 3 from Figure 3.4.2(a). The inset shows the waveguide model cross-section, which assumes no y-axis variation in the refractive index since this data was not available. Figure 3.4.3(b) shows the calculated normalized electric field profile of the fundamental mode at 1.55 μm [48].

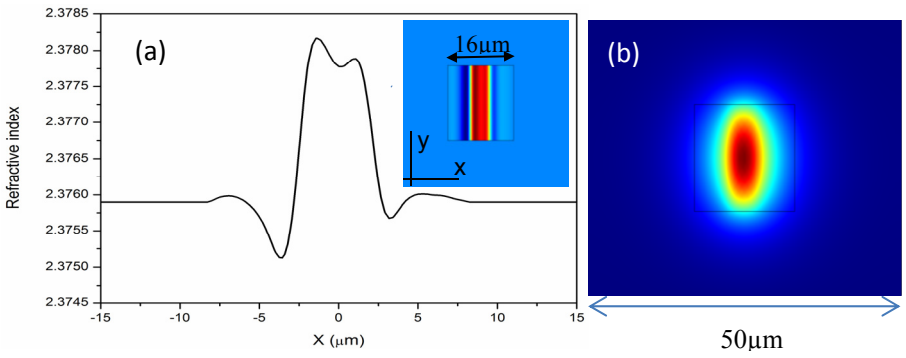

Figure 3.4.3: (a) Measured refractive index profile along the x-axis of waveguide 3, and the inset shows the modelled 2D cross-section of the waveguide imported into Comsol. (b) Calculated mode profile of the fundamental mode at 1.55 μm for the imported waveguide geometry.

It is interesting to note that the obtained electric field profile is to a good approximation symmetric despite the asymmetric index distribution of the waveguide. This is due to the fact that at 1.55 μm the effective index

of the fundamental mode is $n_{eff} \sim 2.3764$, which is well confined to the symmetric region of the waveguide. However, at shorter wavelengths, we could observe asymmetry in the electric field profile. The numerical modelling was in very good qualitative agreement with the imaged near field profile of the waveguide shown in Figure 3.4.1(b). The experimentally measured $1/e^2$ mode field diameters for the waveguide were found to be 10.98 ± 1.15 μm in the x-axis and 17.68 ± 2 μm in the y-axis, as seen in Figure 3.4.1(c), which is also in very good quantitative agreement with the theoretically simulated MFDs, thereby supporting the validity of the refractive index profiles.

The weaker refractive index modification of waveguide 1 also manifested in the transmission spectrum. Figure 3.4.4 shows the output spectra obtained by launching the NKT ZBLAN SC source into waveguides 1, 2, and 3, which clearly shows that waveguide 1 exhibits very poor long-wavelength transmission. It should be noted that the waveguide also show a lower baseline transmission at shorter wavelengths due to reduced coupling to the smaller core, but still the effect of confinement loss is clear.

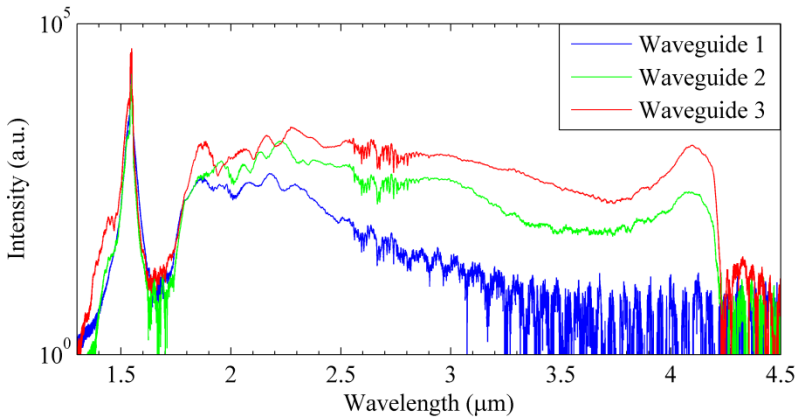

Figure 3.4.4: Output spectrum of the NKT ZBLAN SC source launched into waveguides 1 to 3, which were inscribed with the same inscription parameters, but with increasing widths of around 3, 5, and 7 μm, respectively. The high confinement losses of waveguide 1, which is assumed to be due to a lower index modification, is clearly seen from the poor long-wavelength transmission.

The dispersion of the bulk GLS and inscribed waveguides was also measured using the technique described in section 3.3. Figure 3.4.5(a) shows the measured dispersion of the bulk glass substrate compared to

the dispersion of two waveguides with the same dimensions but fabricated using different NA inscription lenses [80].

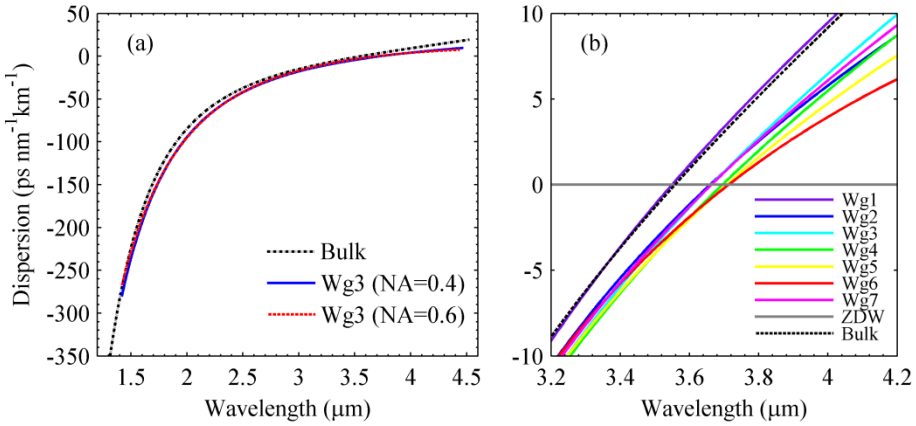

Figure 3.4.5: (a) Comparison of the measured dispersion of the bulk glass and two waveguides of identical dimensions but fabricated using different focusing lens NA and different pulse energy. (b) Zoomed-in view of the dispersion around the ZDW of the bulk glass and seven waveguides inscribed with the same parameters but having increasing cross-sections with waveguide 1 having the smallest cross section and waveguide 7 having the largest one.

For the waveguide inscribed with the 0.4 NA aspheric lens a pulse energy of 64 nJ and sample translation speed of 12mm/s was used, while for the waveguide inscribed with the 0.6 NA aspheric lens the pulse energy was 110 nJ and sample translation speed 12mm/s. From Figure 3.4.5(a) it is seen that the dispersion of the waveguides is very similar to that of the bulk glass, with negligible impact from changing the inscription parameters, such as, the NA of the inscription lens and the pulse energy. Figure 3.4.5(b) shows a zoomed-in view of the measured dispersion near the ZDW region of seven different waveguides, which all, except for waveguide 1, are seen to have almost identical dispersion curves. The waveguides were inscribed with a pulse energy of 110nJ and a sample translation speed of 12mm/s using a 0.6 NA aspheric lens, but they were chosen to have increasing widths with waveguide 1 being the narrowest and waveguide 7 being the widest. Waveguide 1 was measured to have a width of about 3 μm and every subsequent waveguide was 1.98 μm wider than the previous one so that the widest waveguide had a width of about 15 μm. The height was the same for all waveguides, about 18 μm. The bulk glass ZDW was identified to be around 3.61 μm, and for

waveguide 1 the ZDW was at 3.55 μm, whereas the other six waveguides had a measured ZDW between 3.66 and 3.71 μm. The divergence of the dispersion curves at the long-wavelength edge of the spectrum is assumed to be primarily due to the limitations of the fit over a broad spectral range. The discrepancy between the ZDW of waveguide 1 and waveguides 2-7 verifies the measured weak index modification of waveguide 1 and the observed high confinement losses. Modelling revealed that the waveguide dispersion is indeed very small (1.77 ps nm^{-1}1 at 2.5 μm), hence the total dispersion in the waveguides will be dominated by material dispersion, which is in agreement with the experimental observations.

In conclusion, these waveguides may have potential for compact, tailored devices, such as couplers, circuits, switches or wavelength converters, but they are currently limited in transmission up to around 5 μm due to a weak index modification and hence not suitable for longwaver mid-IR SCG. It is expected that further optimization of inscription parameters and possibly new substrates will enable waveguides with better confinement.

3.5 END-FACET NANOIMPRINT LITHOGRAPHY

As mentioned in the discussion of chalcogenide glass properties, the high refractive index result in a significant part of the incident light being reflected at the air-glass interface. The reflectance is calculated from the Fresnel equations, and for normal incidence it reduces to [39]:

$$R = \left| \frac{n_{\text{air}} - n_{\text{glass}}}{n_{\text{air}} + n_{\text{glass}}} \right|^2 \tag{3.5.1}$$

which for an air-As_2Se_3 interface results in $R = 0.228$, and so about 23 % of the light is lost at the input and output of the fiber. It is therefore crucial for applications involving chalcogenide fibers and devices to be able to reduce this loss to a minimum. Traditionally, anti-reflection (AR) coatings has been employed, in which a number of layers of dielectric thin-films is deposited at the interfaces to provide either a graded-index profile or destructive interference in the backwards direction. However, deposition of AR thin-film coatings can be impractical for long lengths of

fiber, and tend to reduce the damage threshold of the fiber due to surface imperfections, mismatch of thermal coefficients, or adhesive failure between the layers due to sub-optimal deposition temperature imposed by the vacuum deposition chamber [75,103]. Alternatively, AR structures may be imprinted into the end-facets through a technique known as nanoimprint lithography (NIL) or hot embossing [76]. NIL offers a potentially fast, flexible, and low-cost processing for various glass optical components such as lenses, diffraction gratings, and optical waveguides [71,75]. Furthermore, AR structures have been demonstrated to improve the laser damage threshold of untreated chalcogenide glasses and cleaved fibers, possibly through irradiance enhancement at the air side of the interface, and elimination of absorbing surface fects [74,103–105]. For these reasons NIL of chalcogenide fiber end-facets was investigated.

AR structures are basically periodic subwavelength gratings that do not diffract light in the classical sense as long as the period is shorter than the wavelength of light [106]. Figure 3.5.1 shows a simple example of such a grating structure, where Λ is the grating pitch, w is the width, and d is the height of the periodic structure. According to scalar diffraction theory the reflectivity of a substrate covered with a thin film has zero reflection provided that two conditions are met: The reflected waves from the two interfaces between air-film and film-substrate should be of equal amplitude and with a half-wavelength phase shift between them [106].

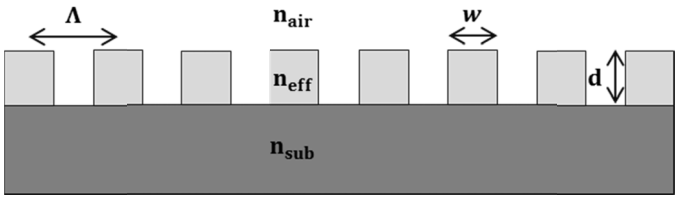

Figure 3.5.1: Basic design parameters of a periodic subwavelength AR structure. Parameters Λ, w and d is the pitch, width, and depth of the protrusions, respectively. The effective refractive index of the interface between air and substrate depends on these parameters, as well as the duty cycle or filling ratio of the structure.

The same conditions can be applied for a periodic structure, if the structure is approximated as a layer of effective refractive index n_{eff} between the air and substrate indices. From the Fresnel formula the reflec-

tion at normal incidence from the interfaces is seen to depend only on the ratio of the refractive indices, leading to the following criteria [106,107]:

$$n_{eff} = \sqrt{n_{air} n_{sub}} \tag{3.5.2}$$

$$d = \lambda/4\, n_{eff}. \tag{3.5.3}$$

$$(n_{eff} - 1) = (n_2 - 1)DC \tag{3.5.4}$$

where $DC = w/\Lambda$ is the duty cycle or filling ratio of the structure. If we assume the substrate is $As_{40}Se_{60}$ with $n_2 = 2.77$ we obtain the criteria $n_{eff} = 1.66$ from Eq. (3.5.2), which inserted into Eq. (3.5.4) results in DC = 0.38. This means that in order to get good anti-reflective properties at $\lambda = 4.4$ µm, the depth must be d = 1.83 µm according to Eq. (3.5.3). These simple equations gives a good indication of which design parameters to use for a specific substrate and wavelength, however, solving Maxwell's equations under the boundary conditions of the real 3D structure is needed for accurate results, but this is outside the scope of the work.

3.5.1 Experimental results

The setup used for NIL of chalcogenide fibers is shown in Figure 3.5.2. The fibers were fixed to a v-grooved force sensor and manually pressed into the AR structure by a vertical translation stage in order to monitor the applied force. The AR structure was placed on a heater connected to a temperature monitor and controller. The entire setup was kept under fume extraction, and later an argon flow was added to reduce the possibility of hydrolysis and oxidation of the glass during imprinting.

Figure 3.5.3 shows an example of an imprint session in which the temperature and applied force is varied over time, which illustrates the interaction and free-parameter space involved in NIL. First the fiber was pressed against the structure, and then the temperature was gradually increased. As the glass become less viscous close to T_g the force was gradually relieved through the viscous flow of the glass giving way to the structure. The force could be increased manually by translating the fiber further to compensate the flow or kept low during some imprint-

ing time, after which the structure was cooled and the fiber released. In such a procedure even slight temperature changes can have a significant impact on the imprint depth and feature quality [73].

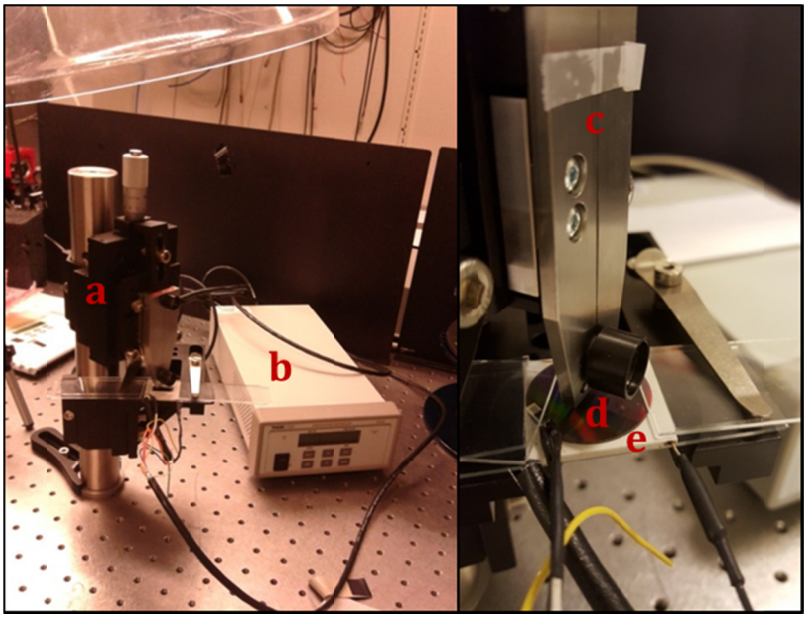

Figure 3.5.2: Setup for nanoimprinting of fiber end-facets. Left: a): Translation setup detailed in the right window, b) temperature controller. Right: c), v-grooved force sensor, d) silicon wafer with the imprint structure, e) ceramic heater connected to b.

Figure 3.5.4 shows a series of scanning electron microscope (SEM) images demonstrating how small changes in the temperature close to T_g can have a significant impact on the result of the imprint. As the temperature was increased beyond T_g of both the core and cladding (~180-185° C) the core of the fiber began to protrude from the cladding, exhibiting relatively deep and clear imprinting features compared to the cladding, which remained largely unaffected. This was a first indicating that the viscosity of the cladding glass was significantly higher at these temperatures.

The imprint temperature was found to be more critical than the applied force, and in many cases increasing the applied force simply led to deformation of the macrostructure of the fiber. In the case of the $Ge_{10}As_{22}Se_{68}$ PCF in Figure 3.5.5 the increased force resulted in collapse of the air-holes and an “elephants foot” deformation of the fiber tip.

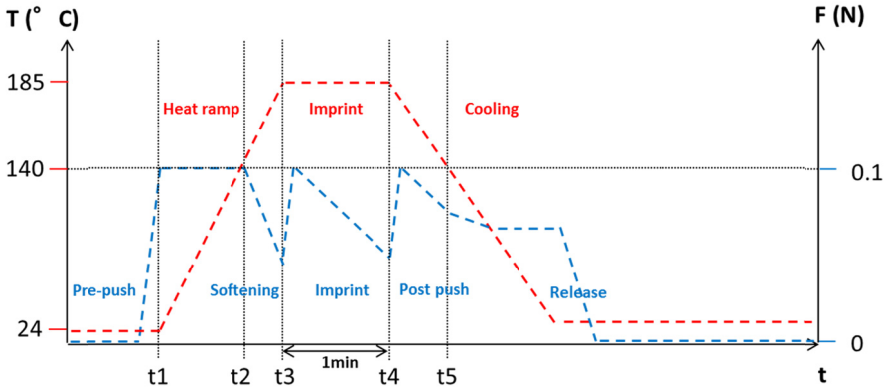

Figure 3.5.3: Example of an imprint session displaying the interplay between the three major parameters: time, temperature (red curve), and applied force (blue curve).

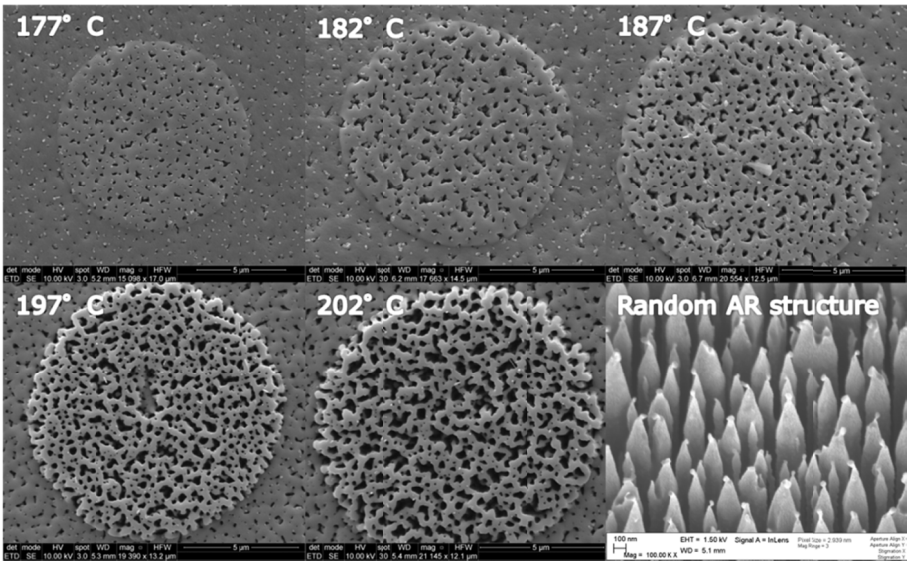

Figure 3.5.4: SEM images showing the effect of increasing temperature on the imprinting features and core protrusion for a random AR structure on a 11 μm diameter $As_{40}Se_{60}$ core $Ge_{10}As_{23.4}Se_{66.6}$ clad fiber. Note that the pictures have different magnification. From top left to the right the values of magnification are: 15098, 17663, 20554, 19390, and 21145. Bottom right picture shows the random cone-like AR structure.

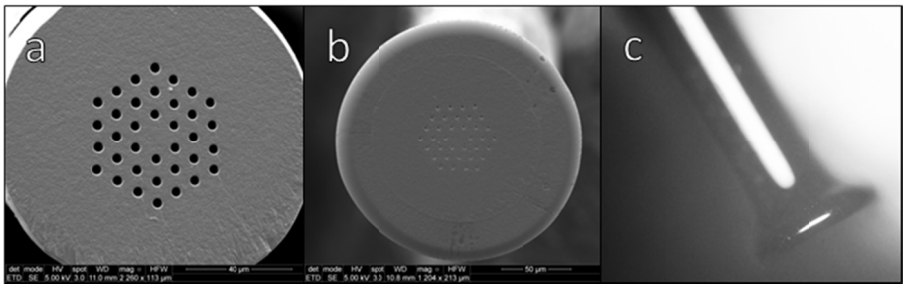

Figure 3.5.5: SEM images showing the effect of increasing the applied force. (a) Failed imprint due to high viscosity in a $Ge_{10}As_{22}Se_{68}$ PCF at 202° C with same applied force as in Figure 3.5.4, and (b) with three times larger applied force with visible macrodeformation of the fiber end-facet. (c) Side-view of the fiber macrodeformation.

In order to better study how well the structure was imprinted into the glass the random AR structure was replaced with a uniform and periodic flat pillar structure, as seen in Figure 3.5.6(a). The structure had approximately $\Lambda = 1.25$ µm , $w = 0.98$ µm, and $d = 0.6$ µm, making the structure optimized around $\lambda = 4$ µm (see Figure 3.5.6(b)). The structure was imprinted into $As_{40}Se_{60}$ core / $Ge_{10}As_{23.4}Se_{66.6}$ cladding SIFs, and SEM images of the imprinted holes into the a small-core (11 µm) and large-core (288 µm) fiber is shown in Figure 3.5.6(c) and (d), respectively. The SEM images revealed a clear periodic imprint with well-defined features in good qualitative agreement with the master structure. However, from the SEM it was hard to evaluate the depth of the imprinted structure, and so the samples were investigated further using atomic force microscopy (AFM). Figure 3.5.7(a) shows the custom-made polymer fiber holder (black rectangle) that was squeezed from one side with a screw in order to hold the fiber in the upright position needed for the AFM probe. The result of AFM on the small-core fiber is 3D visualized in Figure 3.5.7(b), and the cross-sectional analysis in Figure 3.5.7(c,d) revealed about 540 nm penetration in the cladding and at least 700 nm penetration in the core glass. The exact penetration into the core glass is uncertain due to the lack of a flat baseline, which means that in principle the needle may not have touched the bottom of the cavity. The cladding penetration was almost equal to the height of the pillars, which was around 600 nm, indicating that the core was subject to re-flow after release. It is therefore possible that the fiber tip was not cooled sufficiently below T_g before release, or the fiber was slipping slightly in the v-groove during imprinting.

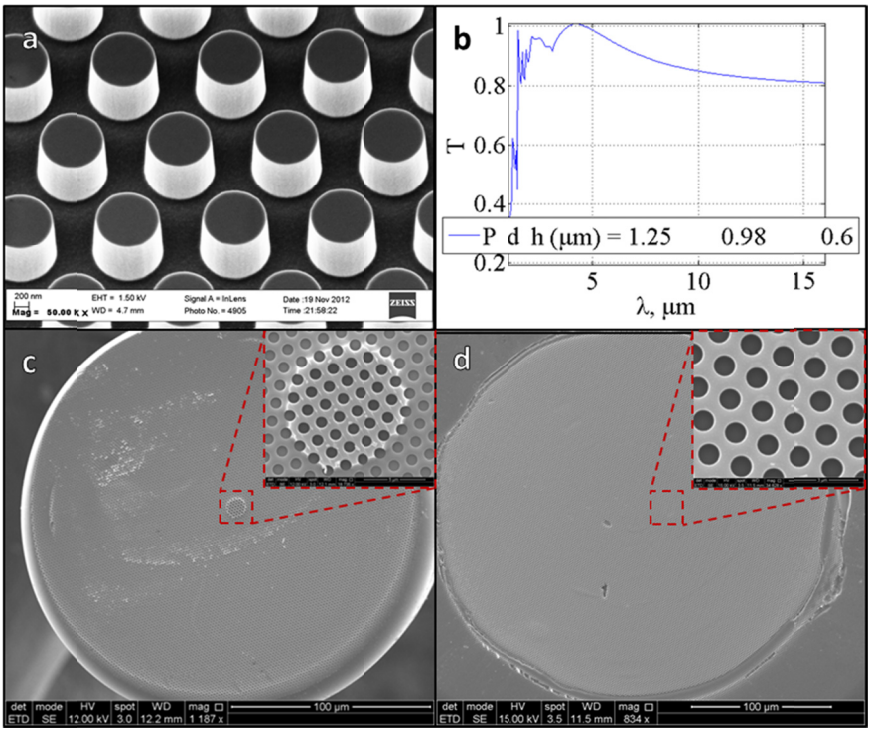

Figure 3.5.6: (a) SEM image of the AR silicon pillar structure. (b) Calculated transmittance of the silicon stamp for n=2.77, pillar pitch, diameter, and height of 1.25 μm, 0.98 μm, and 0.6 μm, respectively (Data from DTU Nanotech). (c,d) SEM images of imprinted pillar structure in a small-core (11 μm) and large-core (288 μm) fiber, respectively.

Re-flow is also visible from the rounding structure seen in Figure 3.5.7(c), which may be advantageous due to the formation of a smoother index transition from air to glass.

The antireflective properties of the pillar-imprint were characterized by measuring the power transmitted through a short piece of the larg-core $As_{40}Se_{60}$ fiber. The light source for the experiment is described in Section 4.3.1. Briefly it is a ~300 fs pulsed laser operating at 4.4 μm with 21 MHz repetition rate, and thus with relatively low peak power. Combined with the large core diameter of the fiber the nonlinearity was negligible, and indeed no spectral broadening was observed at the pump power of 100 mW, so propagation was assumed to be linear. The transmission was measured for two fibers in three configurations: 1) before imprint, 2) with imprint on the input facet, and 3) with imprint on the input and output facets, and the results are shown in Figure 3.5.8.

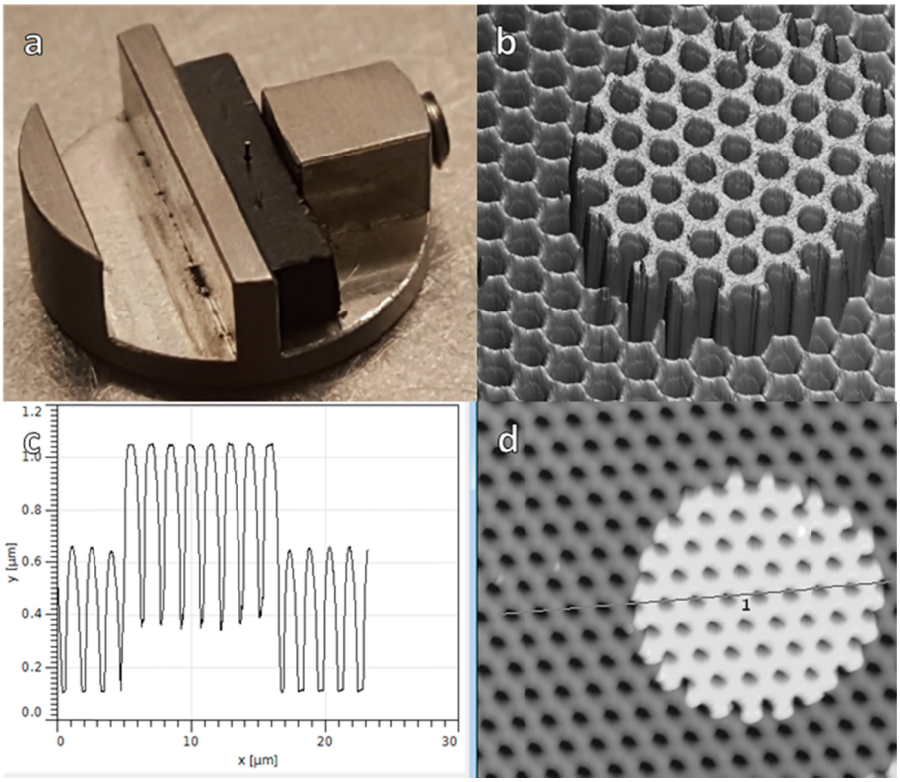

Figure 3.5.7: a) Picture of the fiber mounted with in the black polymer holder with the facet upwards. The fiber is fixed by applying force on the polymer through a screw on the side of the circular AFM sample holder. b) 3D visualization of the AFM results. c) Cross-sectional depth profile corresponding to the line in (d).

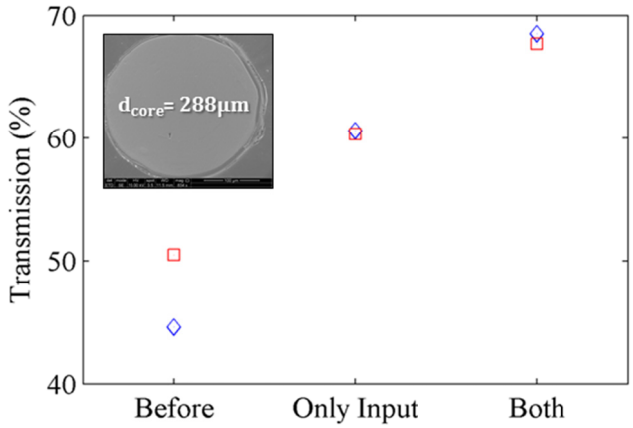

Figure 3.5.8: Transmission data for the 288 µm core fiber imprinted with the pillar AR structure, showing the transmission before imprint, with only the input facet imprinted, and with both input and output facets imprinted.

The 44.6 % transmission outlier in Figure 3.5.8 for the untreated fiber is a result of the fiber breaking after the *Before* measurement, so the reduced transmission was likely due to a bad cleave or similar. The fact that the transmission after re-cleaving was almost identical to that of the other fiber confirms this. The result remains that the transmission was increased from 50.5 % to 67.7 %, with the maximum transmission from the first experiment at 68.5 %. This moderate increase of ~18 % was enough to establish proof-of-principle, and together with DTU Nanotech we have already devised several improvements, including automated control and monitoring of the imprint parameters, in order to record the imprint sessions and obtain experimental figures similar to Figure 3.5.3. New structures has also been fabricated by Mikkel Lotz from DTU Nanotech, and Figure 3.5.9 show an example of the first test imprints using the new optimized "moth-eye-like" structures in the large-core As_2Se_3 fiber, which should offer AR properties over a broad bandwidth [108]. Our results with NIL on $As_{40}Se_{60}$ fibers will be presented at the Micro and Nano Engineering 2016 conference.

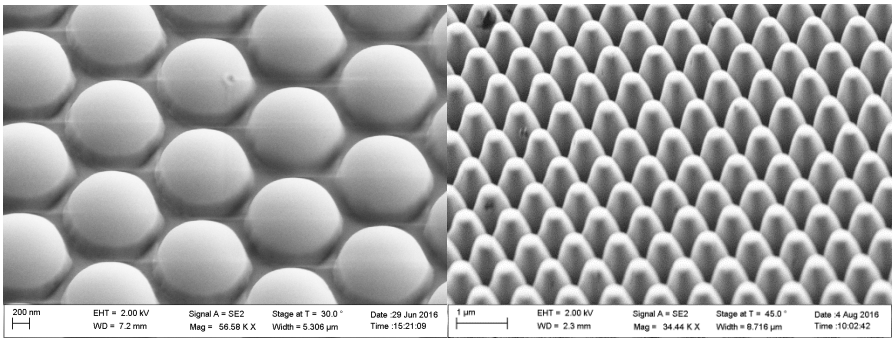

Figure 3.5.9: First test imprints in the large-core As_2Se_3 fiber using new "moth-eye" structures, optimized to have a more smooth and parabolic curvature.

3.5.2 Nanoimprinting as a Tool for Fiber Inspection

Another interesting feature about diffraction gratings, is that the reflected angle of diffraction is not only wavelength dependent, but also dependent on the refractive index of the medium. This is expressed through the scalar grating equation [39,105]:

$$n_{sub}\sin(\theta_m) = n_{air}\sin(\theta_i) + \frac{m\lambda}{\Lambda} \tag{3.5.5}$$

Where θ_m is the angle of diffraction for the m'th order of diffraction, and θ_i is the angle of incidence. The implication is that if an imprinted inhomogeneous substrate is illuminated with white light from e.g. a microscope lamp, the color reflected by a region of refractive index n_1 will be perceived as slightly different compared to a region with $n_1 \pm \Delta n$. This allows us to visualize very subtle inhomogeneities in the refractive index, which may be very difficult to detect otherwise. Figure 3.5.10 shows an example of five imprinted and one un-imprinted large-core fibers as perceived through an optical microscope in reflection mode with a 10× magnification objective. The green circles highlight a region with a distinct "Nike"-like color contrast, which is seen to repeat for all five imprints. In fact, all of the areas circled with red in the top-left imprint also repeat in the other imprints.

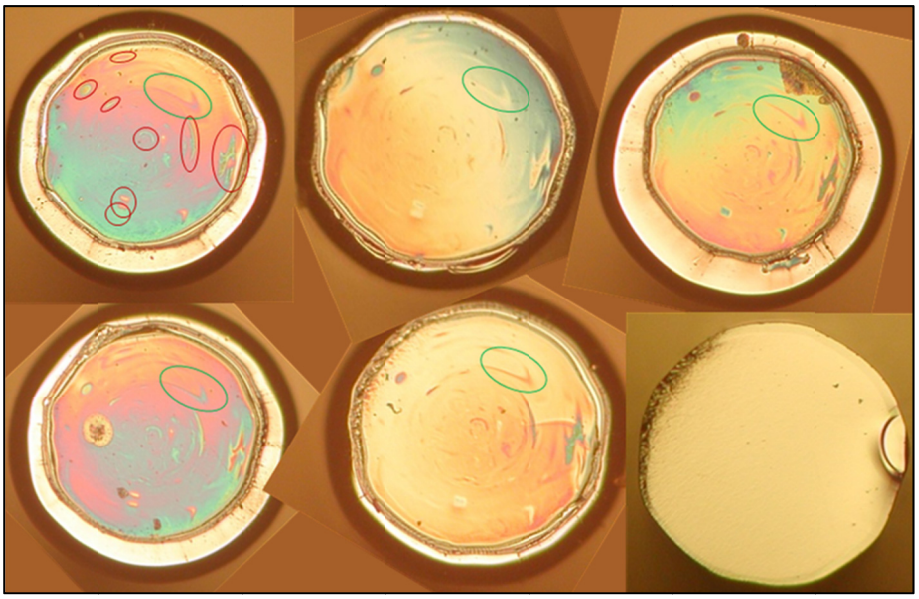

Figure 3.5.10: Microscope reflection images (10× magnification) of five imprinted large-core As_2Se_3 fibers, and one un-imprinted fiber (bottom right). The colors observed are due the wavelength dependence on the angle of diffraction of the white light reflected from the facet. The green ring indicates a distinct "Nike"-like color contrast appearing in all the imprints, and the red rings in the top-left imprint shows other features that visible in all of the imprints.

One could easily suspect that such features was introduced by the master structure, but since the v-groove rig is manually dismounted between each imprint it is practically impossible for the five fibers to all

have been in contact with the same area on the wafer during imprinting, and so it must be an intrinsic property of the fiber. To further demonstrate that the observed color contrast patterns are indeed an intrinsic feature of the fiber a set of small-core fibers were similarly imprinted and inspected using white-light microscopy. Figure 3.5.11 show a set of three imprinted fibers with red circles added once again to highlight some of the repeating patterns. One rather interesting feature is the streamlines seen most clearly in the bottom of the middle imprint, which indicates that some stress possibly due to rapid cooling during viscous flow was frozen into the glass. Even though such inhomogeneous features are all in the cladding, their presence could contribute to inhomogeneity in the core-cladding interface, which as explained in Section 2.1.4 leads to microdeformation loss, and in the worst case macrodeformation of the core. Such analysis could help in the optimization of process involved with the drawing and post-processing of fibers.

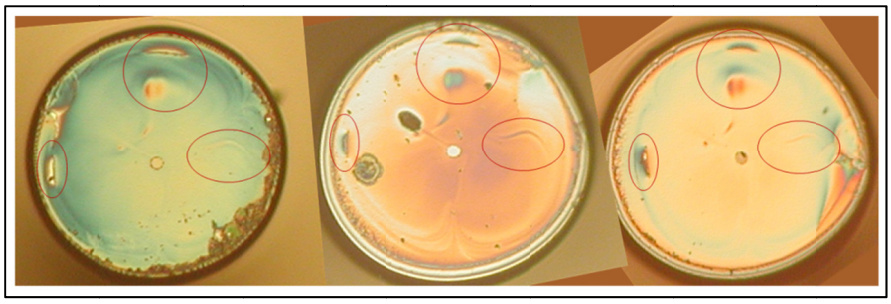

Figure 3.5.11: Microscope reflection images (10× magnification) of three imprinted small-core As_2Se_3 fibers, with red rings highlighting some of the recurring features due to the nanoimprint.

The last example is from a fiber with an AsSe core and GeAsS cladding, which was found to have very high transmission loss, and exhibit strange guiding around the core in SC experiments. For this reason the fiber was tested in an attempt to figure out the cause of these effects. Figure 3.5.12 show that after imprinting the fiber (middle) a dark halo was observed around the core, indicating a change in the refractive index around the core. If this index change is positive, it could explain why the fiber seemed to guide in a region around the core. Since the cladding was a sulphide-based glass, which appears orange to the human eye, it was possible to obtain a microscope image in transmission mode through a very short piece of fiber, as seen in the rightmost window of

Figure 3.5.12. The transmission image verified the halo feature, which means that for glasses that do not guide visible light, the imprint can be used as a way of identifying such inhomogeneities in optical fibers.

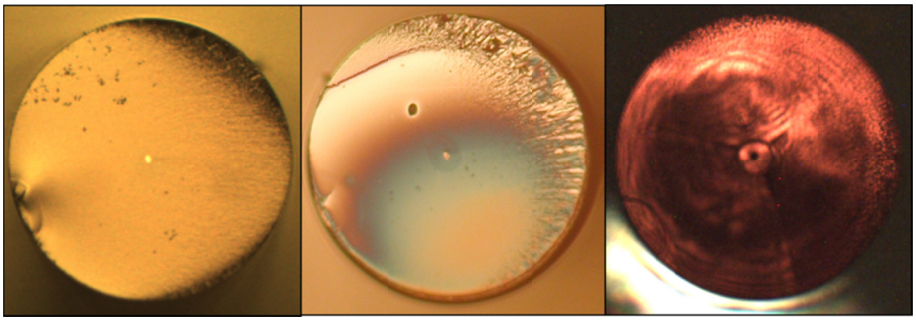

Figure 3.5.12: Comparison between microscope reflection images of the untreated fiber (left), imprinted fiber (middle), and transmission image of the untreated fiber (right). The transmission image verifies the dark halo around the core observed after imprinting.

In conclusion we have demonstrated 18 % increased transmission in AR imprinted $As_{40}Se_{60}$ fibers, and shown how such microstructuring can be used for the investigation of glass inhomogeneities chalcogenide in optical fibers. Imprinted large-core fibers furthermore has the potential for being used as end-caps on small-core fibers to improve the damage threshold. Due to the low required processing temperature NIL is potentially fast, cheap, and practical compared to thin-film deposition or polished Brewster angle connectors.

Chapter 4

Supercontinuum Generation in Chalcogenide Fibers

"I pass with relief from the tossing sea of Cause and Theory to the firm ground of Result and Fact."

— Winston S. Churchill,
The Story of the Malakand Field Force

To date the broadest mid-IR SC reported in literature has been obtained by focusing high peak power fs pulses into a bulk glass sample to obtain extremely high intensities. Using this technique P. Corkum et al. demonstrated as early as 1985 a continuum from 3-14 μm by pumping a 6 cm Cr-doped GaAs with 2.5 ps, ~600 μJ pulses at 9.3 μm from a CO_2 laser [109]. More recently, J. Pigeon *et al.* achieved a continuum from 2-20 μm in a 67 mm GaAs sample also pumped with a CO_2 laser delivering 2 GW peak power 3 ps pulses at 9.3 μm [110]. However, such continuum sources lack spatial coherence and require massive powerful laser systems, limiting the practical applications of this technology. The need for tight focusing in bulk materials limits the nonlinear interaction length, but if instead pulses were launched into a waveguide a relatively high intensity can be maintained over a longer interaction length, meaning that more practical pump systems with lower peak power may be used [111]. In particular optical fibers have the advantage that they can be drawn in great length, have great flexibility, and are compatible with many standard optics components. This Chapter will present the state-of-the-art in mid-IR SCG found in literature and compare it to our own results based on three different pumping schemes.

4.1 INTRODUCTION

The first experimental work with SCG in chalcogenide fibers can be traced back to around 2005 [112]. Back then results were limited by the long ZDW of As-Se glass, and hence much of the subsequent research in the field steered in the direction of As_2S_3 fibers as a highly nonlinear alternative to silica fibers, with the potential for moving further into the mid-IR. Focus was on dispersion engineering and reducing the ZDW in order to pump in the anomalous dispersion regime using mature pump laser technology near the telecom band. This was done by either micro-structured design, by scaling down the fiber core through tapering, or by suspended-core structures. However, experimental results were limited to the 1-5 μm spectral region and with very modest output power [89–91,113]. The first result with high average power up to 565 mW spanning from 1.9-4.8 μm was demonstrated in a As_2S_3 step-index fiber with a 10 μm core diameter by pumping in the normal dispersion regime with a Raman shifted silica fiber laser [114]. This was also the first result with so-called cascaded SCG in a chalcogenide fiber - a topic which will be elaborated on in section 4.5 – but despite these advances results with chalcogenide fibers were being dwarfed by the progress of fluoride fiber-based SCG sources, reaching multi-watt-level output power spanning up to beyond 4.5 μm [63,115–117]. Numerical work had demonstrated the potential for very broadband mid-IR SCG in chalcogenide fibers [118–120], but nonetheless experiments had not been able to exploit the full bandwidth of the chalcogenide glasses. It was not until we demonstrated a record SC bandwidth from 1.4-13.3 μm in an $As_{40}Se_{60}$ SIF [37], then a record long-wavelength average output power of 7.5 mW above 5 μm in an $As_{38}Se_{62}$ suspended-core fiber [82], and lastly the first cascaded SCG to 7 μm [121], that the true potential of chalcogenide fiber-based SCG was made evident.

Since then there has been a rapid development in the field of chalcogenide SCG, with researchers pursuing both longer wavelengths and higher average output power. However, achieving both a long wavelength range and high average power has proved challenging due to the trade-off between peak and average power in most available pump systems, leading to two parallel tracks of development. One that focuses primarily on demonstrating the longest possible wavelengths generated in a fiber, and one that focuses on high average power. The trade-off

between long-wavelength edge and average power is illustrated in Figure 4.1.1, which plots state of the art results in mid-IR SCG found in literature (open circles), against the results presented in this work (solid circles). The state of the art in mid-IR SCG in chalcogenide fibers and waveguides is detailed and referenced in Table 4 of Appendix A. The following sections summarize our progress in realizing broad bandwidth and high average power chalcogenide fiber-based SC sources for use in mid-IR applications.

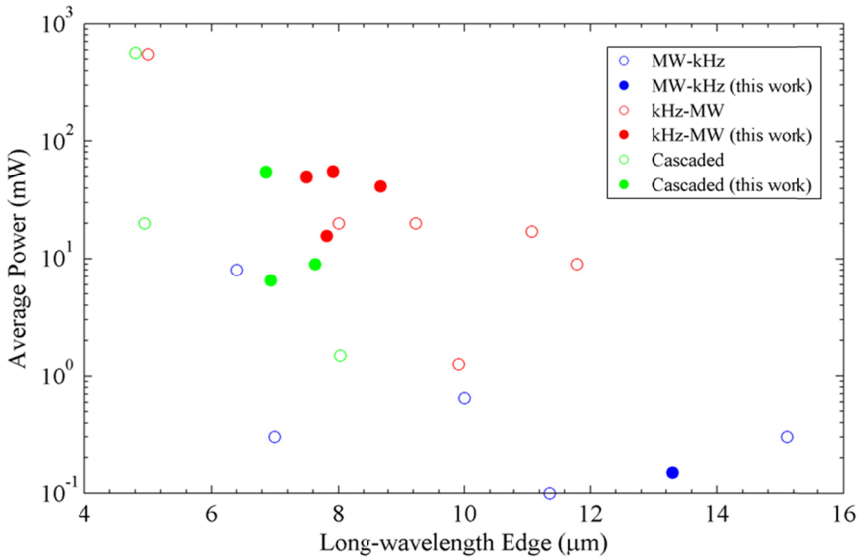

Figure 4.1.1: Overview of state of the art results in mid-IR SCG in chalcogenide fibers with respect to 30 dB long-wavelength edge and average output power. Results found in literature (open circles) is compared to results presented in this work (solid circles), and divided into three pumping regimes: MW-kHz (blue), kW-MHz (red), and cascaded SCG (green).

4.2 MEGAWATT-KILOHERTZ PUMPING SCHEME

(Based on journal paper [IV], Ref. [37]*)*

4.2.1 INTRODUCTION

In order to demonstrate the potential for mid-IR SCG in the fingerprint region, we set up an experiment to pump chalcogenide SIFs with high peak power femtosecond pulses, being the best case scenario in terms of nonlinearity. The chalcogenide glass SIFs were designed specifically for both high numerical aperture and thermal compatibility of the core and cladding glasses. The SIF was fabricated at University of Nottingham via a specially developed multi-stage process of extrusion and preform-drawing, and had had a slightly elliptical ~16μm diameter $As_{40}Se_{60}$ core surrounded by a $Ge_{10}As_{23.4}Se_{66.6}$ cladding. Measurements of the refractive indices of the core and cladding glasses were performed by the company Woollam and are shown in Figure 4.2.1(a) together with the calculated NA. This was the first reported SIF with such a high NA.

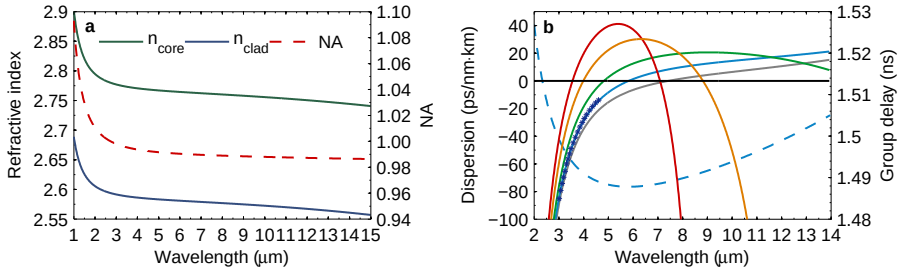

Figure 4.2.1: Measured and calculated chalcogenide fiber parameters. a, Measured refractive indices of the fiber core and cladding glasses together with the calculated NA. b, Calculated dispersion profiles (solid) of the core material (gray) and the four dominant guided modes of the fiber: LP01 (blue), LP11 (green), LP02 (yellow) and LP12 (red) together with the measured dispersion (asterix) and calculated group-delay (dashed) of LP01.

Due to the large core and NA the fiber was effectively multi-moded, and so for this reason we modelled the dispersion of both the fundamental mode (FM) and the three most significant HOMs. The dispersion of these modes is presented in Figure 4.2.1(b), together with the material dispersion of the core glass and the group-delay curve of the FM. The calculated dispersion was verified by measuring the dispersion of the FM from 3.0-4.6 μm, which was found to be in excellent agreement. Be-

low 3 μm the dispersion measurements were obstructed by higher-order mode beating and influence of water vapor absorption ~2.9 μm in the lab atmosphere. The multimode properties were further investigated by sliding window Fourier transform analysis of the measured dispersion data. For a sufficiently narrow spectral window the modulation frequency of the interference is nearly constant, and subsequent Fourier transformation thus gives rise to sharp peak corresponding to a time delay with respect to the reference beam. Any other modulation of the spectrum due to the presence of a higher-order mode (HOM) should therefore result in a second peak, and so by scanning the window across the entire spectrum one can obtain a curve of the delay of each significant mode as a function of wavelength, as shown in Figure 4.2.2(a). The figure clearly shows the presence of at least one significant HOM, which shows good qualitative agreement with the numerical model for the LP11 or LP02 modes shown in Figure 4.2.3. By optimizing the launch conditions significant HOMs could be suppressed, as seen in Figure 4.2.2(b).

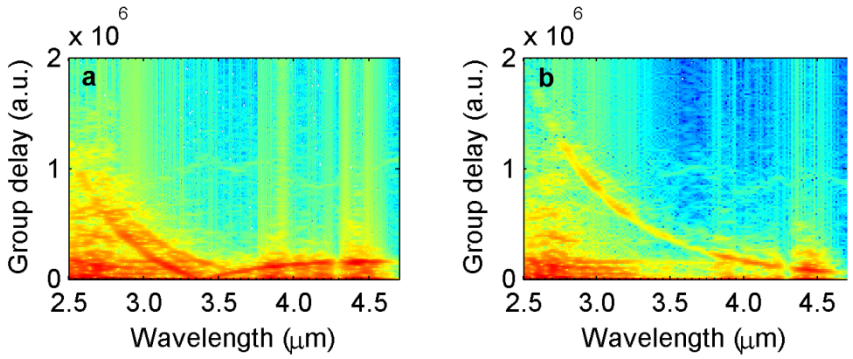

Figure 4.2.2: Spectrograms generated from sliding-window Fourier transformation showing a comparison between the observation of (a) two distinct modes with different group delay curves, and (b) only a single distinct mode, depending on launch conditions.

The fiber FM had a calculated ZDW at 5.83 μm, a low anomalous dispersion towards the longer wavelengths and NA close to unity, which enabled generation of a broad SC with strong confinement to the core. The fiber loss was measured by cut-back of a 288 μm core fiber and using a Fourier transform infrared spectrometer (FTIR). The result is presented in Figure 4.2.4(a) together with the measured absorption of the

laboratory air. The fiber geometry is shown in Figure 4.2.4(b). We pumped the fiber first in the normal dispersion regime at 4.5 µm, which was chosen to fit within the emission band of an envisioned praseodymium (Pr^{3+}) doped chalcogenide fiber laser [122,123], and then compared with pumping in the anomalous dispersion regime at 6.3 µm, which was chosen to coincide with the atmospheric O-H absorption gap, and to avoid the potential impact of the O-H absorption in the fiber on spectral broadening. The idea was, that due to strong nonlinearity and high peak power the light would almost immediately shift away from the pump wavelength, and therefore not be affected by the loss peak [124]. The only potential drawback could be that increased absorption at the end-facet could lead to a lower damage threshold. However, for such high peak power and low average power damage from ionization or molecular dissociation should dominate over thermal damage from absorption [36].

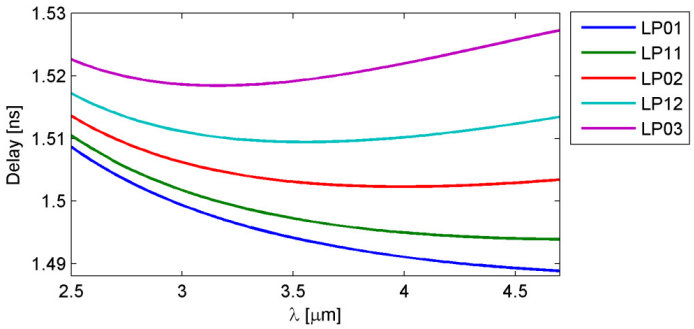

Figure 4.2.3: Modelled fiber group-delay for the five predominant modes. The LP01 and LP11 modes are very close in terms of group delay, similar to what was observed experimentally in Figure 4.2.2(a).

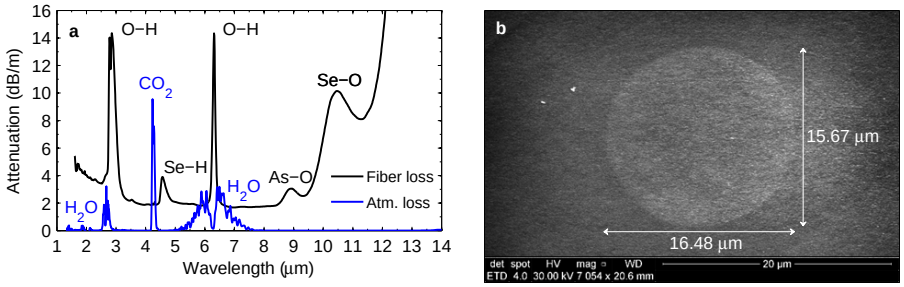

Figure 4.2.4: a) Loss measurements performed using a FTIR spectrometer, where the fiber measurement was performed using an intermediate fabrication step fiber with a core diameter of ~288 µm, and the atmospheric loss was measured in a 250 mm compartment. b) SEM image of the fiber core. The vertical and

horizontal scale axes of the core as shown are 15.67 μm and 16.48 μm, respectively.

4.2.2 EXPERIMENTAL RESULTS

The set-up used for generating and measuring the SC is shown in Figure 4.2.5. SCG was achieved by launching ~100 fs pulses with a repetition rate of 1 kHz into 85 mm of the chalcogenide SIF. The pump was generated from a tunable optical parametric amplifier (OPA) and non-collinear difference frequency generation (NDFG) module with tunable central wavelength from 2.5-11 μm. The OPA was pumped by a mJ pulse energy Ti:Sapphire laser system operating with ~60fs pulses and 1 kHz repetition rate. The pump pulses out of the NDFG were measured to be ~85 fs full width at half maximum (FWHM), and due to the relatively large pump bandwidth, the pulses were expected to be broadened to ~100 fs by the material dispersion from the focusing lens. No spectral broadening from the lens was observed. The 85 mm fiber was placed in a V-groove and mounted on a translation stage. The v-groove was only a few millimeters shorter than the fiber to avoid bending the fiber and to ensure maximum coupling efficiency and stability. The input beam was free-space coupled by a 5.95 mm focal length black-diamond (BD) aspheric lens with anti-reflection (AR) coating for the 2-6 μm spectral range, and the fiber output was collimated by a 1.873 mm focal length BD lens with AR coating for the 7-14 μm spectral range. The collimated beam was focused by a 100 mm focal length gold coated concave mirror onto the entrance slit of a grating monochromator. Long-pass filters were applied as order-sorting filters to eliminate higher-order effects. Detection was performed by a liquid nitrogen cooled HgCdTe (MCT) detector and boxcar integration system, and the short-wavelength edge was measured using an InGaAs array spectrometer. Proper coupling to the fiber core was verified by observing the collimated output beam profile using an electrically cooled micro-bolometer camera.

The broadest generated mid-IR SC spectra are shown in Figure 4.2.6(a) and Figure 4.2.7(a). The pump average power was increased without observing fiber damage up to ~350 μW and ~760 μW in the 4.5 μm and 6.3 μm pump cases, corresponding to a peak power of 3.29 MW and 7.15 MW, respectively. Since the actual coupled peak power is the most influential factor that governs spectral broadening in fibers it was important for the discussion of pulse propagation dynamics to estimate

the coupled peak power. The estimate was based on measuring the output power of the fiber using a pyroelectric detector. After proper coupling was verified using the micro-bolometer camera, the output lens was removed and the pyroelectric detector element placed in close proximity to the output facet. The fraction of coupled power was then calculated from the calculated Fresnel reflection from the fiber facets (~22 %) and the measured lens transmission (81.2 % at 4.5μm and 68.7 % at 6.3μm). In this calculation we are assuming that because of the short length the fiber attenuation loss can be neglected, and that additional scattering from the fiber facets due to surface roughness is also negligible. At low input power the coupled fraction of power was found to be ~60 %, and the maximum average output power ~150 μW. From this we estimated a maximum coupled peak power of 1.25 MW and 2.29 MW. As the pump power was increased, the spectrum quickly broadened and developed a distinct and stable peak at the long-wavelength edge, which extended as far as 11.7 μm and 13.3 μm, for the 4.5 μm and 6.3 μm pump cases, respectively. Despite the broad spectra with wavelengths comparable to the core diameter we observed nice core guidance in our fiber, with the energy remaining confined to the core at all power levels. This was further confirmed by placing a long-pass filter with a cut-on of 7.3μm in front of the camera, as can be seen in Figure 4.2.6(d) and Figure 4.2.7(d), which qualitatively shows the same good confinement to the core as was observed for the full spectrum in (c).

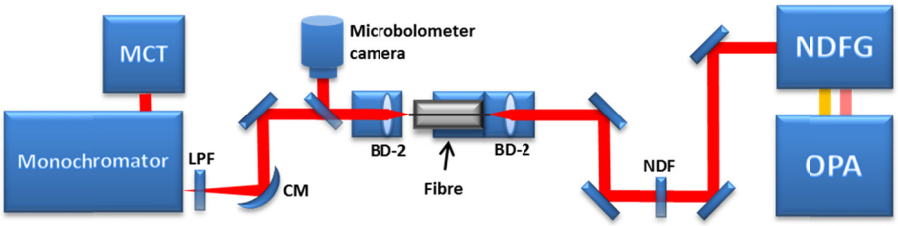

Figure 4.2.5: Experimental set-up for generating and measuring mid-IR SC. A non-collinear difference frequency generation (NDFG) unit pumped by an optical parametric amplifier (OPA) was used to produce the mid-IR pump. The output was free-space coupled into the fiber and subsequently collimated by aspheric lenses. A concave mirror was placed before the monochromator to prevent beam clipping and compensate for chromatic abberations. Proper coupling to the core was verified by near-field imaging using a micro-bolometer camera. BD-2: Black-diamond-2 aspheric lenses, NDF: Neutral density filter, CM: Concave mirror, LPF: Long pass filter, MCT: HgCdTe detector.

When pumping with 100 fs pulses in the normal dispersion regime at 4.5 µm the pulses, as is well known, initially undergo strong SPM, possibly leading to wave-breaking due to self-steepening and TOD, which causes a significant part of the light to be blue-shifted [125,126]. The red-shifting part will eventually cross the ZDW, at which point soliton dynamics, in particular Raman induced SSFS, will dominate further spectral broadening [42,126]. As expected we observed distinct SPM broadening close to the pump, and soliton dynamics when crossing the FM ZDW at 5.83 µm. This is clearly seen from the asymmetric evolution of the spectrum in Figure 4.2.6(b).

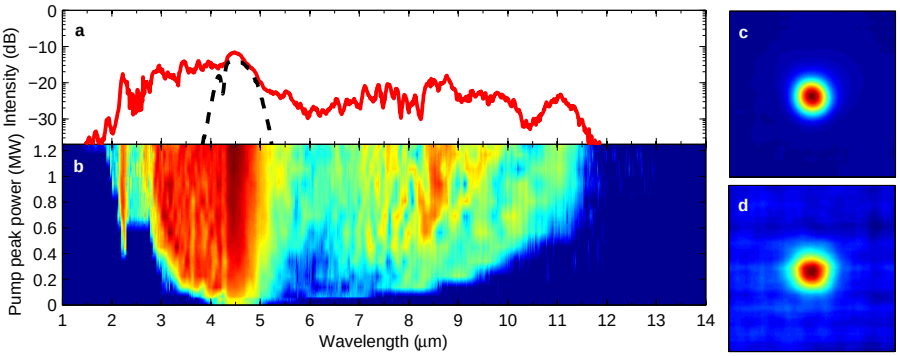

Figure 4.2.6: Experimental SCG results with the pump centered at 4.5 µm. (a) The input pump spectrum (dashed) and spectral profile at maximum pump power (solid), which shows a relatively flat SC (2.08-10.29 µm at -20 dB from the signal peak) with distinct soliton peaks above the ZDW ~5.83µm, especially at 11µm. (b) The spectral evolution with increasing pump peak power, which shows a gradual red-shift of distinct soliton peaks above the ZDW, and a combination of SPM and DWs below the pump wavelength. (c) The fiber output near-field beam profile corresponding to the spectrum in (a) for all wavelengths and (d), beam profile for wavelengths above 7.3 µm only, which show that the long wavelengths are still confined to the core.

The SPM edge was seemingly limited by the loss peak at ~2.9 µm, but at high power we observed the formation of a distinct spectral peak ~2.2 µm, which can only be explained as a parametric effect involving HOMs, which has previously been demonstrated numerically [88].

When pumping directly in the anomalous dispersion regime at 6.3 µm, just above the FM ZDW of 5.83 µm, the pump pulse is expected to transform into a higher-order soliton that rapidly breaks up into multiple fundamental solitons through soliton fission, and radiates DWs at a wavelength that is phase-matched to the solitons in the normal disper-

sion regime [45]. The red-shifting solitons will ultimately impose a trapping-potential on the DWs through GV-matching, and cause them to continuously blue-shift while being GV-matched [47]. However, this is only provided that a steady-state can be reached. When, for example, the dispersion or loss is locally changing, the trapping-potential is perturbed, causing the DWs to lose GV-matching and no longer be blue-shifted [47]. This means that the DWs will not only be influenced by the loss peak at ~2.9 μm, but also by the loss peaks experienced by the solitons, which represents an interesting physical interaction that complicates the dynamics of the spectral broadening.

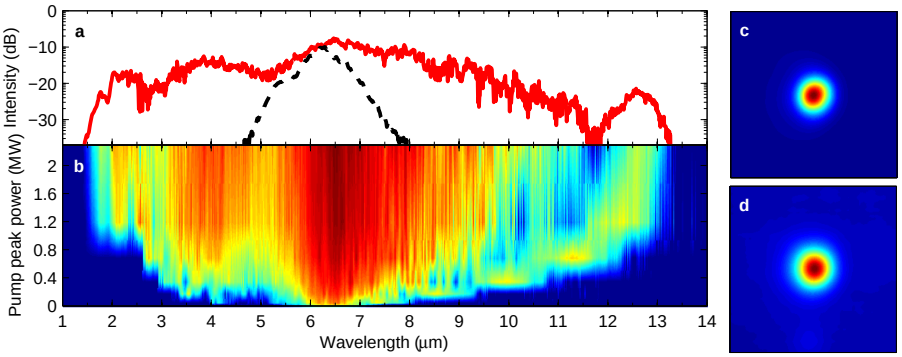

Figure 4.2.7: Experimental SCG results with the pump centered at 6.3 μm. (a) The input pump spectrum (dashed) and spectral profile at maximum pump power (solid), which shows a broad, flat SC (1.64-11.38 μm at -20 dB) followed by a strong spectral peak extending the spectrum all the way to 13.3μm. (b) The spectral evolution with increasing pump peak power shows the gradual red-shift of a distinct spectral peak at the long-wavelength edge and the corresponding formation and blue-shift of DWs. (c) The fiber output near-field beam profile corresponding to the spectrum in (a) for all wavelengths and (d), beam profile for wavelengths above 7.3 μm only, which show that the long wavelengths are still confined to the core.

Figure 4.2.7(b) shows the spectral evolution with increasing peak power. In the experiments we observed the formation of distinct DWs at ~3.5 μm and ~4 μm for low pump power, an increasing number of clear soliton peaks with increasing power, and the long-wavelength edge formed a large separate peak, which indicates a single high-power soliton. The short-wavelength edge of 1.4 μm extended beyond the limit imposed by GV-matching of the long-wavelength edge of the FM, as can be seen from the group-delay curve of Figure 4.2.1(b), which suggests that it is the result of intermodal parametric effects.

4.2.3 SUPERCONTINUUM SIMULATIONS

Pulse propagation and SCG was modelled using the GNLSE presented in Section 2.4, which is a standard framework used for this type of modelling where only a single spatially invariant mode and single polarization is considered. The GNLSE was rewritten into an interaction picture formulation and integrated using the 4th order Runge-Kutta integration method with adaptive step-size, based on the Local Error Method algorithm [127]. The spectral and temporal windows were composed of 2^{16} bins with the spectral window spanning from 1-30 μm yielding a temporal resolution dt=3.6 fs and spectral resolution df=4.2042 GHz. A series of peak powers were chosen in the simulations in order to best match the simulated SC spectra to the short and long wavelength edges of the experimental spectra. The linear propagation operator in the simulations was based on the calculated fiber dispersion using COMSOL Multiphysics together with the measured fiber loss. The loss was only measured out to 12.5 μm, where it was about 25 dB/m. In the simulations we artificially extrapolated the loss to 1000 dB/m above 12.5 μm to avoid overloading the spectral window. The nonlinear operator was given by the Kerr coefficient from slusher *et al*. [65] and Raman gain from Ung and Skorobogatiy [128].

A comparison between experiment and simulation in the 4.5 μm pump case is shown in Figure 4.2.8. The experimentally observed dynamics and qualitative dependence on the pump peak power was remarkably well reproduced by modelling of the FM alone. This is most likely because the dynamics were initially governed by SPM. Even after the SPM generated light crosses the ZDW at ~5.83 μm, the simulations produce the same heavily modulated spectrum consistent with soliton dynamics. The peak power used in the simulations was reduced by a factor of ~5 in order to reproduce the same features as seen in the experiment. This factor was justified by a combination of measurement uncertainty, a factor of two power loss due to coupling to the orthogonal polarization, and further power loss from coupling to HOMs [87].

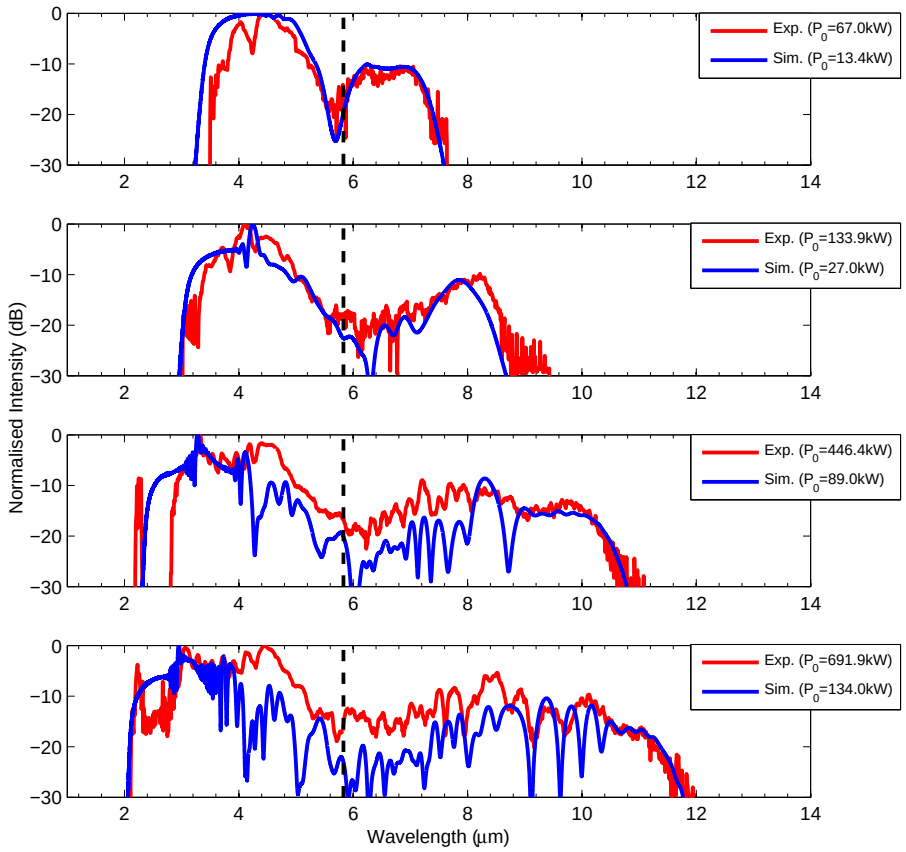

Figure 4.2.8: Comparison between experimental (red solid) and simulated (blue solid) SCG in the 4.5μm pump case for varying input peak power, together with the ZDW of the fibre (black dashed).

The 6.3 μm pump simulations were also able to reproduce some of the same features present in the experimental spectra at low input power, such as the formation of DWs in the normal dispersion regime, as can be seen in Figure 4.2.9. At 6.3 μm our fiber modelling for the FM showed that the nonlinear parameter was γ=0.04 $W^{-1}m^{-1}$ ($n_2 = 4.893 \times 10^{18}\ m^2W^{-1}$) [65] and the dispersion was D=3.24 ps $nm^{-1}km^{-1}$, which for a 100 fs pulse with estimated coupled peak power of 2.29 MW results in a soliton number of N=118 and fission length of just 1.27 mm. A soliton number larger than 10 would suggest that the SCG is noisy with large shot-to-shot variations in the output spectrum due to incoherent MI amplification of vacuum noise [42]. However, this calculation neglects HOMs and coupling to the orthogonal polarization, which may effectively reduce the soliton number in the FM. In fact, we observed a

relatively high degree of spectral stability of the SC. This can be seen from Figure 4.2.10, comparing the measured spectra with 1 shot per 10 nm to 100 shots averaging per 10 nm sampling. Furthermore, the simulated input peak power was reduced by a factor of ~17.5 in order to obtain qualitative correlation with the experimental data, and the high factor may be due to the fact that in our experiment a large part of the light is present around the pump wavelength, where the simulations predict that a large part of the light will be shifted away. This discrepancy is attributed partly to the excitation of HOMs, which tend to cause little broadening and thus increase the signal around the pump as demonstrated by Poletti et al. [88]. Only experimental data for broadening below 12.5 μm was compared with simulations because of the imposed artificial loss edge.

4.2.4 Conclusion

These results were the first to demonstration a broadband fiber-based SC light source covering both of the transparent atmospheric windows at 3-5 μm and 8-13 μm [129], as well as an important part of the chemical functional group and fingerprint regions from 1.4-13.3 μm. The SIF design allowed for high power handling capabilities, with potential for flexible output beam delivery and simplified system integration, all of which will be essential in realizing efficient mid-IR analytical tools. The results represented an important step forward in overcoming the limitations of current mid-IR light sources, paving the way for many later demonstrations, including the recent demonstration of SCG in a $As_2Se_3/AsSe_2$ SIF reaching 15.1 μm using a similar pumping scheme, but pumping at 9.8 μm [130]. However, these demonstrations only serve as proof of principle, since the sources are impractical and the average output power low due to the advanced kHz pump system needed. The ideal pump source would be a mode-locked rare-earth-doped chalcogenide fiber laser that could be spliced to the nonlinear fiber for improved coupling efficiency. However, such sources are not available, so instead other tricks must be played in order to scale up the average power. One way of scaling up the average power is by using a high repetition rate femtosecond OPA source with a lower peak power. Results with this pumping scheme is presented in the following section.

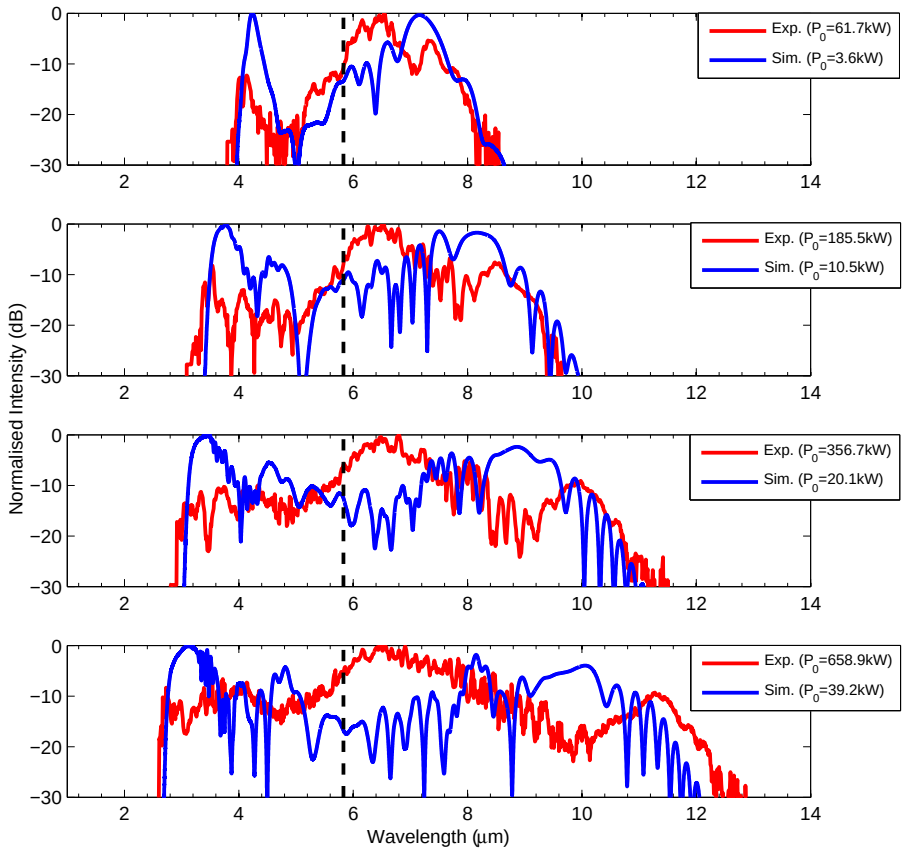

Figure 4.2.9: Comparison between experimental and simulated SCG for the 6.3μm pump case with varying input peak power, together with the ZDW of the fiber (black dashed line).

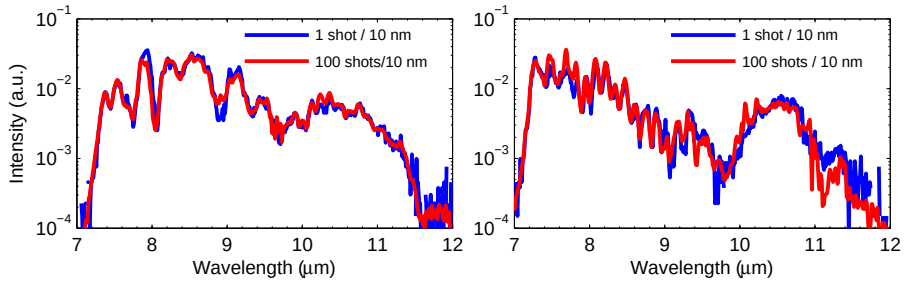

Figure 4.2.10: Shot-to-shot stability analysis. Comparison between single-shot per 10nm spectrum and averaging over 100 pulses per 10nm in the 4.5μm (left) and 6.3μm (right) pump cases, which shows that the spectrum is quite stable considering the free-space coupled nature of the set-up.

4.3 Kilowatt-Megahertz pumping scheme

Following the demonstration of SCG up to 11.7 μm from pumping at 4.5 μm we decided to investigate the possibility of scaling up the SC output power by employing a MHz optical parametric generation (OPG) source operating at a central wavelength of 4-4.5 μm. The source was built after the design presented in ref. [131].

4.3.1 Optical Parametric Generation

The OPG source consisted of a low-power tunable continuous wave (CW) seed that was mixed with 250 fs pulses from a 1040 nm mode-locked pump laser in a periodically poled lithium niobate (PPLN) non-linear crystal. The crystal is periodically poled to obtain quasi phase matching at a specific wavelength given by the poling period. This enables degenerate parametric generation of Stokes and anti-Stokes waves, as explained in the theory section 2.3.3. Furthermore, the crystal has a fan-out design with a varying poling period over the cross-section of the crystal, allowing for the phase matching wavelength to be tuned by translating the crystal. The material dispersion (phase matching condition) was tuned thermally by keeping the crystal in an oven at 150° C. This configuration enabled tuning of the idler beam from ~3.8-4.5 μm, with average power ~260-120 mW, respectively. Figure 4.3.1 show the beam profile and spectrum at different tuning wavelengths. The larger beam at 4.4 μm is due to the different *k*-vector in the phase-matching.

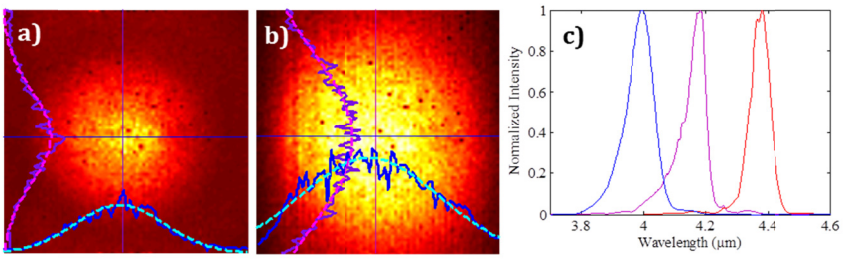

Figure 4.3.1: OPG beam profiles of at (a) 4 μm and (b) 4.4 μm. The solid curves show the intensity of the beam cross-sections measured with an IR camera, and the dashed line is a Gaussian fit. (c) Spectrum of the generated mid-IR pump at three select wavelengths.

Unfortunately, it was not possible to perform temporal characterization of the generated idler pulses with our existing autocorrelator at these

peak power levels, so the pulse duration was instead inferred from the spectrum. At 3.992 µm central wavelength a Gaussian fit of the spectrum yielded a full width at half maximum (FWHM) of 93.7 nm, which for a time-bandwidth limited Gaussian pulse corresponds to 249.6 fs, but at 4.391 µm the bandwidth was reduced to around 70 nm, which corresponds to 418.7 fs. The exact shape and FWHM of the pump varied with crystal tuning and pump power, so it is possible that it may be significantly chirped. A similar source built at Australian National University (ANU) was numerically estimated to yield around 320 fs pulses at 4 µm [131] and 330 fs at 4.485 µm [132] when pumped with a 500 fs laser at 1041 nm, but the bandwidth or time-bandwidth product was not provided for comparison.

4.3.2 Step-Index Fiber

For the kW-MHz pump experiment a longer fiber segment of 25 cm with a smaller core diameter of 11 µm was used to compensate the lower pump peak power. The smaller core also resulted in a slightly shorter calculated ZDW of 5.32 µm. The pump was tuned to 4.4 µm, pumping in the normal dispersion regime with a maximum of around 153 mW before the in-coupling lens. The result is plotted in Figure 4.3.2 in terms of power spectral density (PSD) in µW/nm. The result indicates that about two to three orders of magnitude higher power spectral density was achieved in the 3-8 µm region, with a total output power of 28.5 mW (5.5 mW >4.5 µm) after collimation. In comparison the 0.15 mW from MW-kHz result yields a PSD of around 10^{-2} µW/nm in this region. From the pump/output power and measured lens transmission of 92.3 % we estimated around 36.5 % transmission, which corresponds to a coupled peak power of 4.1 kW assuming 400 fs pulses (6.5 kW for 250 fs pulses). At 4.4 µm $A_{\text{eff}} = 28.81\ \mu\text{m}^2$ resulting in $\gamma = 0.27\ \text{W}^{-1}\text{m}^{-1}$, and hence the nonlinear length $L_{NL} = 0.91$ mm is still very short.

Besides heavy coupling/Fresnel losses, evident from the low transmitted output power, the primary limitation was again the long ZDW compared to the pump wavelength, which resulted in a significant amount of the pump beam exhibiting only moderate broadening due to SPM. This is also seen from the spectral evolution in the bottom window

of Figure 4.3.2, which shows similar qualitative broadening features with increased pump power as in the 4.5 µm MW-kHz pump scheme.

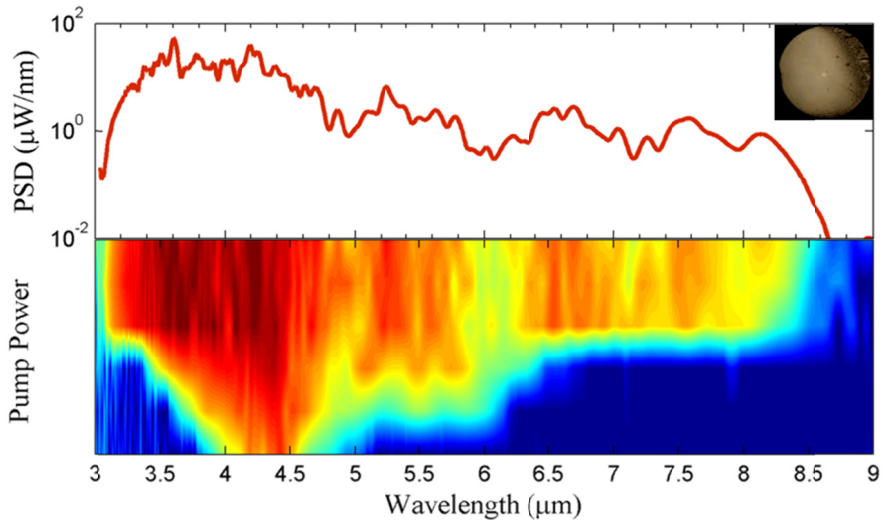

Figure 4.3.2: (Top) PSD of the AsSe SIF SC spectrum at a maximum pump power of 141 mW, resulting in 28.5 mW total average output power, and 5.5 mW > 4.5 µm. Inset shows the fiber end-facet cross section. (Bottom) Spectral evolution with increased pump power, revealing similar broadening properties as in the MW-kHz pump case.

Reducing the core size further would not necessarily improve the results, since numerical modelling had revealed that this would only slightly shift the ZDW and more importantly would also introduce a second ZDW at longer wavelengths, eventually leading to all-normal dispersion [133]. To reduce the ZDW while maintaining a broad window of anomalous dispersion the NA of the fiber must be raised by increasing the index contrast of the core/cladding glass, such as in ref. [67]. This would enable a shorter ZDW and broader region of anomalous dispersion for smaller core diameters, as shown in Figure 4.3.3. For example, an NA of ~1.6 would allow for anomalous dispersion from around 3.2-9.5 µm in a 5 µm core fiber, and around 4 µm to above 10 µm in a 7 µm diameter fiber. Such high-NA fibers have been fabricated at Nottingham and are currently under investigation at DTU.

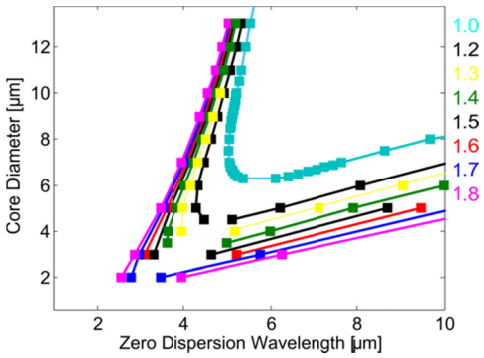

Figure 4.3.3: Calculated ZDW(s) as a function of core diameter for different fixed NA based on As_2Se_3 core glass. Increasing the NA shifts the curve towards the bottom left corner, enabling shorter ZDW and a broader region of anomalous dispersion.

4.3.3 Suspended-Core Fiber

(Based on journal paper [III], Ref. [82]*)*

Another fiber geometry that allows for a very short ZDW is the three-hole suspended core fiber (SCF) structure shown in the inset of Figure 4.3.4. The $As_{38}Se_{62}$ SCF had a core diameter of 4.5 µm and was fabricated by Perfos. This fiber had a ZDW around 3.5 µm, which enabled pumping far into the anomalous dispersion regime. The fiber loss presented in Figure 4.3.4(a) was estimated from cut-back measurements between 1.4-8.5 µm of a six-hole $As_{38}Se_{62}$ 'wagon-wheel' fiber with a core diameter of 20 µm (black curve). Troles et al. reported that the 4.5 µm fiber had a 0.4 dB higher loss than the 20 µm fiber at 1.55 µm [134], so this loss was added uniformly to the 20 µm data and extrapolated at the edges to 100 dB/m (red curve). Absorption peaks due to O-H at 2.9 µm and 6.3 µm are visible from the spectrum, along with a small Se-H absorption at 4.3 µm. The dispersion was calculated based on the fiber geometry and As_2Se_3 material refractive index measurements from Amorphous Materials Inc., which were in good agreement with the refractive index of $As_{38}Se_{62}$ [79]. Because of the geometry, the fiber is slightly birefringent with a birefringence of 4.2×10^{-4} at 3.5 µm, and so both the dispersion of the slow and fast axis were calculated in COMSOL Multiphysics as shown in Figure 4.3.4(b). There was no observable difference due to the fiber orientation in the experiments, and therefore no

special care was taken to orient the fiber to account for the birefringence.

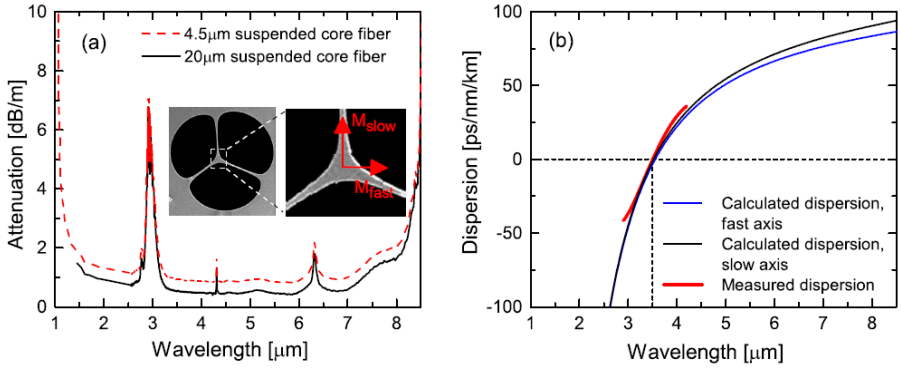

Figure 4.3.4: (a) Measured fiber loss of a 6-hole 'wagon-wheel' fiber with a core diameter of a 20 μm (black solid) from which the estimated fiber loss of the SCF with a core diameter of 4.5 μm was calculated (red dashed). Inset: SEM image of the 4.5 m SCF and a zoom-in on the core indication the fast and slow polarization axis. (b) Measured (red) and calculated dispersion for the slow (black) and fast (blue) axis. (Source: [82]).

The SC experiments were carried out at ANU by Ph.D. student Yi Yu using an OPG setup similar to the one at DTU described in section 4.3.1, with the main difference being that the ANU mid-IR pump had a pulse duration of 320 fs, and the beam was chopped before in-coupling. The pump was coupled to an 18 cm fiber segment using an NA = 0.85 BD-2 lens. The output was collimated using a similar lens when evaluating the insertion loss, and a reflective objective lens when measuring the spectrum. Spectral acquisition was performed using a monochromator equipped with a PbSe and MCT detector connected to a lock-in amplifier for the 1.5-4.0 μm and 4.0-8.5 μm ranges, respectively. Order sorting filters were used to prevent measurement of higher order diffraction. At wavelengths >4.0 μm the data was corrected for the MCT detector responsivity, which was provided by the manufacturer. The total insertion loss of the fiber plus the coupling lenses was measured to be 7.5 dB. Pulse propagation and SCG was simulated using the same method as described in section 4.2.3.

Figure 4.3.5 shows a comparison between experimental and numerical results when tuning the pump wavelength from 3.5 μm to 4.7 μm. The solitonic long wavelength edge was gradually red-shifted to longer wavelengths in the simulated spectra, and accordingly the short

wave-length edge was blue-shifted, consistent with group-velocity matched dispersive waves. However, the same clear trend was not observed in the experiments. In the experiments the spectrum was increasingly broadened when the pump was shifted between 3.5 μm and 3.9 μm, but for longer pump wavelengths the broadening was halted as the pump was tuned further up to 4.7 μm.

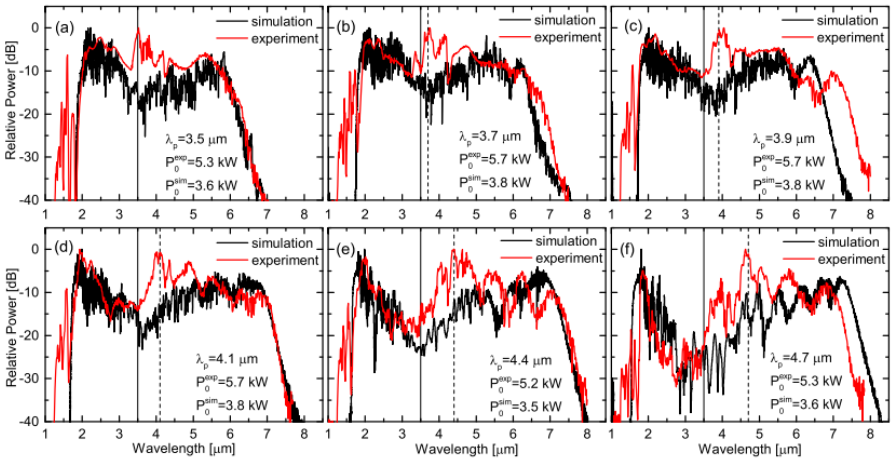

Figure 4.3.5: Comparison between simulations (black) and experiments (red) at six different pump wavelengths (vertical dotted line). The ZDW is indicated as the vertical solid line. (Source: [82]).

The absence of a long wavelength extension when pumping at wavelengths longer than 3.9 μm was initially attributed to inconsistent coupling in the experiment, resulting in variable excitation of HOMs, but another possible explanation could be that the small core diameter could impose a fundamental limitation to the guiding properties >7.5 μm. As explained by Chemnitz and Schmidt, when the wavelength of light becomes increasingly larger than the core diameter the mode may develop a double-lobe pattern that extends beyond the geometrical core into the air cladding [135]. The cladding field contribution becomes greater with wavelength, and so the long-wavelength part of the spectrum experiences a reduced optical nonlinearity and increased loss.

Nevertheless the broadest experimental SC spectrum spanning from 1.7 to 7.5 μm was obtained when pumping at 4.4 μm, and the average output power was 15.6 mW with a BD-2 lens at the fiber output and the chopper turned off. Based on the measured spectrum and total average output power, the average power > 5.0 μm was estimated to be 4.7

mW. The spectrum is plotted in terms of PSD in Figure 4.3.6, which shows that the shorter ZDW did not improve the bandwidth or the PSD, but it did however improve the long-wavelength efficiency significantly. When pumping at 4.7 µm the total average output power was increased to 16.0 mW and 7.5 mW >5.0 µm, although parts of the supercontinuum spectrum from 2.0 to 3.5 µm dropped below the -20 dB mark.

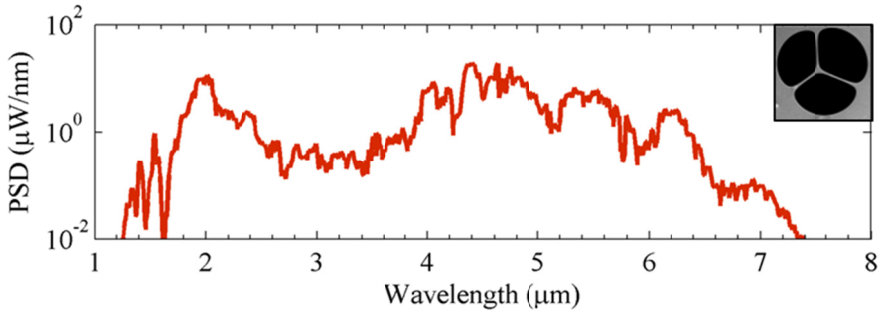

Figure 4.3.6: PSD of the AsSe SCF spectrum at a maximum pump power of 44 mW at 4.4 µm, resulting in 15.6 mW total average output power, and 4.7 mW > 5 µm. Inset shows the fiber end-facet cross section.

The experiments succeeded in demonstrating SCG spanning almost the entire transparent region of the fiber, but were limited in terms of output power due to the lower damage threshold of the suspended core. When comparing the PSD plot in Figure 4.3.6 with that of the SIF in Figure 4.3.2 it is clear that there was no benefit to the long-wavelength generation from using the SCF design.

4.3.4 Photonic Crystal Fiber

We also investigated pumping a commercial single-material $Ge_{10}As_{22}Se_{68}$ PCF from Perfos with a nominal 13 µm core diameter, pitch of Λ=8.5 µm, and $d/\Lambda = 0.44$, making it endlessly single-moded. This GeAsSe PCF was chosen over a similar AsSe PCF because it had a relatively short ZDW measured at around 4.6 µm, compared to around 5.1 µm in AsSe [136]. The shorter ZDW should improve the long-wavelength generation efficiency compared to the SIF, and the large core diameter and PCF design allows for better coupling efficiency and power handling compared to the SCF. The loss and dispersion of this fiber is shown in Figure 4.3.7. The measured dispersion of the fiber was

found to be in good agreement with the modelled dispersion, which is based on refractive index data for the slightly different $Ge_{10}As_{23.4}Se_{66.6}$ composition. A nonlinear refractive index of $n_2 = 8.8 \times 10^{-18}$ m^2W^{-1} at 1.55 µm was provided by the manufacturer, which is comparable to AsSe-type fibers.

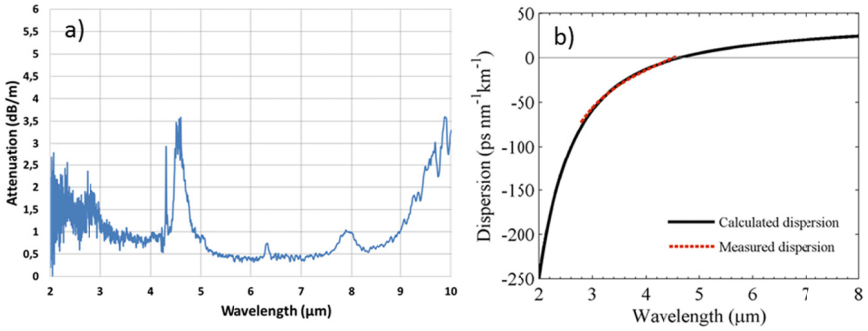

Figure 4.3.7: (a) Loss of the 13 µm core $Ge_{10}As_{22}Se_{68}$ PCF provided by Selenoptics. (b) Comparison between the measured (red dashed) and calculated (black solid) dispersion curves, showing good agreement between the two and a ZDW near 4.6 µm.

Figure 4.3.8 shows the result of pumping 25 cm of fiber at 4.4 µm with a maximum of 127 mW pump power (maximum at the time of the experiment), which yielded a total output power of 49.5 mW and 10.5 mW above 4.5 µm, which is almost twice as much compared to the AsSe SIF, albeit at the expense of a shorter long-wavelength edge of around 7.5 µm. The pump wavelength was just short of the Se-H absorption at 4.5 µm, while avoiding the CO_2 absorption at 4.25 µm. The bottom window of Figure 4.3.8 shows yet again the clear sign of SPM broadening below the pump, which constitutes an effective loss to the long-wavelength generation. Changing the pump wavelength to 4 µm for increased pump power was therefore found not to improve the long-wavelength generation efficiency, and using a longer fiber was also had no major impact on spectral broadening or long-wavelength output power. The immediate conclusion must be that the SCG was limited mainly by the properties of the fiber and the available pump power. However, unlike the SIF reducing the core diameter of the GeAsSe PCF should according to our calculations significantly shift the ZDW towards shorter wavelengths, while maintaining anomalous dispersion beyond 10 µm. Although, while pumping such a small-core fiber increases the efficiency and nonlinearity it also reduces coupling efficiency. For this

reason an entirely different approach was taken - we decided to investigate tapered PCFs as a potential path to obtaining increased broadening, while maintaining high average power. The following section presents our work with increasing the spectral broadening through fiber tapering, while maintaining a high average output power.

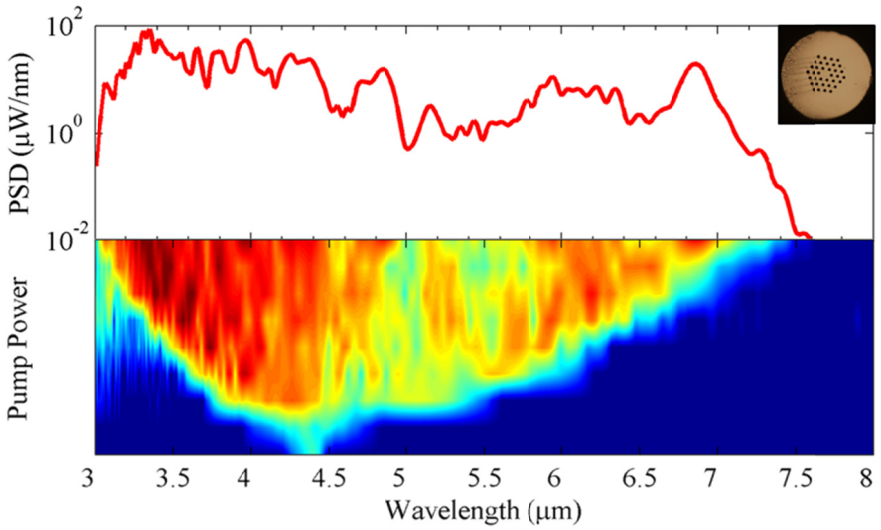

Figure 4.3.8: (Top) PSD of the ~13 μm GeAsSe PCF SC spectrum at a maximum pump power of 127 mW, resulting in 49.5 mW total average output power, and 10.5 mW > 4.5 μm. Inset shows the fiber end-facet cross section. (Bottom) Spectral evolution with increased pump power, revealing distinct SPM broadening below the pump, and soliton dynamics at longer wavelengths.

4.4 SUPERCONTINUUM GENERATION IN TAPERED FIBERS

4.4.1 INTRODUCTION

In order to improve the long-wavelength generation efficiency a symmetrically tapered $Ge_{10}As_{22}Se_{68}$ PCF with 12.4/119 μm initial core/cladding diameter was tapered down to around 7.2 μm by the company Selenoptics, as shown in the schematic of Figure 4.4.1(a). This glass composition was chosen over the more nonlinear $As_{38}Se_{62}$ due to its resistance to crystallization [68]. We verified the initial core diameter by SEM imaging (Figure 4.4.1(c)), and the core diameter at the taper

waist was determined by Selenoptics to be around 7.2 µm by measuring the outer diameter of the fiber at the waist with ±2.5 µm accuracy.

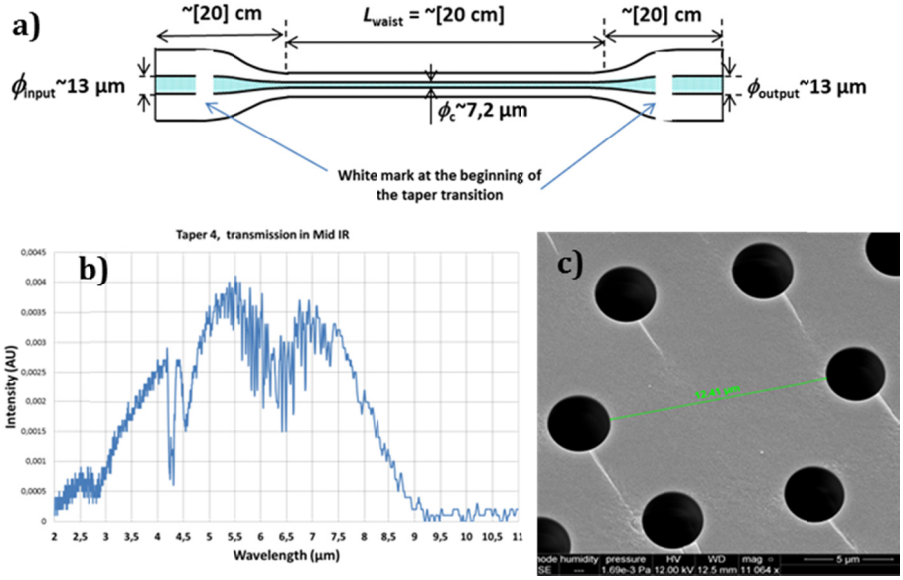

Figure 4.4.1: (a) Taper schematic showing the approximate scales of the fiber. (b) Taper transmission spectrum measured by Selenoptics, showing heavy influence from O-H at 5.5-7.5 µm. (c) SEM image of the input facet.

Verifying the tapered core diameter by SEM imaging would require breaking the taper at the waist, so instead we measured a second taper from the same fiber batch with an estimated diameter of 7.6 µm. The second taper was found to have a waist diameter of ~7.8 µm, as shown in Figure 4.4.2, so we estimated the accuracy of the core diameter in the waist to be ±0.25 µm, one tenth of the outer diameter accuracy, since the core diameter was about one tenth of the outer diameter. The relative transmission of the taper was characterized by Selenoptics, and from the transmission curve of Figure 4.4.1(b) several features are visible. Firstly, while these fibers should have less than 4 dB/m loss from 1.4-10 µm [68,137] the fiber transmits only between 2-9 µm, most likely due to a combination of long fiber length and increased confinement and scattering losses at the taper waist. Secondly, there are several absorption lines present due Se-H at 4.6 µm, O-H around 2.8 µm and from 5-7.5 µm, and CO_2 at 4.25 µm. Especially the O-H absorption due to infiltration of atmospheric air into the capillaries of the fiber results in significant

losses, which have been found to accumulate over time [137]. This optical aging results in strong absorption peaks at 2.8 µm 6.3 µm [137].

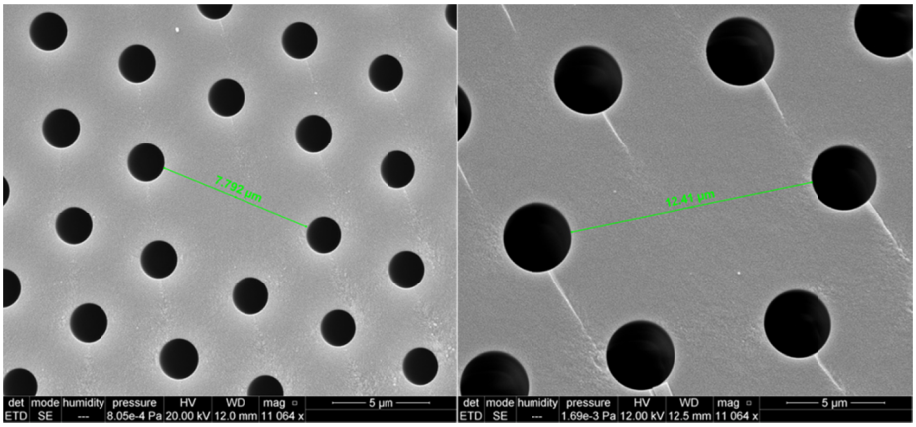

Figure 4.4.2: SEM images of the fiber end facet at the taper waist (left) and input of the fiber (right). The images were taken for taper made from the same batch as the one in the SC experiment, but with a slightly larger waist diameter of around 7.8 µm compared to 7.2 µm in the experiment.

The dispersion was calculated based on Sellmeier coefficients from $Ge_{10}As_{23.4}Se_{66.6}$ glass [34], which is expected to be very similar. The calculated dispersion curves for various core diameters is shown in Figure 4.4.3. The initial fiber is expected to have a ZDW around 4.6 µm and in the waist a 7.2 µm core diameter should shift the ZDW down to around 3.8 µm. Such a short ZDW would enable the use of the higher available pumping power at 4 µm, due to the increased efficiency of the OPG, which may be beneficial for increasing the maximum output power.

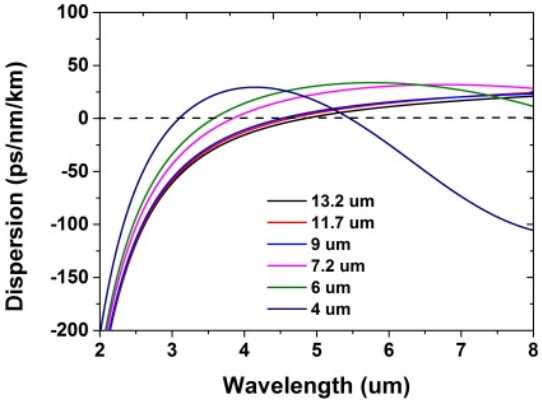

Figure 4.4.3: Calculated dispersion for the GeAsSe PCF with various core diameters. The dispersion was calculated based on Sellmeier coefficients from $Ge_{10}As_{23.4}Se_{66.6}$ glass.

4.4.2 SUPERCONTINUUM EXPERIMENTS

To test the effect of reducing the ZDW through tapering we compared the results with pumping at 4.02 μm and 4.38 μm with 207 mW and 146 mW pump power, respectively. The results, shown in Figure 4.4.4, show a strong increase in spectral broadening on the short wavelength side in both cases, but no apparent long-wavelength broadening. The long-wavelength conversion efficiency was evaluated by measuring the power after a 4.5 μm long-pass filter. Using the 4.02 μm pump only 12.4 mW of the total 42.0 mW extended above 4.5 μm (29.5 %), compared to 14.3 mW out of 32.5 mW (44 %).

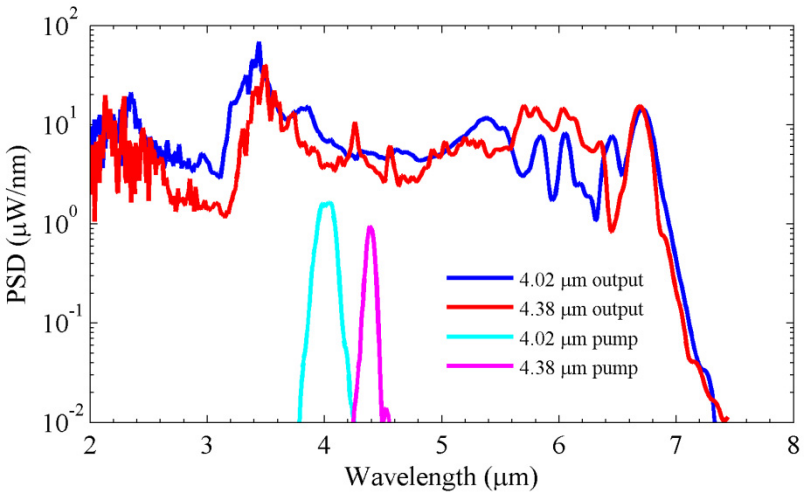

Figure 4.4.4: Comparison between pumping the tapered PCF at 4.02 μm and 4.38 μm. Pump spectra are shown for reference. The oscillations in the short-wavelength end of the spectra is due to applying wavelength calibration to the FTIR spectrometer.

However, while the long-wavelength power and efficiency was improved compared to the initial 10.5 mW and 21 % for the untapered fiber, the long-wavelength edge was not extended. One explanation could be that because of the long untapered part before the taper transition (10-15 cm), the spectrum will already have broadened fully before the taper waist, and so a lot of pump light will still exhibit moderate broadening in the normal dispersion regime. To test this we cut back the fiber on the input end to 4 cm before the taper transition and repeated the experiment. Figure 4.4.5 show the clear result of the cut back, resulting in extension of the spectrum up to 8.6 μm and 39.5 mW output power when pumping at 4.4 μm. When pumping at 4.0 μm a higher output power of 54.8 mW could be achieved, but at the cost of reducing the long-wavelength edge to 8 μm. For the two pump cases the power after the long-pass filter was 21.5 mW and 18.7 mW for the 4.0 μm and 4.4 μm pump cases resulting in an efficiency of 39 % and 47 %, respectively. This is a significant improvement compared to the initial 21 % for the untapered fiber. Note that Figure 4.4.5 and the remaining figures of this section was measured with a monochromator and MCT detection system, which had better sensitivity in the short-wavelength range.

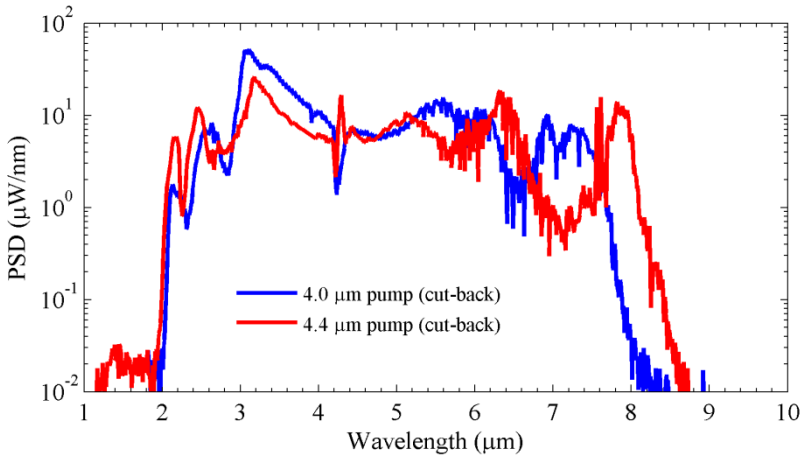

Figure 4.4.5: Results of taper cut-back when pumping at 4 μm and 4.4 μm measured using a monochromator and MCT detector. In the 4 μm pump case a total of 54.8 mW was obtained (21.5mW >4.5 μm), and 39.5 mW (18.7mW >4.5 μm) in the 4.4 μm pump case.

In an attempt to benefit even further from the increased power when pumping at 4 μm, we decided to try another taper with both a smaller initial core diameter of around 11.5 μm and smaller waist diameter of around 6 μm, which should shift down the ZDW to around 3.6 μm according to in Figure 4.4.3. The fiber was cleaved 5 cm from the input taper transition, and was in total around 30.8 cm long. The fiber had a measured average hole diameter of 4.42 μm, and pitch of 7.66 μm, resulting in a $d/\Lambda = 0.446$. This configuration resulted in extending the spectrum from 8 μm to almost 9 μm with similar output power levels of maximum 44.5 mW and 21 mW above 4.5 μm observed. **Figure 4.4.6** show the spectral evolution of an experiment that resulted in 41.5 mW output power and 19.3 mW above 4.5 μm. It is evident from the spectrum that the ~10-13 mW reduced total output power compared to the larger core taper was mainly taken from the peak at 3-4 μm, but the fact that the absolute power above 4.5 μm was not improved suggest that it may be beneficial to maintain a larger initial core diameter to improve coupling efficiency.

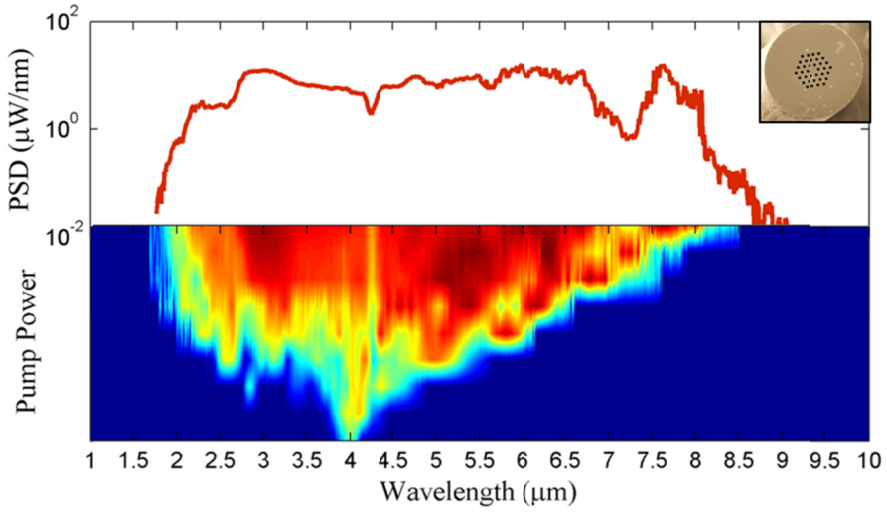

Figure 4.4.6: (Top) PSD of the tapered 11.5 µm GeAsSe PCF SC spectrum at a maximum pump power of 213 mW, resulting in 41.5 mW output power and 19.3 mW above 4.5 µm. Inset shows the fiber end-facet cross section. (Bottom) Spectral evolution with increased pump power, revealing distinct DW generation on the short-wavelength side, and SSFS on the long-wavelength side.

To test whether our results represented the full potential of the taper we performed a measurement using the MW-kHz source and pumping far in the anomalous dispersion regime at 4.9 µm. In the same fiber a spectrum extending up to 11 µm was obtained, as seen in Figure 4.4.7, which shows that the long-wavelength edge is now limited mainly by the available peak power of the pump source. Future improvements should focus on improving the coupling efficiency, and optimize the length of the taper for maximum efficiency.

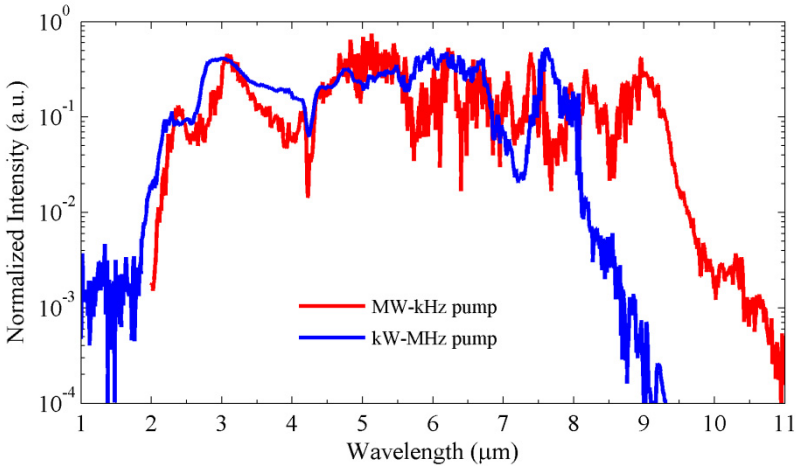

Figure 4.4.7: Comparison between the normalized output spectrum of the tapered 11.5 μm GeAsSe fiber when pumping with the MW-kHz and kW-MHz configuration. The result show that the fiber can indeed transmit to 11 μm if sufficient peak power can be supplied.

4.5 Cascaded Supercontinuum Generation

4.5.1 Introduction

Cascaded SCG describes the technique of generating a SC in a consecutive cascade of different fibers in order to benefit from their respective properties at each stage in the continuum generation process. The motivation for this scheme is avoid costly and impractical mid-IR pump sources, and eliminate the use of free-space optics to obtain a practical and robust all-fiber configuration. As mentioned in the introduction to the chapter, new mid-IR glasses are needed to extend the spectrum beyond the silica transmission limit of 2.5 μm. Currently, the most mature mid-IR fiber SC technology is based on fluoride glasses, such as ZrF_4-BaF_2-LaF_3-AlF_3-NaF (ZBLAN), owing to their high-power capabilities and excellent transmission from the UV to about 4.5 μm [59,138]. Due to these unique properties commercial ZBLAN SC sources are now emerging [139–141], and in this regard cascaded SCG has been one of the key enabling technologies for efficient SCG, because it has enabled the use of matured technologies such as semiconductor laser diodes, silica fibers, and fiber amplifiers [63,139,141]. However, the use of ZBLAN fibers limits the spectrum to around 4.5 μm due to strong multiphonon ab-

sorption in the host material [59], and thus further broadening requires mid-IR transparent glasses, such as chalcogenides. Extending the cascading scheme to chalcogenide fibers presents an attractive alternative to direct pumping schemes with the potential for all-fiber integration enabled by advances in fusion splice technology [142–144].

4.5.2 CASCADED 2 µM LASER PUMP SCHEME

(Based on journal paper [V], ref. [119])

The ZBLAN-chalcogenide cascading scheme was first studied numerically back in 2014, which demonstrated the possibility of generating a spectrum from 0.9-9.0 µm by pumping a 5 µm diameter As_2Se_3 SCF with a ZBLAN SC generated from a thulium-doped fiber laser, as shown in Figure 4.5.1 [119]. In this scheme a commercially feasible mode-locked thulium-doped fiber laser emitting 3.5 ps Gaussian pulses with a 30 MHz repetition rate at 2 µm central wavelength with a maximum peak power of 20 kW was simulated as the pump source. The modelled ZBLAN fiber was based on the material dispersion from Gan [100] and measured fiber loss provided by FiberLabs Inc., Japan. The SIF had a core diameter of 5.7 µm and NA of 0.30, which yielded a very low, anomalous dispersion of the FM with a ZDW of 1.59 µm. The dispersion and loss of the fiber is shown in Figure 4.5.2. When pumping the fiber far from the ZDW with low anomalous dispersion the generated solitons rapidly shifted to longer wavelengths due to enhanced SSFS, resulting in very efficient mid-IR SC [94], as seen in Figure 4.5.3.

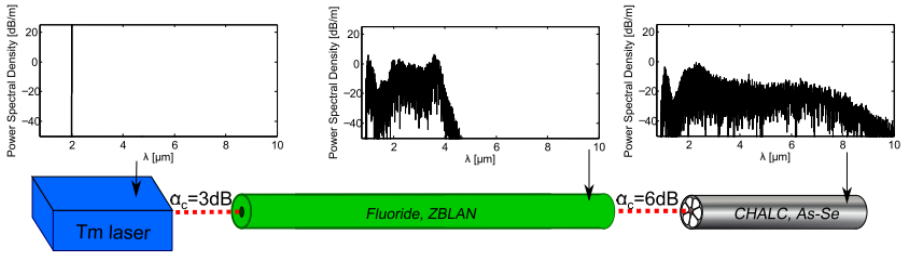

Figure 4.5.1: Pumping scheme for cascaded SCG based on a Tm fiber laser, ZBLAN fiber, and AsSe SCF. Coupling losses used in the simulations are indicated at the input interfaces, and the output spectra from the three stages in the cascade are shown in the top. Figure from [119].

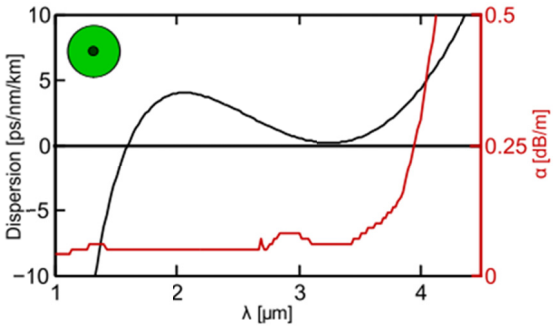

Figure 4.5.2: ZBLAN fiber properties. The dispersion (black curve) was calculated based on the 5.7 μm SIF geometry, NA=0.3, and core material dispersion from Gan [100]. The fiber loss (red curve) was supplied by FiberLabs Inc.

For the SC broadening to successfully continue in the AsSe fiber requires both a low coupling and propagation loss, so that the broadening processes are not inhibited, and anomalous dispersion across most of the transmission window so that the solitons from the ZBLAN SC are allowed to further broaden the spectrum. A coupling loss of 3 dB and 6 dB was assumed from coupling to the ZBLAN and AsSe fibers, respectively. Transferring solitons between fibers with a substantial difference in nonlinearity further allows for dramatic broadening, as was detailed by Agger et al., where the dramatic difference in nonlinearity was shown to result in extreme soliton fission [145]. For the ZBLAN fiber $n_{2,ZBLAN} = 2.55 \times 10^{-20}\ \mathrm{m^2W^{-1}}$ was used [94], compared to $n_{2,AsSe} = 2.4 \times 10^{-17}\ \mathrm{m^2\ W^{-1}}$ [128], which is almost three orders of magnitude higher. The AsSe fiber loss and dispersion from Figure 4.3.4 was used for the simulations. Figure 4.5.3(a) and (b) display spectrogram plots of the spectral-temporal composition of the output from ten meters of ZBLAN and ten centimeters of AsSe fibers, respectively.

The ZBLAN spectrogram show the clear signature of solitons from the temporally narrow and spectrally broad lines in the -2 to 28 ps temporal window covering from 1.8-4.5 μm. The DWs below the ZDW are seen to be GV-matched to the solitons, as illustrated by the solid black line of the total group-delay $\beta_1 L$ [42]. Figure 4.5.3(e) show the development of the long-wavelength edge (-30 dB level) along with the output power in the 3-5 μm band. In less than two meters the spectrum reaches the multiphonon edge, but the power generated in the 3-5 μm band continues to increase until around ten meters, thus a length of ten meters was chosen as the optimum for high average power and continued

broadening in the AsSe fiber. A total of around 300 mW average power was generated in this region, and especially the high peak power solitons above the 3.5 µm ZDW of the AsSe fiber seen in Figure 4.5.3(c) are expected to have significant impact on extending the long-wavelength edge.

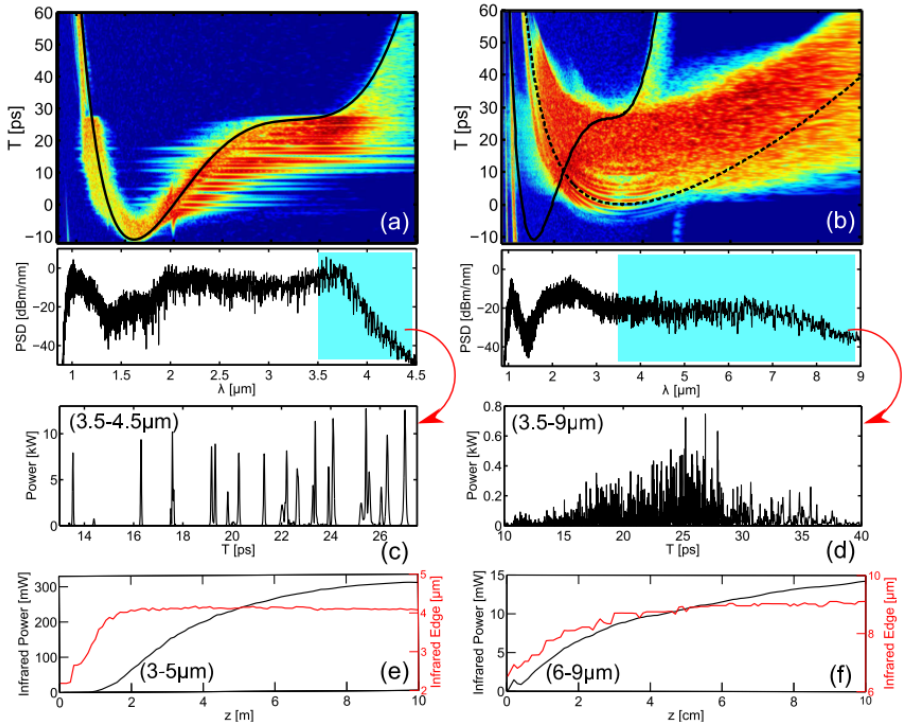

Figure 4.5.3: Single-shot simulation results for the cascaded 2 µm pump scheme. (a,b) Spectrogram for the ZBLAN and AsSe fiber SCG, respectively, with the output spectrum shown in the bottom. (c,d) Temporal characteristics of the 3.5-4.5 µm and 3.5-9 µm part of the ZBLAN ans AsSe spectra, respectively. (e,f) Evolution ZBLAN and AsSe SC long-wavelength edge and power in the 3-5 µm and 6-9 µm windows, respectively.

The spectrogram for the AsSe fiber in Figure 4.5.3(b) show very complex broadening dynamics, with the temporal trace in Figure 4.5.3(d) revealing that the ZBLAN solitons have broken up to a large amount of sub pulses from soliton fission. Near the ZDW there are signs of symmetric broadening from GV-matched solitons and DWs, but otherwise it is hard to clearly see the dynamics due to the density of pulses. The long-wavelength edge extended all the way to 9 µm (-30 dB level), and when comparing the spectrogram to the dashed $\beta_1 L$ line for the AsSe fiber it is apparent that the spectrum developed very rapidly. This

is also confirmed from the plot of the long-wavelength edge and power in Figure 4.5.3(f), which shows that within a few millimeters the spectrum was broadened to 7 μm. In conclusion, the 2.2 W pump power at 2 μm was first converted to 300 mW from 3-4.5 μm in the ZBLAN fiber, which resulted in around 39 mW from 3.5-9 μm generated in the AsSe fiber. These simulations was considered a mere proof-of-concept since they did not take the damage threshold of the AsSe fiber into account, and omitted HOMs and the coupling of power to both polarization states, which strongly limits the spectral broadening [111]. Furthermore, while Tm-doped fiber lasers are commercially available, they are still relatively expensive. If a pump source in the telecom band was used instead the source as a whole would be much cheaper. The use of inexpensive components will dramatically improve the commercial prospects of such a system, but pumping the ZBLAN fiber directly at 1.55 μm below the ZDW is not suitable. Silica fibers on the other hand are well suited to be pumped at 1.55 μm, generating efficient SC up to beyond 2 μm. The following section describes our work with cascaded SCG starting from a 1.55 μm seed.

4.5.3 Cascaded 1.55 μm Tm-Amplified laser pump scheme

(Based on journal paper [II], ref. [121])

In general, efficient SCG towards longer wavelengths requires pumping in the anomalous dispersion regime near the fiber ZDW, where soliton dynamics is dominating [42,94]. Standard silica SIF exhibits anomalous dispersion from around 1.3 μm all the way to the silica multiphonon absorption edge near 2.5 μm. Consequently, pumping a step-index silica fiber with a laser diode or erbium-doped silica fiber laser at 1.55 μm, inherently results in a SC where the long-wavelength edge is composed of solitons. Such a continuum has been found to be an excellent pump source for continued broadening in ZBLAN fibers through SSFS, because it extends above the ZDW of typical ZBLAN SIFs, which is around 1.6 μm [59]. Using this scheme efficient SCG in ZBLAN fibers has been demonstrated using various combinations of seed lasers and optical amplifiers [63,115,139,141]. Unlike silica the dispersion of ZBLAN SIFs is less well known due to the more complex composition of heavy-metals, and in fact these fibers may have a second ZDW before the mul-

tiphonon absorption edge, as was demonstrated in Section 3.3.1 (see Figure 3.3.3). The presence of a second ZDW completely changes the spectral-temporal dynamics of the long-wavelength part of the spectrum. As solitons shift towards the second ZDW the SSFS is halted due to an increasing transfer of energy to DWs that are phase-matched to a resonant wavelength in the normal dispersion regime across the ZDW. To conserve both energy and momentum the soliton frequency must shift in the opposite direction of the DW, thus counteracting the SSFS – an effect referred to as spectral recoil [94,146–148].

The average power of such a long-wavelength spectrum consisting of DWs can be equivalent or even higher than one consisting exclusively of solitons [148], which raises the fundamental question whether both spectra could be used for continued broadening in a chalcogenide fiber. This was still an open question at the time these results were published, since there had been no experimental results with coupling DWs, or cascading a ZBLAN SC into a chalcogenide fiber. Gattass et al. experimentally demonstrated SCG from 1.9-4.8 µm by launching a 2.4-2.5 µm silica continuum into two meters of As_2S_3 step-index fiber with 10 µm core diameter [114]. In their experiment the spectral broadening was limited by a strong absorption peak at 4 µm and the reduced efficiency of normal dispersion pumping in a large-core chalcogenide fiber.

The experimental setup for cascaded SCG is shown in Figure 4.5.4. The seed was based on a 1.55 µm semiconductor laser diode delivering 3 ns pulses at 40 kHz repetition rate, which generated around 400 mW SC from 1.5-2.2 µm in standard silica single-mode fiber. The continuum was then amplified to 1.25 W in a 10 µm core diameter Tm-doped silica fiber pumped at 790 nm, resulting in depletion of the wavelengths below 1.8 µm and extension of the long-wavelength edge to 2.7 µm. The addition of a Tm-doped fiber amplifier compared to an erbium-doped fiber amplifier was made to extend the long-wavelength edge in the ZBLAN fiber by boosting the long-wavelength solitons [63,141]. The amplified spectrum was then coupled to one of the two tested ZBLAN fibers and then further into a chalcogenide fiber by BD-2 aspheric lens telescopes. Coupling to the small chalcogenide fiber core was confirmed with the aid of a PbSe camera, and the resulting spectrum was measured using an FTIR spectrometer. Measurements of the intermediate silica and fluoride spectra were performed using a grating-based scanning spectrometer.

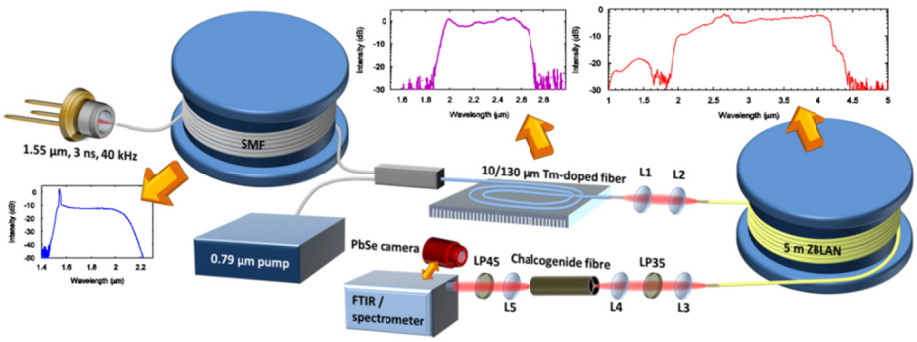

Figure 4.5.4: Experimental setup for cascaded SCG. A 1.55 µm laser diode delivering 3 ns pulses at 40 kHz repetition rate was coupled into a few meters of standard silica single-mode fiber (SMF) to generate a continuum from 1.5-2.2 µm (blue curve). This SC was coupled to around 3 m Tm-doped fiber pumped by a 0.79 µm laser to amplify and extend the continuum from 1.8-2.8 µm (purple curve). Aspheric lenses L1-L5 was used to couple the spectrum in and out of the ZBLAN/chalcogenide fibers. The long-wavelength part of the full ZBLAN spectrum (red curve) was filtered out with a 3.5 µm long pass filter (LP35) and coupled into the chalcogenide fiber. The output was collimated and analysed with an FTIR and PbSe camera. A 4.5 µm long pass filter (LP45) was inserted when measuring the power and spectrum generated at longer wavelengths.

The chalcogenide fiber used in the experiments was the same commercial $As_{38}Se_{62}$ SCF from Perfos discussed in Section 4.3.3, with a 4.5 µm core diameter, ZDW at 3.5 µm, and low loss in the 3.2-8.0 µm window [82]. The two ZBLAN fibers (A and B) were acquired from Fiberlabs Inc. ZBLAN A had a core diameter of 6.4±0.1 µm, ZBLAN B had a core diameter of 6.9±0.7 µm, and both fibers had a reported NA of 0.265. Note that ZBLAN A and B in this section corresponds to ZBLAN B and F in Table 2 and Figure 3.3.3. The dispersion of the fibers was measured from around 1.1-4.6 µm revealing two ZDWs in both fibers. The first ZDW was around 1.51 µm in both fibers, however, due to the smaller core ZBLAN A had a shorter second ZDW at 3.56 µm, and due to the larger core variation of ZBLAN B the second ZDW was found to vary from 4.37-4.43 µm. This difference in ZDW between the two fibers is essential to the experiment because it means that in ZBLAN A the long-wavelength edge of the spectrum consist of DWs generated beyond the second ZDW in the normal dispersion regime, whereas in ZBLAN B it consist entirely of solitons, as illustrated in Figure 4.5.5(a) and (b), respectively.

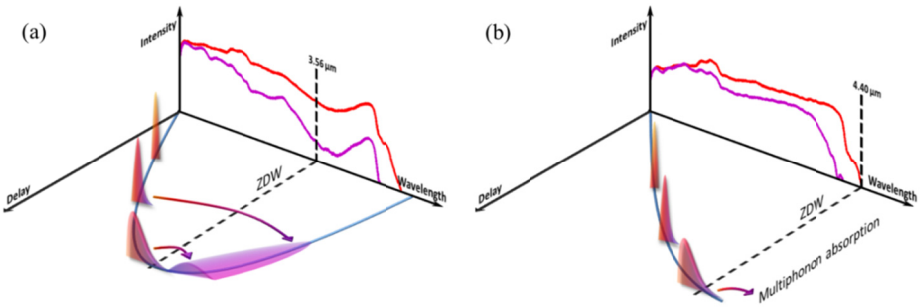

Figure 4.5.5: (a) Illustration of DW generation across the second ZDW. The experimental output spectrum of ZBLAN A is plotted in linear scale on the wavelength/intensity plane displaying the signature of initial DW generation across the ZDW (purple curve) and the subsequent continuum formation at higher power (red curve). (b) In ZBLAN B the long-wavelength edge is continuously shifted through SSFS up until the multiphonon absorption edge due to a longer ZDW.

The fundamentally different spectral-temporal dynamics was observed experimentally from the evolution of the long-pass filtered ZBLAN spectrum with increased pump power, as seen in Figure 4.5.6(a) and (b). The figure shows how the DW peak in ZBLAN A remains centered around 4.1 μm while growing with increasing power, whereas in ZBLAN B the edge of the spectrum shifts continuously due to SSFS. Red-shifted DWs and spectral recoiling has been thoroughly investigated in fibers with negative dispersion slope going from the anomalous dispersion regime towards the second ZDW, which is the case for both ZBLAN A and B. Energy transfer to the DWs increase with propagation length, i.e., as the soliton approaches the ZDW and the overlap between the DW and the soliton becomes stronger. However, while the energy of the solitons remain localized in time the DWs are spread in a tail travelling ahead of the solitons [146,147]. To our knowledge, such a pump source consisting of DWs has never been used in a cascading scheme before. While it may seem obvious that DWs should be inferior to solitons as a pump source, it is still interesting to investigate the efficiency of the scheme. Also, in this case the second ZDW of ZBLAN B coincides with the absorption edge of the fiber, which may reduce the efficiency of the soliton pumping scheme. In our experiments we investigated this by coupling the >3.5 μm long-pass filtered part of the ZBLAN SC into ~167.5 mm SCF. This way either exclusively DWs or solitons were launched into the anomalous dispersion regime of the fiber.

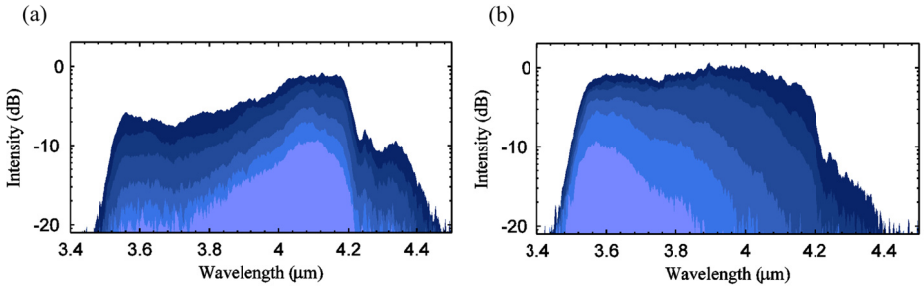

Figure 4.5.6: (a) Formation of a distinct DW peak at around 4.1 μm in ZBLAN A with increased power, eventually forming a continuum. (b) Red-shifting of the spectrum above 3.5 μm in ZBLAN B with increased pump power, displaying a continuous shift due to SSFS. The spectral dip around 4.25 μm in both cases is due to CO_2 absorption in the air.

In order to confirm the correctness of the experimental results a series of SC simulations were performed in an attempt to reproduce the experimental observations. Pulse propagation was again simulated using the numerical method described in previous sections [77,119,133]. For convenience we limited the simulated pulse duration to 20 ps, and to match the experimental results in the silica fiber we used a diode laser peak power of 10 kW and a fiber length of 10 m. The dispersion was modelled using a simplified dispersion relation from the specifications of Corning SMF28. The loss was determined empirically by incorporating appropriate loss edges modelled as Gaussian high- and low-pass filters and a Gaussian OH-absorption at 1.3 μm to give a good match to the experimental results. The Tm-doped silica fiber model included additional absorption and emission bands for the Tm transitions modelled as broad Gaussian loss and gain peaks centered at 1.6 μm and 1.9 μm, respectively, similar to Figure 2.1.5. Before further propagating the Tm-amplified spectrum the time-window was wrapped around, so the short-wavelength edge was shifted to the end of the window to allow for additional temporal broadening in the ZBLAN fiber without changing simulation parameters. Such a shift had no impact on the simulations, since the time axis is relative. A fiber length of 4.25 m with a gain of 4.13 dB/m was used to match experimental observations. Because the spectral-temporal dynamics in the ZBLAN fibers are essential to the experiments, they were modelled much more accurately using the measured dispersion. The loss and numerical aperture (NA) were provided by the manufacturer (NA=0.265 assumed to be constant). The wavelength dependent effective area and nonlinear parameter were calculated using

COMSOL Multiphysics, incorporating the given fiber parameters, and coefficients for the Kerr effect and delayed Raman response found in the literature [60,77,94]. The silica spectrum was multiplied with a factor of 0.9 before further propagation in the ZBLAN fibers to better match experimental spectra. The results of the silica and ZBLAN simulations are shown in Figure 4.5.7.

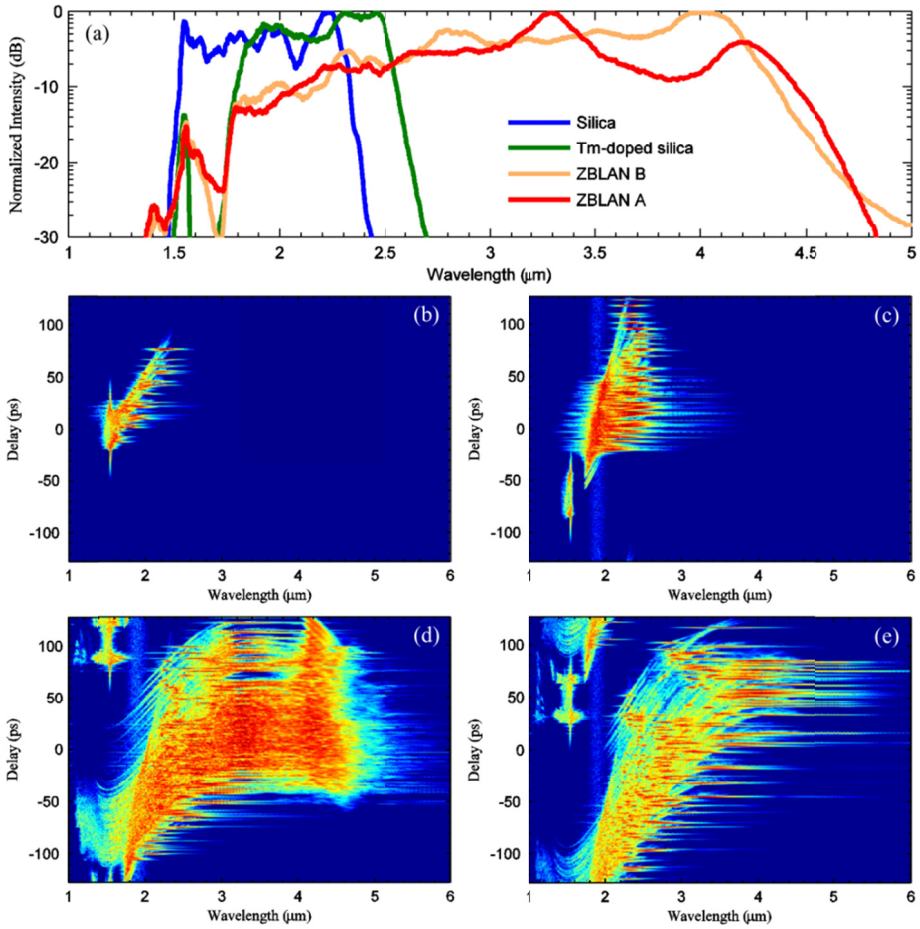

Figure 4.5.7: Simulation of SCG in silica and ZBLAN fibres. (a) Spectrum at the output of the silica and ZBLAN fibres. The spectral-temporal composition is displayed in corresponding spectrograms for (b) standard silica fibre, (c) Tm-doped silica fibre, (d) ZBLAN A, and (e) ZBLAN B, respectively. The spectrograms are normalised to the maximum value and scaled from 0 dB to -80 dB.

Figure 4.5.7 shows the normalized output spectra from the different simulated silica and ZBLAN fibers, while the remaining windows (b-e) show the corresponding intensity-normalized spectrograms of the spec-

tral-temporal composition at the output of the fibers. The expected dynamics of red-shifted DW generation (d) and continuous SSFS (e) is evident from the spectrograms. It is also evident that a small portion of the short-wavelength spectrum has wrapped around in the time-window, however, this part of the spectrum is relatively weak and was filtered out before propagation in the suspended-core fiber. A length of 15 m of ZBLAN fiber was needed in order to push the DW peak of ZBLAN A close to the experimentally observed peak at 4.15 µm. This discrepancy may be due to measurement uncertainty of the dispersion slope (β_3), which has an impact on the wavelength of the DW generation, as seen from Eq. (2.3.29).

As a result, coupling solitons from ZBLAN B provided almost 1.5 µm increased spectral broadening (10 dB bandwidth) compared to the DWs from ZBLAN A, as seen in Figure 4.5.8(a) and (b) for comparable output power levels of 4.46 mW and 4.48 mW, respectively. Measurements with comparable output power rather than pump power were chosen to account for changes in coupling to the SCF fiber. The spectra were corrected by blackbody calibration and the dataset was limited on the short-wavelength side to 2.8 µm due to the detection limit of the FTIR.

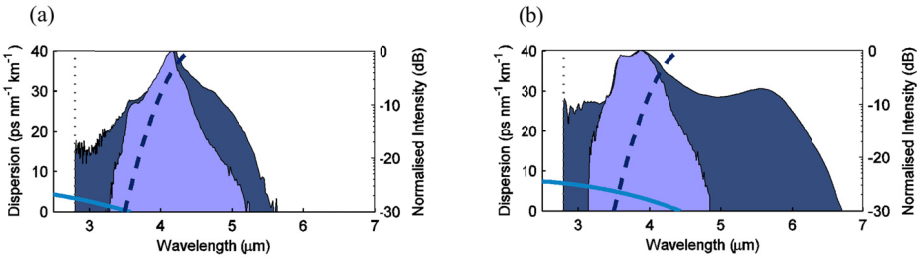

Figure 4.5.8: Experimental results with cascaded SCG efficiency for the ZBLAN A (a) and B (b) configurations with comparable output power levels of 4.48 mW and 4.46 mW, respectively. The solid and dashed lines represent the measured dispersion of the ZBLAN and chalcogenide fibers, respectively.

Further insight into the spectral-temporal dynamics was gained by simulating both pump cases. The full dispersion of the SCF was obtained using COMSOL based on the refractive index of AMTIR glass [133]. The nonlinear operator was again calculated using COMSOL, incorporating the modelled Kerr coefficient from Romanova et al. [56] and the delayed Raman response measured by Ung and Skorobogatiy [128]. Estimation of fiber loss was performed as refs. [82,133]. Before propagation in the chalcogenide fiber the ZBLAN spectra were long-pass filtered and mul-

tiplied by a dampening factor of 0.21 to match experimental observations. This corresponds to a coupling loss of -6.8 dB which is reasonable for this fiber material and geometry. The ZBLAN A pump spectrum was then equalized with the ZBLAN B pump spectrum in terms of summed average power to make the two comparable.

Figure 4.5.9(a) shows a comparison between the experimental and simulated spectra for the ZBLAN A pump case. It can be seen from the input (b) and output (c) spectrograms that solitons, seen as temporally narrow horizontal lines between -25 ps and 10 ps, slowly develop from the DW radiation. However, a large part of the spectrum exhibit very little spectral broadening due to the low-amplitude nature of the DWs.

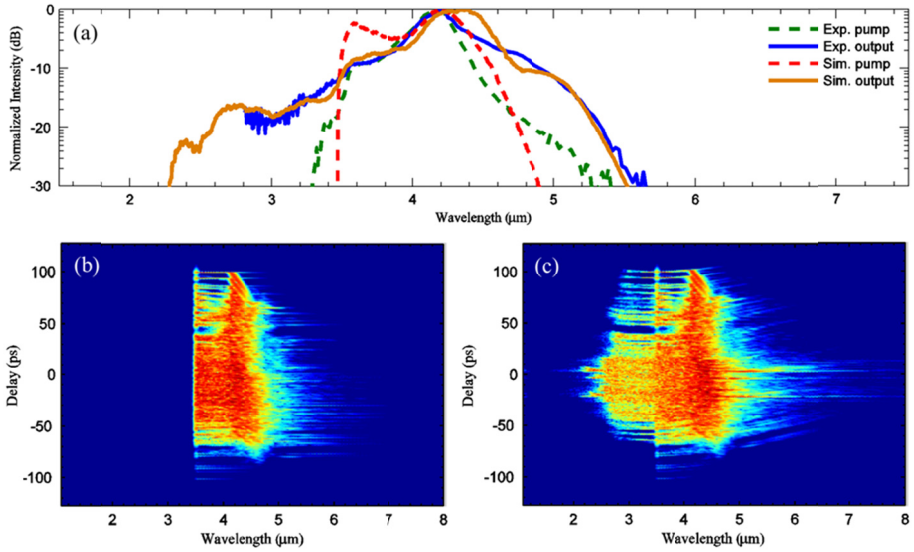

Figure 4.5.9: (a) Comparison between the experimental and simulated pump/output spectra for the ZBLAN A pump case. (b,c) Corresponding normalized simulation spectrograms for the filtered ZBLAN A pump, and output after 170 mm propagation in the suspended-core fiber, respectively.

Our simulations show that a much longer fiber is needed for the spectrum to develop, which makes the chalcogenide fiber losses a limiting factor. In the ZBLAN B pump case, spectral broadening in the chalcogenide fiber is assumed to be largely dominated by soliton fission and subsequent SSFS due to the large increase in the nonlinear Kerr coefficient from $n_2 = 2.2 \times 10^{-20}$ $\mathrm{m^2W^{-1}}$ in ZBLAN [59,77] to $n_2 = 5.72 \times 10^{-18}$ $\mathrm{m^2W^{-1}}$ in As_2Se_3 [56] and the greatly reduced effective modal area. This causes a large increase in the order of the injected solitons,

which consequently breaks up within a very short length of fiber into a large amount of fundamental solitons that may continue to red-shift and collide [145]. This was also corroborated by the simulations, which shows a large number of red-shifting solitons, as seen in Figure 4.5.10.

In both cases the absence of blue-shifted DWs in our experiments is explained as a combination of reduced sensitivity of the FTIR spectrometer used in our measurements and a large OH loss peak at 2.9 μm due to contamination and diffusion of water vapor from the atmosphere. The output power and long-wavelength edge of the spectrum was limited by the typical large losses associated with coupling to a small-core chalcogenide fiber, including the 22 % Fresnel reflections, and by optically induced damage to the fiber facet, which occurred above 53 mW average pump power. Damage was observed at fairly low pump powers due to the thermal isolation of the core and the very fragile suspending struts. Still this type of fiber was chosen over more robust designs due to the ZDW at 3.5 μm, which was ideal for this experiment. The bandwidth limit presented here thus represents the limitation of the chalcogenide fiber, rather than the cascading scheme itself.

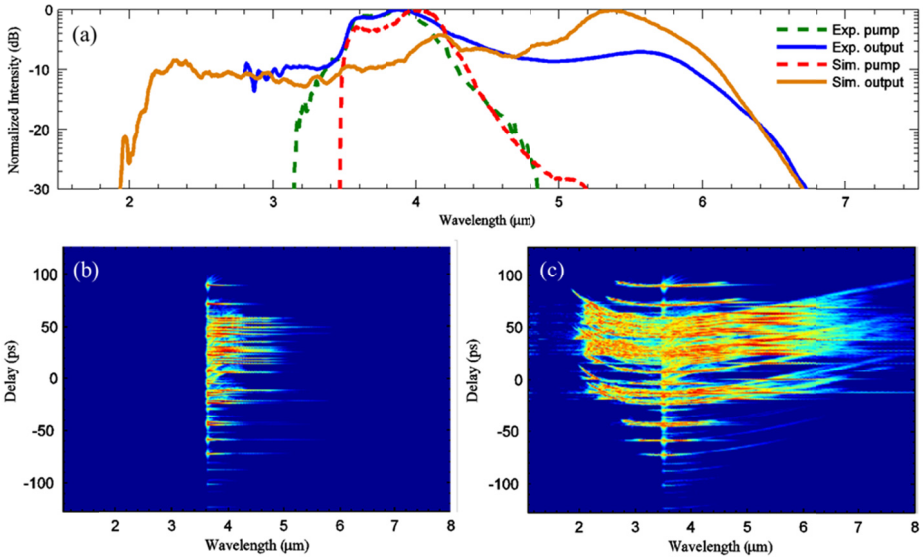

Figure 4.5.10: Comparison between the experimental and simulated pump/output spectra for the ZBLAN B pump case. A clear peak at around 5.5 μm is seen in both cases. (b,c) Corresponding spectrograms for the filtered ZBLAN B pump spectrum, and output after 165 mm propagation in the suspended-core fiber, respectively.

In fact, a high-NA chalcogenide SIF with a ZDW of 3.2 μm was recently demonstrated [67], which should allow for further power scaling.

Even so, with the ZBLAN B pump and using a maximum pump power of 51.4 mW before the in-coupling lens a continuum up to 7.0 µm with a total output power of 6.5 mW and 1.5 mW above 4.5 µm was obtained after collimation, showing good qualitative agreement with the simulated spectrum as seen in Figure 4.5.11. These results are comparable to the results with direct MHz-kW pumping in Section 4.3.3. Thus we demonstrated as the first the experimental feasibility of such a cascading scheme, while also demonstrating the importance of careful control over the fiber dispersion to obtain solitons at the long-wavelength edge of the pump spectrum for efficient cascaded SCG. Supported by numerical simulations our results reveal that an SC consisting of DWs was very inefficient as a means of extending the spectrum further into the mid-IR. To achieve similar results pumping with dispersive waves would require longer lengths of fiber and higher average power, which means that the efficiency of the DW generation should be significantly higher than the efficiency of generating long-wavelength solitons with SSFS in a soliton pump fiber to give any merit to such a scheme.

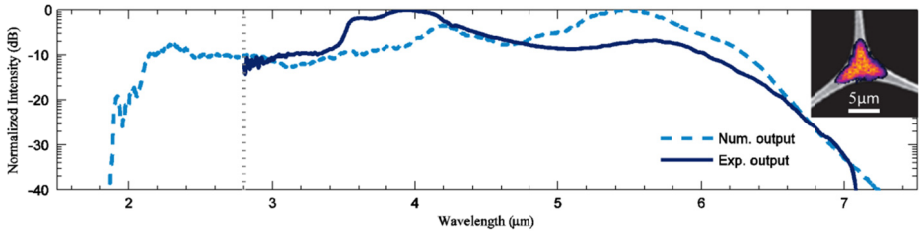

Figure 4.5.11: Broadest experimental spectrum (solid line) from soliton cascaded SCG with a total output power of 6.5 mW and 1.5 mW above 4.5 µm, and the corresponding simulated spectrum (dashed line). The inset shows the near-field image of the output beam superimposed on a scanning electron microscope image of the suspended-core region from Perfos.

For comparison with previous results the spectral broadening and PSD is plotted in Figure 4.5.12. The spectral evolution shows that the spectrum is likely only limited by the maximum pump power before optical damage. Therefore, more robust fibers were investigated.

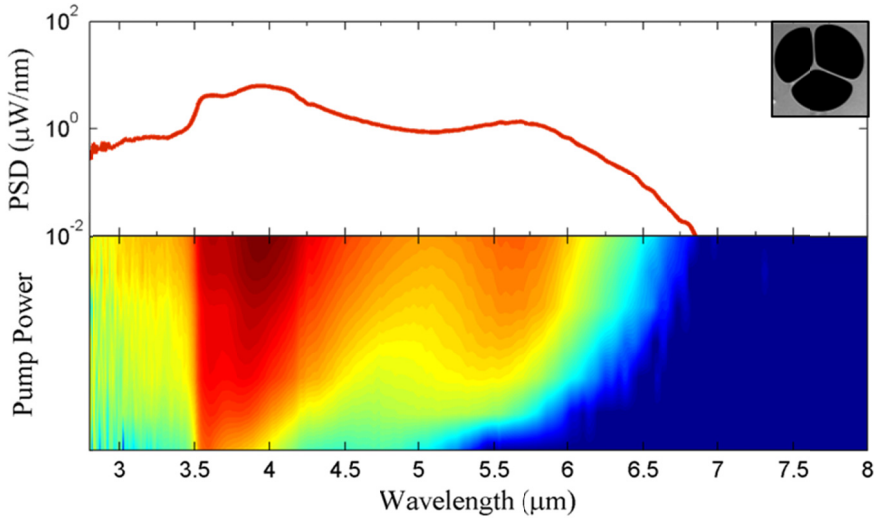

Figure 4.5.12: (Top) PSD of the cascaded ZBLAN-SCF spectrum at a maximum pump power of 51.4 mW, resulting in 6.5 mW total average output power, and 1.5 mW > 4.5 μm. Inset shows the fiber end-facet cross section. (Bottom) Spectral evolution with increased pump power, revealing asymmetric broadening of the pump towards the longer wavelengths indicative of soliton dynamics with corresponding DWs below the ZDW.

4.5.4 Photonic Crystal Fiber

(Based on conference paper [i], Ref. [149]*)*

Having identified that the soliton-based ZBLAN SC pump spectrum gave the best results, we repeated the experiment with the commercial $Ge_{10}As_{22}Se_{68}$ PCF from Perfos with around 13 μm core diameter. At a maximum pump power after the long-pass filter of 135.7 mW, we obtained a continuum up to 7.2 μm with a total output power after the collimating lens of 54.5 mW, and 3.7 mW above 4.5 μm [149]. The low power conversion above 4.5 μm was primarily due to the large core diameter and ZDW around 4.6 μm, resulting in normal-dispersion pumping. The spectral broadening shown in Figure 4.5.13 for a similar experiment (113.7 mW pump, 43 mW output power, 3.4 mW >4.5 μm), which displays the highly asymmetric broadening behavior of the ZBLAN pump. The short-wavelength edge was only shifted by around 100-200 nm, whereas the red-edge is shifted around 2500 nm at the -20 dB level. This suggests a combination of SPM, XPM, and FWM between the ZBLAN solitons caused the initial broadening and transfer of energy across the ZDW [42]. The red-shifted part of the spectrum coupled to the anoma-

lous dispersion regime and generated solitons that continued to broaden through SSFS. Increasing the length of the fiber to 40 cm was found not to improve the spectral extend or power conversion above 4.5 µm, which suggest that the short fiber is sufficient to obtain maximum spectral broadening with the current setup. Nonetheless, we demonstrated a factor of 8.4 higher total continuum power, and a 2.5 increase in power above 4.5 µm compared to the previous results with the $As_{38}Se_{62}$ SCF [121]. Key to this achievement was the increased coupling efficiency and damage threshold that comes from the larger core area and better thermal conductivity between the fiber core and cladding. The higher glass transition temperature and resistance to crystallization may also have had an impact on the performance of the fiber [68].

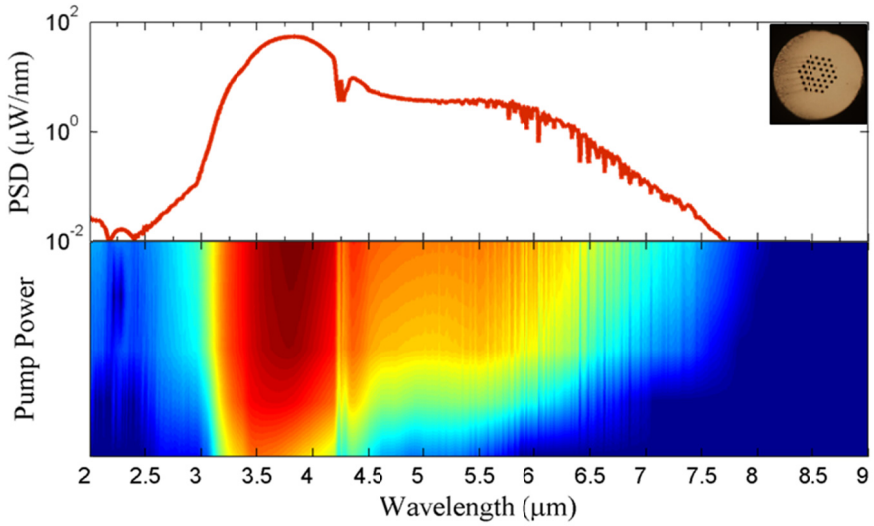

Figure 4.5.13: (Top) PSD of the cascaded ZBLAN-PCF spectrum at a maximum pump power of 113.7 mW, resulting in 54.5 mW total average output power, and 3.7 mW > 4.5 µm. Inset shows the fiber end-facet cross section. (Bottom) Spectral evolution with increased pump power, revealing weak broadenin of the main peak due to normal dispersion, and asymmetric broadening of the pump towards the longer wavelengths indicative of SSFS.

To improve this result the experiment was repeated using a tapered PCF.

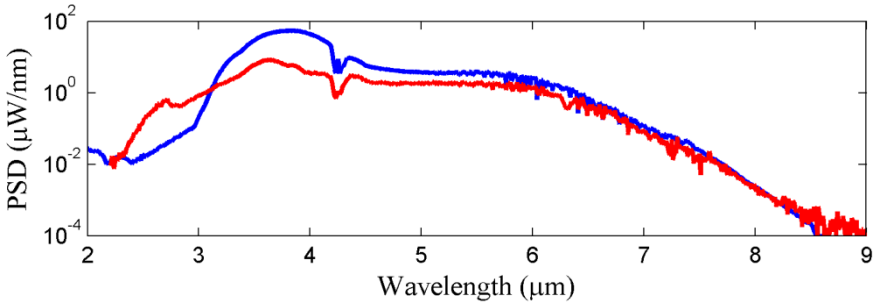

Figure 4.5.14: Comparison between the ZBLAN-PCF output spectrum in the tapered (red) and untapered (blue) PCFs. In the tapered PCF spectrum the total average power was reduced to 9 mW, but the power >4.5 µm was 3.34 mW, almost the same as in the untapered case.

In conclusion, by demonstrating cascaded SCG we presented an alternative route to chalcogenide fiber-based mid-IR SC sources using a double-cascading configuration. By starting from a cheap 1.55 µm laser generating an SC in standard silica fiber, amplifying, and coupling this into a fluoride fiber with carefully designed dispersion, and then finally coupling this into a chalcogenide fiber with a suitable low ZDW, a SC can be generated up to 7 µm with several mW of average power. Provided that a compact, all-fiber configuration can be realized, the cascaded pump scheme could prove commercially viable. Optimization of the seed parameters, lengths of fiber, and an optimized chalcogenide fiber should improve these results.

4.6 Summary and conclusion

In the introduction to the chapter it was made clear that there is a lot of research devoted to mid-IR SCG, and results presented in this chapter is well represented in all three pump configurations, as seen in Figure 4.1.1. However, there is little focus on practical applications and demonstrations. Many papers focus only on the spectral bandwidth, and therefore fail to provide e.g. the average output power, which makes it difficult to compare different results. Figure 4.6.1 show some PSD plots of results presented in this chapter, which makes it easy to compare different results in terms of effective bandwidth. For example, although the MW-kHz result obtained the broadest bandwidth, the kHz-MW result with the tapered PCF achieved better PSD from 2-9 µm. In fact, re-

sults with kW-MHz pumping seem most promising in terms of bandwidth and average output power for realizing mid-IR spectroscopic and imaging applications. However, realizing a compact, all-fiber system using cascaded SCG would help in bridging the gap between technology and user, bringing the mid-IR SC sources to the application, rather than having to bring the applications into the SC labs.

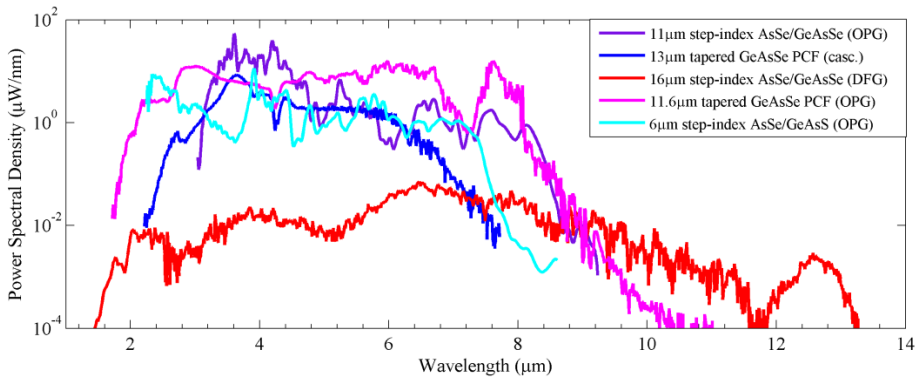

Figure 4.6.1: Comparison between the PSD of various results presented in the chapter.

Chapter

5

Applications in Spectroscopy and Imaging

"I suppose it is tempting, if the only tool you have is a hammer, to treat everything as if it were a nail."

— Abraham H. Maslow, Toward a Psychology of Being

One of the early predictions regarding SCG, was that it would prove useful in a wide range of application, such as telecommunications, metrology, spectroscopy, and imaging [42,109]. To date there has been many proof-of-concept demonstrations of visible to near-IR SC driven mainly by applications in biophotonics and life sciences. Especially in the field of biological imaging SC sources has been employed extensively in such diverse modalities as OCT [26,27], photothermal microscopy [150], fluorescence microscopy [25], and multiphoton microscopy [151]. The latter demonstrated an impressive combination of two- and three-photon auto-fluorescence, second-harmonic generation, THG, Raman scattering, and coherent anti-Stokes Raman scattering for stain-free histopathology of tumorous tissues – all using the same SC source. Needless to say visible/near-IR SC sources have been widely accepted as the state of the art technology in many such applications, and some would even deem it a commercial success. However, when it comes to the mid-IR spectral region, SC sources are lagging behind other technologies in application-based demonstrations, such as QCLs and tunable lasers. The goal of this chapter is to identify potential applications of mid-IR SC sources based on the strengths and drawbacks of the technology, and to provide proof-of-concept demonstrations.

5.1 INTRODUCTION

When it comes to identifying applications of mid-IR SC it is tempting to simply transfer applications from the near-IR. However, there are several things that must be taken into account when switching to the mid-IR. Figure 5.1.1 shows a crude illustration of one of the major differences between near-IR and mid-IR, which is that while Rayleigh scattering is reduced at longer wavelengths the absorption from the fundamental resonances can be several orders of magnitude higher. For instance in skin OCT the expected improvement in penetration due to reduced scattering is dwarfed by a drastic increase in the absorption of water, but for mid-IR transparent materials such as ceramics OCT has indeed been proposed for non-destructive testing [152].

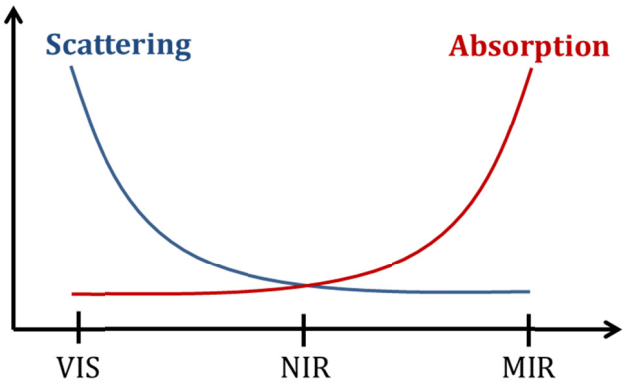

Figure 5.1.1: Qualitative illustration of the inverse relation between scattering and absorption for the VIS, near-IR, and mid-IR spectral ranges.

Another example is within gas-phase spectroscopy, where moving from the near-IR to mid-IR should improve the chemical specificity and the sensitivity due to the increased absorption [153]. However, there are several factors that makes it difficult to do the transition, including noise and lack of low-cost high-performance laser components in the mid-IR. Regarding noise, Y. Yu et al suggested a polarization-maintaining system is needed to avoid noise from fluctuations in the polarization state, and a dual-beam configuration is necessary to normalize each point in the measured sample spectrum with a reference signal measured simultaneously from the same pulse sequence, to avoid noise from spectral variations in the SC [154]. Cezard et al. reported a 1/f noise comparable to ther-

mal emitters from a ZBLAN fiber-based SC source, but also noticed spectral variations with polarization [9]. Nevertheless absorption spectroscopy has been demonstrated [9,154–156], although the applications are usually simple demonstrations on standard samples, such polystyrene or similar. Much more advanced applications has been demonstrated using QCLs, such as monitoring dynamic changes of protein secondary structure in aqueous solutions [7], and large scale infrared imaging of tissue micro arrays [21]. Similar applications should be demonstrated in order to establish SC sources as a promising technology for mid-IR. Potential applications should carefully consider the advantages of SCG. To this end some of the advantages and disadvantages of SC sources, as perceived by the author, is presented in Table 3:

Feature	Advantage	Disadvantage
Broad spectrum	Potential for fast, real-time applications through spectrum-time transformation [158], or by using array spectrometers.	Low local PSD. Power may be wasted in parts of the spectrum where it is not needed.
Fiber based (light is born in the fiber)	High compatibility with fiber sensing, such as fiber evanescent wave spectroscopy [18,48,52,157–159], fiber imaging bundles [160], or fiber tip microspectroscopy [49].	Power is lost when coupling light in and out of the fiber.
Nonlinear technique	Potential for nonlinear applications, such as. photoacoustic spectroscopy [23,161], or photothermal microscopy [150].	Relatively high noise. Polarization scrambling.
Diffraction-limited, spatially and spectrally coherent	Compatible with fibers, may be focused to small sample areas for localized probing, and can be used in interferometry.	Unsuitable for wide-field imaging. Coherence effects, such as interference may affect imaging performance.

Table 3: Advantages and disadvantages of various features of SC sources.

5.2 Skin Cancer Screening

Continuing on the topic of skin, I have been very much involved with the European research project MINERVA (MId- to NEaR infrared spectroscopy for improVed medical diAgnostics), a project which as explained in conference paper [ii] is working towards realizing the so-called "optical biopsy" for fast and non-invasive diagnosis of early-stage skin cancer [53]. The project envision the use of mid-IR SC in order to cover the broad range of target wavelengths identified as relevant in the context of skin cancer (see Figure 5.2.1).

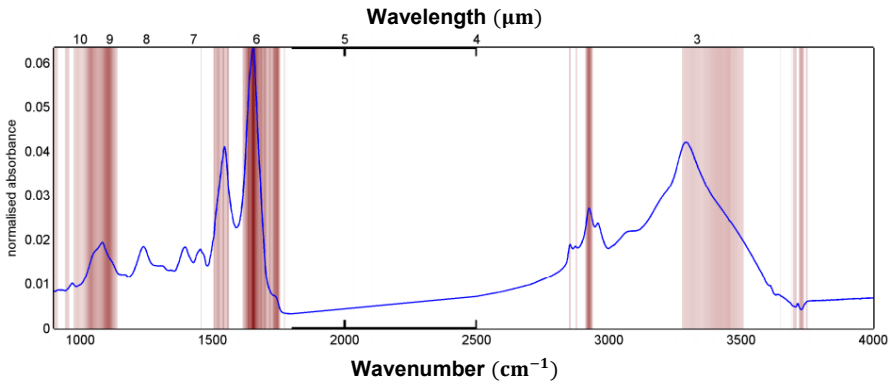

Figure 5.2.1: Identified wavenumber targets for the MINERVA project (red), and a reference skin spectrum (Source: MINERVA project newsletter #3).

The original idea was to use the mid-IR SC source for wide-field hyperspectral imaging in combination with high-resolution IR cameras – a technique that has already been employed successfully in MINERVA using a Globar light source in combination with FTIR for investigation of individual cellular and histopathological features in colon tissue [162]. A prototype wide-field hyperspectral-imaging system employing a ZBLAN-based SC source from NKT Photonics with a 5 µm spatial resolution was also successfully demonstrated [163], but as described later by Lindsay et al. in [24] the brightness advantage of SC sources over traditional thermal sources stems from their nearly diffraction limited beam capabilities. In wide-field imaging the beam is expanded to cover the entire sample and detector area in order to obtain a high spatial resolution, but in the process the brightness advantage is diminished, reducing the comparison to one of purely total PSD. Figure 5.2.2 show a comparison of the PSD of various mid-IR light source configurations calculated

by Ian Lindsay as part of the MINERVA. In the diffraction-limited case, depending on the wavelength range, SC sources have around 5-7 orders of magnitude higher PSD compared to thermal sources, and about 1-3 orders of magnitude higher than synchrotrons. However, if the thermal emitter is imaged by a 15× reflective objective it can out-perform the synchrotron in terms of PSD, and is either on par or maximum 1-2 orders of magnitude below the SC sources. This demonstrates that the advantage of SC sources is utilized best in diffraction-limited modalities.

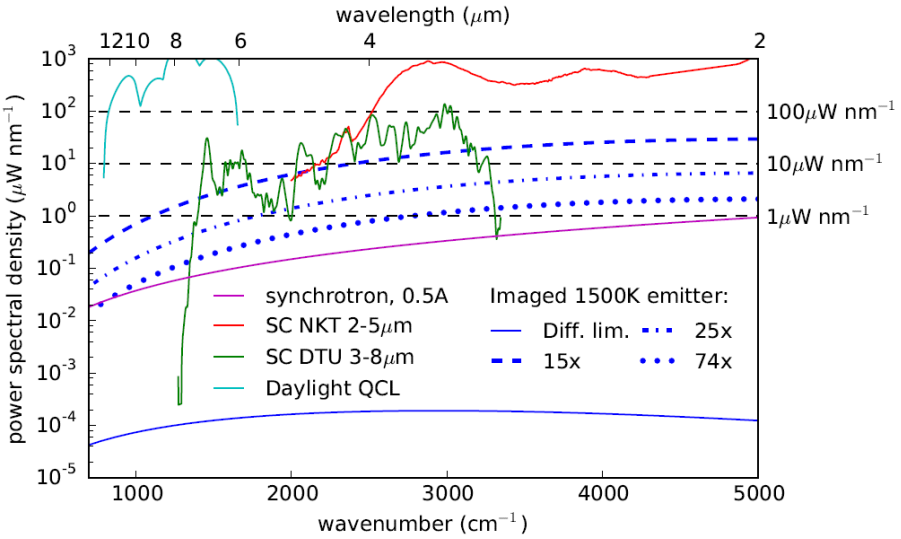

Figure 5.2.2: Comparison of the PSD of different broadband mid-IR sources. The figure illustrates that the real advantage of SCG is the diffraction-limited beam. (Provided by courtesy of I. Lindsay through the project MINERVA).

For this reason the focus was changed towards a scanning solution, which reduces both the PSD requirements and the complexity on the detection side. The concept was demonstrated with a ZBLAN fiber-based SC source by Dupont et al. [164] in which a spatial resolution of 5 μm was achieved by focusing the collimated beam onto a sample, and then raster-scanning the sample in x,y via a translation stage. A more practical system that avoids the use of free-space optics near the sample is illustrated in Figure 5.2.3. Since the SC is born in the fiber, it is convenient to use a mid-IR fiber for delivery and collection of light at the sample, which would also make it easier to use in a clinical environment. This approach thus takes advantage of the strengths of SCG, namely the

high brightness in a diffraction-limited beam, and the compatibility with optical fiber circuits.

As project partner in MINERVA we were supplied with artificial skin phantoms for testing in combination with our SC source. The phantoms were fabricated by the group of Dr. Juergen Schnekenburger at University of Münster. Figure 5.2.4(a) shows a picture of the skin phantom, which was a 500 µm thickness EpidermFT skin model, having an irregular, layered, and thus scattering structure very similar to real skin. Figure 5.2.4(b) shows an image of the observed speckle pattern from transmitting the SC light through the sample at the low-absorption wavelength of 5 µm, selected using a monochromator. Figure 5.2.4(c) shows a test spectrum measured using the SC from an untapered GeAsSe PCF (having the highest average power at the time of the experiment), with the sample placed at the entrance slit of the monochromator, and detected with an MCT detector. The spectrum shows the same qualitative features of Figure 5.2.1, although it is expected to be significantly improved using the higher average power available from the tapered PCFs, and with the sample placed closer to the detector to avoid excess scattering loss.

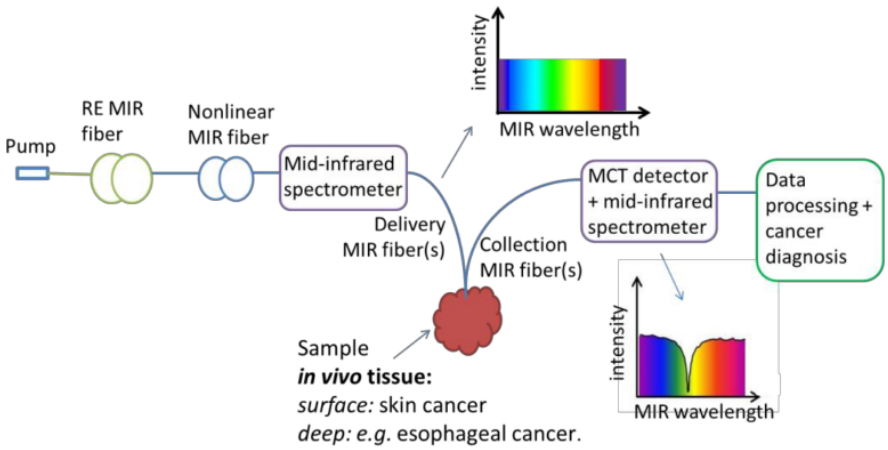

Figure 5.2.3: Concept schematic for the optical biopsy. Note that here mid-infrared spectrometer simply means a wavelength selection device, and so only one is needed and preferably on the detector side (From conference paper [ii]).

The fact that we were able to penetrate 500 µm of skin demonstrates that we can expect to detect diffuse reflection and scattering from a depth of at least 250 µm, and since skin cancer develops from the

surface of the skin this may very well prove sufficient. Because the MINERVA system is also aiming for a diffuse reflectance probe, the skin phatom was also measured in diffuse reflectance. The setup which is shown schematically in Figure 5.2.5(a) featured a silver-halide fiber probe with an IR lens mounted at the end, which was connected to the FTIR spectrometer. The fiber probe was placed close to the phantom and kept at the lowest possible angle without obscuring the beam.

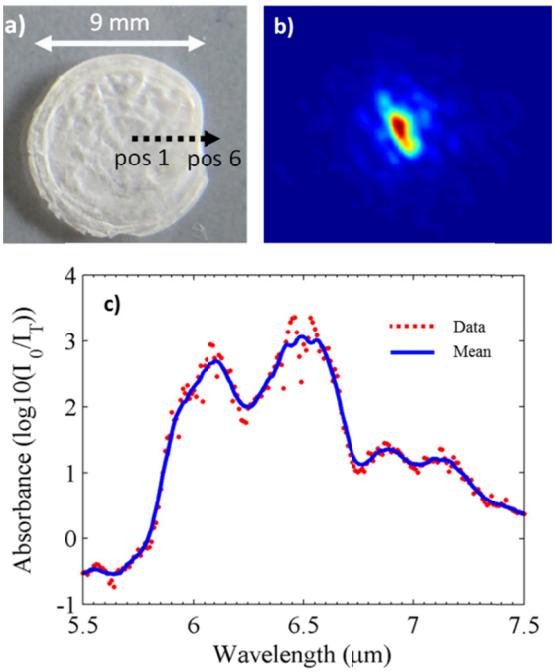

Figure 5.2.4: (a) Artifical skin model (phantom) measuring about 11 mm in diameter, and thickest at the center. (b) Speckle pattern observed when launching the output beam from a GeAsSe PCF through the skin phantom. (c) Absorption spectrum of the skin phantom placed at the input of the monochromator, and measured with a MCT detector.

Figure 5.2.5(b) shows an example of the normalized absorption spectra measured using the fiber probe in transmission (absorption) and diffuse reflectance (reflection). The spectra show several discrepancies which may be due to coherence effects. A. Michel et al. reported a strong angular dependence on the spectral shape of mid-IR light reflected from skin when using a QCL compared to a thermal source, but they could not fully explain their observations [165]. It is clear that further investigation is

needed before diffuse reflectance can be considered as a viable modality over transmission.

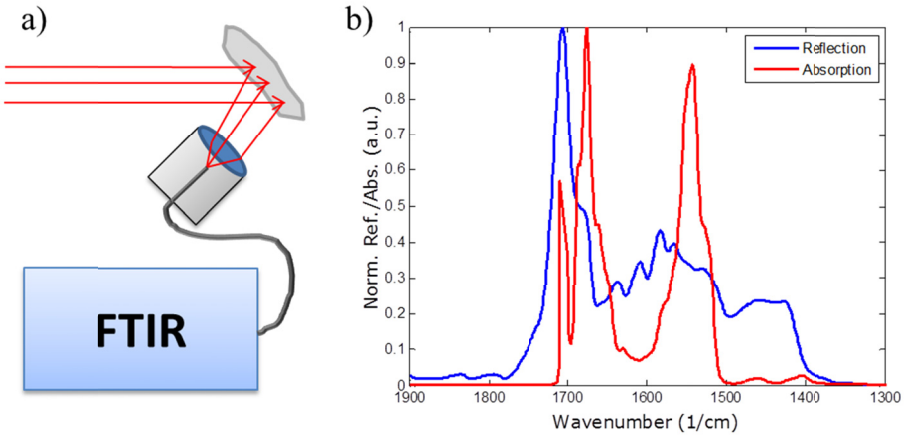

Figure 5.2.5: (a) Schematic for the diffuse reflectance measurements. (b) Comparison between diffuse reflectance (reflection) and transmission (absorption) spectra for the skin phantom, measured with a fiber-coupled FTIR.

5.3 Ultrafiltration Membranes

Another application that is problematic due to strong scattering is monitoring of residual fouling of ultrafiltration (UF) membranes, used to concentrate sweet whey from milk in the dairy industry, as illustrated in Figure 5.3.1(b). The membranes require daily cleaning, and consequently the dairies use massive volumes of water every day in order to maintain the required hygienic standards. This results in a significant loss of water resources, consumption of chemicals, and production downtime [14]. Furthermore, the cleaning procedures only remove the main fouling layers of the membrane, leaving some irreversible residual fouling that eventually requires replacing the membrane. For this reason there is a need for better knowledge of the membrane cleanliness state. Recently Jannie Jensen from the Department of Food Science at Copenhagen University investigated residual fouling of UF membranes from the dairy industry, by infrared attenuated total reflectance (ATR) [14]. One issue with ATR is that it is a surface technique, and so to make sure that residual fouling of the deeper membrane layers are also included in the analysis, the membranes must be measured in transmission. However, due to the high absorption and scattering from the membranes,

standard FTIR transmission methods was not possible, but with the added brightness and spatial coherence of our SC source we were able to perform a proof-of-concept experiment.

Together with Trine Ringsted from the Department of Food Science at Copenhagen University, we were allowed to re-use the UF membrane sheets from the ATR experiment. The membrane was made from polyethersulfone (PES), and the five square sheets used in this experiment came from different parts of a 1x1 m membrane segment. Figure 5.3.1(a) show the experimental setup, in which the beam from a tapered GeAsSe PCF (49 mW total power, 18 mW > 4.5 μm) was transmitted through the roughly 1 mm thick membrane. The transmitted signal was collected using the lensed FTIR fiber probe.

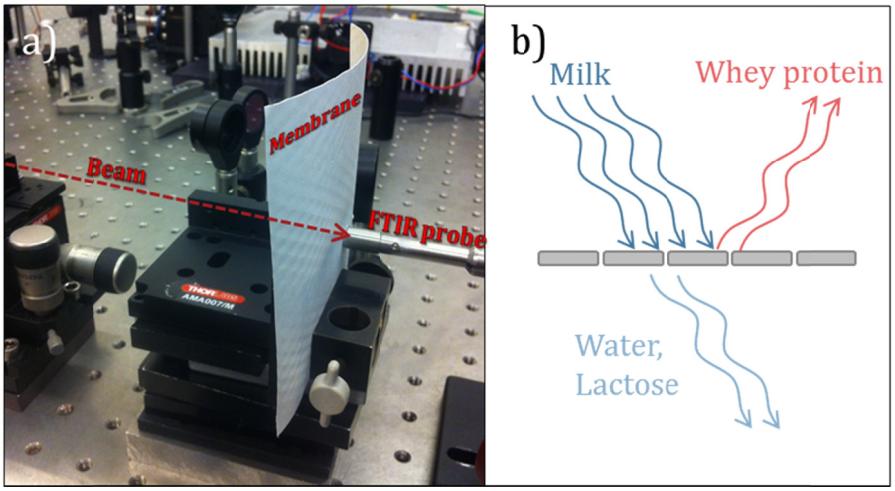

Figure 5.3.1: (a) Picture of the membrane transmission setup showing the beam passing through a sheet of UF membrane, and the signal is collected by the FTIR probe. (b) Illustration of the UF membrane up-concentration of whey protein.

Five fouled sheets and a single clean sheet where each measured in all four corners about 2 cm from the edge, and each measurement was repeated over ten consecutive scans. Figure 5.3.2 show the mean absorption spectra of the fouled sheets after subtracting the spectrum for the clean membrane to account for the absorption of the PES material. For reference the dashed black line of the figure show the absorption of the clean membrane with respect to the air background (scaled for better visibility). The variance in baseline is most likely due to different amount of scattering between individual sheets, and can be corrected by

using various post-processing techniques if required [1]. In the ATR experiments fouling was observed from the presence of amide I (1,645–1,670 cm^{-1}), amide II (1,500–1,550 cm^{-1}), and the trace of fat in the carbonyl region (1,720–1,760 cm^{-1}). Hausmann et al. reported that fouling in polytetrafluorethylene whey membranes gave rise to peaks mainly in the 2800-3000 cm^{-1} carbohydrate region (C-H stretching), in the 1500-1700 cm^{-1} nitrogen region (N-H bending), and an ester peak around 1730 cm^{-1} (C=O) [166].

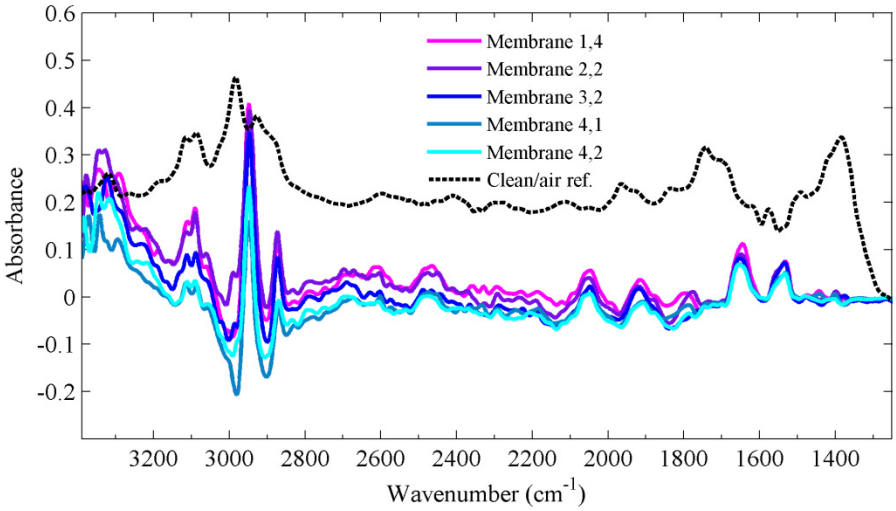

Figure 5.3.2: Mean absorbance spectra of the clean and fouled membranes (colored curves). For reference the clean membrane spectrum is shown with an air background, scaled for visibility (dashed line).

From our spectra we observed clear peaks around the amide I and II bands of proteins and peptides at 1650 cm^{-1} and 1540 cm^{-1}, respectively [1]. The band around 3100 cm^{-1} could possibly be the first overtone of the amide II, and the features at 3300 cm^{-1} may be due to the N-H stretching of amines [1]. The C-H stretching region from 2850-3000 cm^{-1} corresponds to the acyl chain of fatty acids, but no C=O peak around 1750 cm^{-1} was observed, which suggest that it is not from fat but instead from other fouling organics [1,166]. The features between 1800-2100 cm^{-1} are difficult to explain, since there should be no vibrational modes in the region from 1800-2800 cm^{-1}, but since it is fairly close to the zero baseline it is assumed to be some artefact of the measurement.

In order to evaluate whether the six membrane sheets displayed significant variations over the entire measured spectrum, a so-called principle component analysis (PCA) was performed. Briefly, based on the measured data the PCA constructs a number of mutually orthogonal basis vectors (principle components, PC), that each account for some percentage of the spectral variation. From these principle components, the individual data sets can be assigned a different weight (loading) to each PC. If two data sets are significantly different, they should therefore be separated in the vector space spanned by the PC basis set. Figure 5.3.3 show the result of PCA on the raw data sets after mean-centering, which resulted in 87.52 % of the variability explained from three PCs. The figure shows a relatively good separation between the membranes, although with some overlap. In conclusion we presented the first mid-IR transmission absorption spectra for clean and fouled PES UF membranes, and made plausible the possibility of separating individual sheets based on PCA analysis of the raw data, which for now is sufficient for a proof-of-principle demonstration.

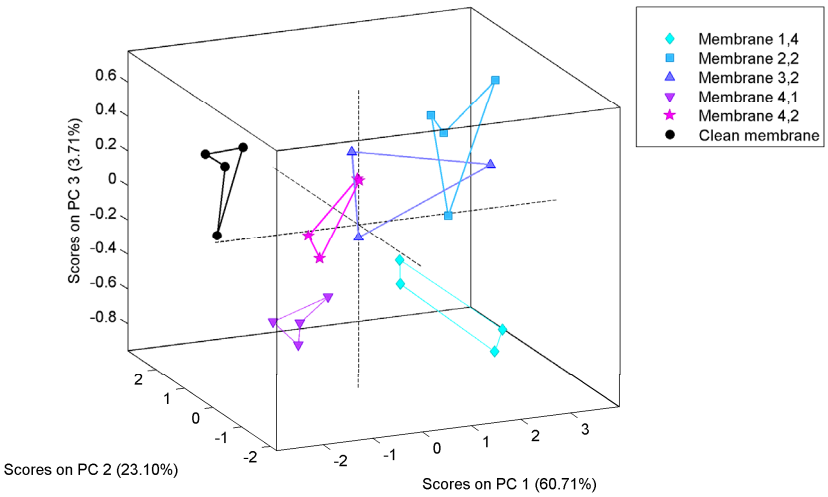

Figure 5.3.3: Principle component analysis of raw UF membrane data. The PCs 1-3 account of 87.52 % of the spectral variability, and the loadings show a fair separation between the sheets, although with some overlap. (Calculations performed by Tine Ringsted).

5.4 LIQUID MILK

It was hinted in the introduction of Chapter 1 that liquid milk was especially difficult to measure throughout the entire mid-IR region, due to strong water absorption near e.g. the amide I band (1650 cm^{-1}). This issue is visualized Figure 5.4.1, which show a region of missing spectral data around the 1650 cm^{-1} water band. This section presents our efforts in trying to penetrate the water band for measuring a continuous spectrum of milk in the mid-IR.

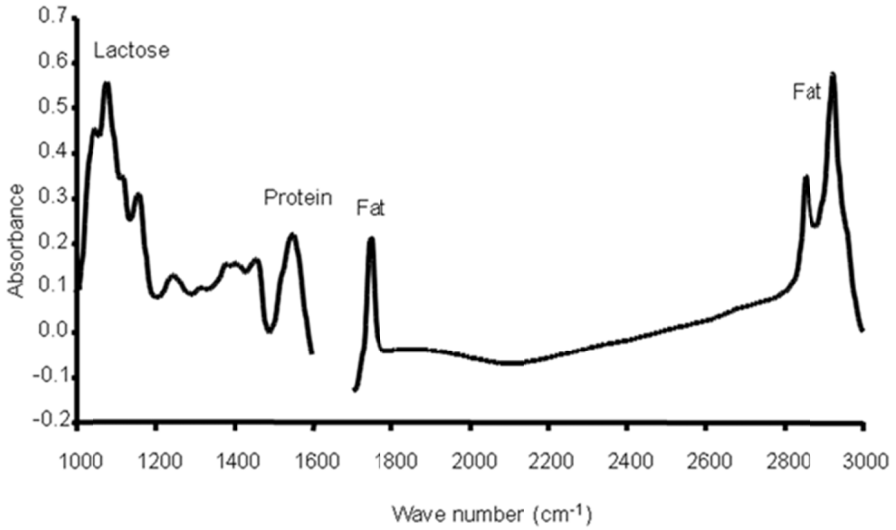

Figure 5.4.1: Standard milk spectrum measured with 38 µm path length transmission cell. Provided by Thomas Nikolajsen from FOSS.

For the measurements a standard transmission cell with 38 µm path length was kindly provided by FOSS (see Figure 5.4.2(a)), which could be filled and emptied using a system of tubes and a syringe (see Figure 5.4.2(b)). The cell was equipped with calcium fluoride windows of about 1 cm clear aperture, and was placed either before the monochromator or before the FTIR fiber probe.

To test the feasibility of this application, the spectrum of pure water was measured, and the result is seen Figure 5.4.3. It is apparent from the figure that the heavily modulated spectrum of the source resulted in a heavily modulated water peak spectrum, but there was still a readable signal.

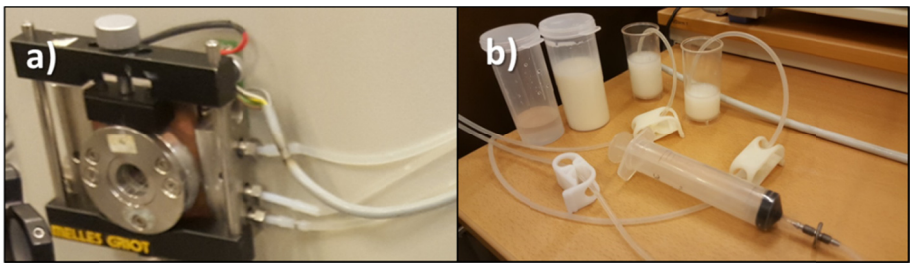

Figure 5.4.2: (a) Liquid transmission cell with 38 µm path length from FOSS. (b) Display of the tubes, canisters, and syringes used for filling and emptying the cell.

The water spectrum was measured using the monochromator and MCT detector setup. However, since milk contains particles that scatter light, it was decided that in order to increase the signal as much as possible, the fiber-coupled FTIR was placed right after the transmission cell. The measurements of milk was done by first measuring ten background spectra of water, then ten spectra of skimmed milk, ten water spectra, ten light milk spectra, ten water spectra again, and finally ten whole fat milk spectra.

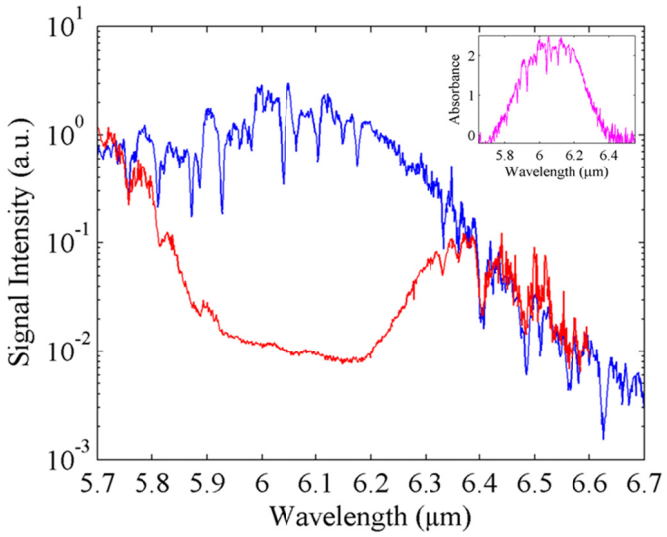

Figure 5.4.3: Measured signal of the SC source with an empty transmission cell (blue), and with the cell filled with de-ionized water (red). The inset shows absorption spectrum obtained from subtraction of the two. It is important to notice that the signal did not completely disappear, although the water spectrum was affected by the heavy modulation of the SC spectrum.

Obviously the time between measurement of the reference and sample spectra could cause additional noise due to spectral drift, and even though the cell was flushed with water in between milk samples, it is possible that milk residuals, especially fat, could influence subsequent measurements. Figure 5.4.4 show the results of the three different milk samples superimposed on the milk spectrum from Figure 5.4.1, which shows heavy influence by noise. The C=O fat peak at 1750 cm^{-1} was very well resolved and consistent with the fat content of each sample. The peak of the amide II band at 1550 cm^{-1} was relatively consistent, which was to be expected since the protein content of all three samples should be the same. The features between 1350-1500 cm-1 was in qualitative agreement with the reference milk spectrum, but the remaining features, and especially the amide I band at 1650 cm^{-1}, was too noisy to perform any meaningful analysis.

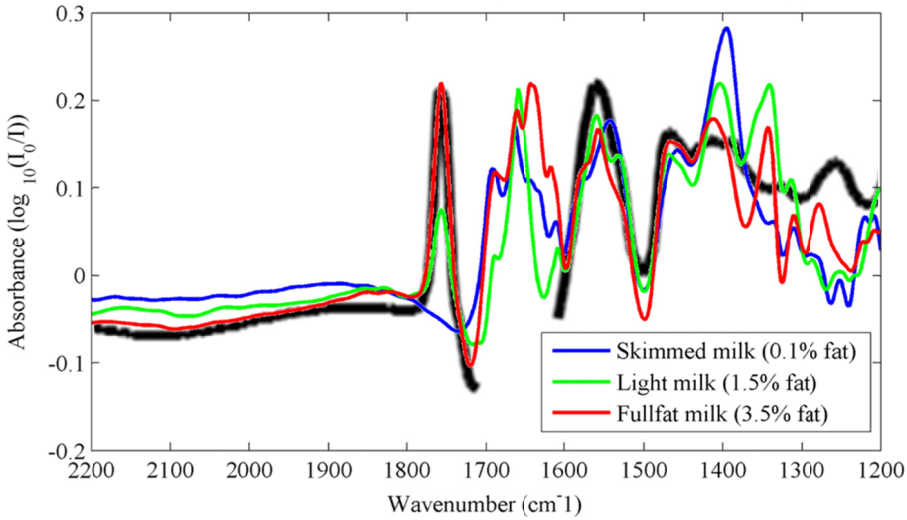

Figure 5.4.4: Spectra for skimmed, light, and whole fat milk superimposed on a standard milk spectrum. The fat peak at 1750 cm^{-1} correlates well with the difference in fat between the three samples.

One issue with this application is that it does not utilize the strengths of SC sources, since the broad bandwidth of the source results in parts of the spectrum saturating the detector, while the signal from the water band is barely above the noise floor. For the specific application of penetrating the 1650 cm^{-1} water band QCLs can provide a much higher PSD, as shown in Figure 5.2.2, and measurement of the amide I band has al-

ready been demonstrated in aqueous solutions [7]. Possible ways of optimizing the experiment includes keeping the milk and water thermostatic, to avoid changes in absorption features due to the temperature, and adding a bandpass filter for the target region to avoid saturation of the detector outside the absorption region. One practical optimization would be to employ a dual-beam configuration for simultaneous reference measurements, which should improve the signal-to-noise ratio greatly, while avoiding any errors in the reference measurement due milk remnants in the cell.

Chapter

6 Conclusion and Outlook

- "I may not have gone where I intended to go, but I think I have ended up where I needed to be."

- Douglas Adams, The Long Dark Tea-Time of the Soul

I set out in this PhD Project "Light and Food" with the goal of developing a mid-IR SC source which could be used in various practical applications, for example within the food industry. The task was initially to build upon the mid-IR platform from NKT Photonics based on ZBLAN fibers, and during this endeavor we discovered the presence of a 2nd ZDW in the ZBLAN fibers used by NKT Photonics, which therefore rendered them unsuitable for cascaded SCG. We proceeded to demonstrate experimentally the difference in the efficiency of the cascaded SCG scheme if a different fiber with a more suitable dispersion profile was chosen. This was the first ever demonstration of cascaded SCG reaching beyond 5 μm in chalcogenide fibers. In demonstrating this we have laid the foundation for developing an all-fiber chalcogenide mid-IR SC source, which could be transported to other research labs for testing in various applications, thus making the technology more available, visible, and the context of commercialization more viable.

In the project we have benefitted tremendously from our strong collaboration with various national and international universities and companies. Our collaboration with Nottingham University resulted in a record SC bandwidth obtained using their high quality chalcogenide fibers - a result which was published in Nature Photonics. From collaboration with Heriot-Watt University we also got our hands on ULI GLS waveguides, which is an exciting technology with many potential appli-

cations within mid-IR devices, and our joint efforts also resulted in a journal publication. In collaboration with Australian National University we also demonstrated the, at that time, highest average output power above 5 μm from a chalcogenide fiber. Since then there have been several demonstrations of higher average power from ANU, and in that respect the results in this work on SCG in tapered fibers is placed among the state of the art in terms of long-wavelength average power.

The nanoimprint idea started out as a small side project of mine, which eventually ended up as a complete Ph.D. project for Mikkel Lotz at DTU Nanotech. I built the setup from scratch, and learned a lot in the process about material science and thermo-electrical systems. In the end it resulted in a lot of beautiful pictures, and more importantly in a proof-of-concept experiment demonstrating the anti-reflective properties of the imprinted structures in chalcogenide fibers.

Another goal of the project was to identify and demonstrate potential applications for mid-IR SC sources, which proved to be a major challenge. We performed proof-of-concept demonstrations of spectroscopy on skin, milk, and milk filtration membranes, which showed some potential, but the real golden application was not found. One application that we are confident will be a success for mid-IR SC sources is OCT for non-destructive testing, but such an advanced application requires significant work and instrumentation, which was outside the scope of the project. This OCT application is the subject of another Innovation Fund Denmark project called “ShapeOCT”, in which I will take part as a post.doc. upon completion of this work.

Appendix

A

State of the Art in mid-IR Supercontinuum

Appendix A includes the details of the state of the art SC results plotted in Figure 4.1.1. The long-wavelength edge (λ_{edge}), 30 dB bandwidth (BW_{30dB}) were evaluated from published figures. In the cases where the total output power (P_{tot}) was not supplied, it was ither calculated or estimated from other reported values.

Nonlinear fiber	λ_{edge} (μm)	BW_{30dB} (μm)	P_{tot} (mW)	λ_p (μm)	Pump type	Ref.
15 μm SIF As_2Se_3/$AsSe_2$	15.10	13.10	<0.3[b]	9.8	MW	[130]
16 μm SIF As_2Se_3/ $Ge_{10}As_{23.4}Se_{66.6}$	13.30	11.90	0.15	6.3	MW	[37]
7 μm SIF GeSbSe/GeAsSe	11.79	8.79	9.0[c]	4.6	kW	[167]
23 μm SIF ($Ge_{15}Sb_{25}Se_{60}$/ $Ge_{15}Sb_{20}Se_{65}$)	11.36	9.02	<0.1[b]	6.0	MW	[168]
6 μm SIF $Ge_{15}Sb_{15}Se_{70}$/ $Ge_{20}Se_{80}$	11.08	8.77	17	4.5	kW	[132]
27 μm SIF As_2Se_3/As_2S_5	10.00	7.00	0.65	7.0	MW	[169]
4.1/4.6 μm SIF $Ge_{12}As_{24}Se_{64}$/$Ge_{10}As_{24}S_{66}$	9.91	8.26	1.26	4.0	kW	[67]
4/4.4 μm RWG $Ge_{11.5}As_{24}Se_{64.5}$/ $Ge_{11.5}As_{24}S_{64.5}$	9.24	6.97	20.0	4.2	kW	[154]
11.6→6 μm tapered PCF $Ge_{10}As_{22}Se_{68}$	8.68	6.83	41.5	4.0	kW	This work
18 μm As_2Se_3 SIF	8.03	5.03	1.50	3.0-4.2	Casc.	[170]
4 μm RWG $Ge_{11.5}As_{24}Se_{64.5}$ /$Ge_{11.5}As_{24}S_{64.5}$	8.00	6.42	20.0	4.0	kW	[131]
12.4→7.2 μm tapered PCF $Ge_{10}As_{22}Se_{68}$	7.91	5.87	54.8	4.0	kW	This work
12.4→7.2 μm tapered PCF $Ge_{10}As_{22}Se_{68}$	7.63	5.38	9.0	3.5-4.4	Casc.	This work

4.5 µm $As_{38}Se_{62}$ SCF	7.60	5.90	15.6	4.4	kW	[82]
12.4 µm $Ge_{10}As_{22}Se_{68}$ PCF	7.49	4.49	49.5	4.3	kW	This work
100 µm SIF As_2S_3	7.00	1.50	0.3[b]	3.9	MW	[171]
4.5 µm $As_{38}Se_{62}$ SCF	6.94	4.14[a]	6.5	3.5-4.4	Casc.	[121]
12.4 $Ge_{10}As_{22}Se_{68}$ PCF	6.86	3.76	54.5	3.5-4.4	Casc.	[149]
9 µm As_2S_3 SIF	6.40	4.81	8.0	3.1	kW	[172]
9 µm As_2S_3 SIF	5.00	2.20	550	3.8	kW	[173]
11.5 µm $As_{38}Se_{62}$ PCF	4.95	1.85	20	3-4.2	Casc.	[174]
10 µm SIF As_2S_3	4.80	2.90	565	2.4-2.5	Casc.	[114]

Table 4: State of the art in mid-IR SCG in chalcogenide fibers sorted by long-wavelength edge (λ_{edge}). BW_{30dB}: 30 dB bandwidth, P_{tot}: Total average output power, λ_p: Pump wavelength, RWG: Rib waveguide, SCF: suspended-core fiber, SIF: step-index fiber, WG: waveguide. a: Limited by detector b: Estimated. -30 dB edge. c: Data from personal correspondence with the author Yi Yu.

References

1. D.-W. Sun, *Infrared Spectroscopy for Food Quality Analysis and Control*, 1st ed, (Academic Press, n.d.).
2. L. B. Mostaço-Guidolin, L. S. Murakami, A. Nomizo, and L. Bachmann, "Fourier Transform Infrared Spectroscopy of Skin Cancer Cells and Tissues," Appl. Spectrosc. Rev. **44**, 438–455 (2009).
3. M. J. Walsh, M. J. German, M. Singh, H. M. Pollock, A. Hammiche, M. Kyrgiou, H. F. Stringfellow, E. Paraskevaidis, P. L. Martin-Hirsch, and F. L. Martin, "IR microspectroscopy: potential applications in cervical cancer screening," Cancer Lett. **246**, 1–11 (2007).
4. C. Hughes and M. J. Baker, "Can mid-infrared biomedical spectroscopy of cells, fluids and tissue aid improvements in cancer survival? A patient paradigm," Analyst **141**, 467–475 (2015).
5. R. K. Sahu, S. Argov, A. Salman, M. Huleihel, N. Grossman, Z. Hammody, J. Kapelushnik, and S. Mordechai, "Characteristic absorbance of nucleic acids in the Mid-IR region as possible common biomarkers for diagnosis of malignancy.," Technol. Cancer Res. Treat. **3**, 629–638 (2004).
6. A. Dong, P. Huang, and W. S. Caughey, "Protein secondary structures in water from second-derivative amide I infrared spectra.," Biochemistry **29**, 3303–3308 (1990).
7. M. R. Alcaráz, A. Schwaighofer, H. Goicoechea, and B. Lendl, "EC-QCL mid-IR transmission spectroscopy for monitoring dynamic changes of protein secondary structure in aqueous solution on the example of β-aggregation in alcohol-denaturated α-chymotrypsin," Anal. Bioanal. Chem. **408**, 3933–3941 (2016).
8. M. Carbonaro and a. Nucara, "Secondary structure of food proteins by Fourier transform spectroscopy in the mid-infrared region," Amino Acids **38**, 679–690 (2010).
9. N. Cezard, A. Dobroc, G. Canat, M. Duhant, W. Renard, C. Alhenc-Gelas, S. Lefebvre, and J. Fade, "Supercontinuum laser absorption spectroscopy in the mid-infrared range for identification and concentration estimation of a multi- component atmospheric gas mixture," Proc. SPIE - Int. Soc. Opt. Eng. **8182**, (2011).
10. M. G. Allen, "Diode laser absorption sensors for gas-dynamic and combustion flows," Meas. Sci. Technol. **9**, 545–562 (1998).
11. E. Domingo, A. A. Tirelli, C. A. Nunes, M. C. Guerreiro, and S. M. Pinto, "Melamine detection in milk using vibrational spectroscopy and chemometrics analysis: A review," Food Res. Int. **60**, 131–139 (2014).
12. J. Wegener, R. H. Wilson, and H. S. Tapp, "Mid-infrared spectroscopy for food analysis : recent new applications and relevant developments in sample presentation methods," Trends Anal. Chem. **18**, 85–93 (1999).
13. R. N. M. Páscoa, J. ATLopes, and J. L. F. C. Lima, "In situ near infrared monitoring of activated dairy sludge wastewater treatment processes," J. Near Infrared Spectrosc. **16**, 409–419 (2008).
14. J. K. Jensen, N. Ottosen, S. B. Engelsen, and F. van den Berg,

"Investigation of UF and MF Membrane Residual Fouling in Full-Scale Dairy Production Using FT-IR to Quantify Protein and Fat," Int. J. Food Eng. **11**, 1–15 (2015).

15. R. H. Wilson, B. J. Goodfellow, P. S. Belton, B. G. Osborne, G. Oliver, and P. L. Russell, "Comparison of fourier transform mid infrared spectroscopy and near infrared reflectance spectroscopy with differential scanning calorimetry for the study of the staling of bread," J. Sci. Food Agric. **54**, 471–483 (1991).
16. T. Ringsted, S. Dupont, J. Ramsay, B. M. Jespersen, K. M. Sorensen, S. R. Keiding, and S. B. Engelsen, "Near-Infrared Spectroscopy Using a Supercontinuum Laser: Application to Long Wavelength Transmission Spectra of Barley Endosperm and Oil," Appl. Spectrosc. **70**, 1176–1185 (2016).
17. J. Haas and B. Mizaikoff, "Advances in Mid-Infrared Spectroscopy for Chemical Analysis," Annu. Rev. Anal. Chem. **9**, 45–68 (2016).
18. M. L. Brandily, V. Monbet, B. Bureau, C. Boussard-Plédel, O. Loréal, J. L. Adam, and O. Sire, "Identification of foodborne pathogens within food matrices by IR spectroscopy," Sensors Actuators, B Chem. **160**, 202–206 (2011).
19. C. Heuer, H. J. Luinge, E. T. Lutz, Y. H. Schukken, J. H. van der Maas, H. Wilmink, and J. P. Noordhuizen, "Determination of acetone in cow milk by Fourier transform infrared spectroscopy for the detection of subclinical ketosis.," J. Dairy Sci. **84**, 575–582 (2001).
20. D. Segelstein, "The Complex Refractive Index of Water (M.Sc. Thesis)," University of Missouri, Kansas City (1981).
21. P. Bassan, M. J. Weida, J. Rowlette, and P. Gardner, "Large scale infrared imaging of tissue micro arrays (TMAs) using a tunable Quantum Cascade Laser (QCL) based microscope.," Analyst **139**, 3856–3859 (2014).
22. C. S. Colley, J. C. Hebden, D. T. Delpy, A. D. Cambrey, R. A. Brown, E. A. Zibik, W. H. Ng, L. R. Wilson, and J. W. Cockburn, "Mid-infrared optical coherence tomography," Rev. Sci. Instrum. **78**, (2007).
23. J. Kottmann, J. M. Rey, J. Luginbühl, E. Reichmann, and M. W. Sigrist, "Glucose sensing in human epidermis using mid-infrared photoacoustic detection," Biomed. Opt. Express **3**, 667 (2012).
24. I. D. Lindsay, S. Valle, J. Ward, G. Stevens, M. Farries, L. Huot, C. Brooks, P. M. Moselund, R. M. Vinella, M. Abdalla, D. de Gaspari, R. M. von Wurtemberg, S. Smuk, H. Martijn, J. Nallala, N. Stone, C. Barta, R. Hasal, U. Moller, O. Bang, S. Sujecki, and A. Seddon, "Towards supercontinuum-driven hyperspectral microscopy in the mid-infrared," SPIE BiOS **9703**, 970304 (2016).
25. Y. Sun, C. F. Booker, S. Kumari, R. N. Day, M. Davidson, and A. Periasamy, "Characterization of an orange acceptor fluorescent protein for sensitized spectral fluorescence resonance energy transfer microscopy using a white-light laser," J. Biomed. Opt. **14**, 1–11 (2009).
26. P. Cimalla, J. Walther, M. Mittasch, and E. Koch, "Shear flow-induced optical inhomogeneity of blood assessed in vivo and in vitro by spectral domain optical coherence tomography in the 1.3 μm wavelength range,"

J. Biomed. Opt. **16**, 1–11 (2011).
27. K. K. Chu, C. Unglert, T. N. Ford, D. Cui, R. W. Carruth, K. Singh, L. Liu, S. E. Birket, G. M. Solomon, S. M. Rowe, and G. J. Tearney, "In vivo imaging of airway cilia and mucus clearance with micro-optical coherence tomography," Biomed. Opt. Express **7**, 2494 (2016).
28. J. He, J. Miyazaki, N. Wang, H. Tsurui, and T. Kobayashi, "Label-free imaging of melanoma with nonlinear photothermal microscopy," Opt. Lett. **40**, 1141–1144 (2015).
29. F. L. Pedrotti, L. M. Pedrotti, and L. . Pedrotti, *Introduction to Optics*, 3rd ed. (2007).
30. M. Fox, *Optical Properties of Solids* (2010).
31. P. J. Larkin, *Infrared and Raman Spectroscopy; Principles and Spectral Interpretation* (2011).
32. N. Colthup, *Introduction to Infrared and Raman Spectroscopy* (1975).
33. G. P. Agrawal, *Nonlinear Fiber Optics Fifth Edition Nonlinear Fiber Optics*, 5th editio (Academic Press, 2013).
34. H. G. Dantanarayana, N. Abdel-Moneim, Z. Tang, L. Sojka, S. Sujecki, D. Furniss, A. B. Seddon, I. Kubat, O. Bang, and T. M. Benson, "Refractive index dispersion of chalcogenide glasses for ultra-high numerical-aperture fiber for mid-infrared supercontinuum generation," Opt. Mater. Express **4**, 1444 (2014).
35. M. D. Nielsen, G. Vienne, J. R. Folkenberg, and A. Bjarklev, "Investigation of microdeformation-induced attenuation spectra in a photonic crystal fiber.," Opt. Lett. **28**, 236–238 (2003).
36. R. W. Boyd, *Nonlinear Optics*, 3rd ed. (Academic Press, 2008).
37. C. R. Petersen, U. Møller, I. Kubat, B. Zhou, S. Dupont, J. Ramsay, T. Benson, S. Sujecki, N. Abdel-Moneim, Z. Tang, D. Furniss, A. Seddon, and O. Bang, "Mid-infrared supercontinuum covering the 1.4–13.3 μm molecular fingerprint region using ultra-high NA chalcogenide step-index fibre," Nat. Photonics **8**, 830–834 (2014).
38. P. F. Moulton, G. A. Rines, E. V. Slobodtchikov, K. F. Wall, G. Frith, B. Samson, and A. L. G. Carter, "Tm-doped fiber lasers: Fundamentals and power scaling," IEEE J. Sel. Top. Quantum Electron. **15**, 85–92 (2009).
39. B. E. A. Saleh and M. C. Teich, *Fundamentals of Photonics*, 2nd ed. (Wiley, 2007).
40. G. P. Agrawal, *Fiber-Optic Communication Systems*, 4th ed. (Wiley, 2010).
41. A. Bjarklev, J. Broeng, and A. S. Bjarklev, *Photonic Crystal Fibres* (Springer, 2003).
42. J. M. Dudley, G. Genty, and S. Coen, "Supercontinuum generation in photonic crystal fiber," Rev. Mod. Phys. **78**, 1135–1184 (2006).
43. J. Hansryd, P. a. Andrekson, M. Westlund, and P.-O. Hedekvist, "Fiber-based optical parametric amplifiers and their applications," IEEE J. Sel. Top. Quantum Electron. **8**, 506–520 (2002).
44. S.-W. Xu, R.-P. Wang, Z.-Y. Yang, L. Wang, and L.-D. Barry, "Homopolar bonds in Se-rich Ge–As–Se chalcogenide glasses," Chinese Phys. B **25**, 057105 (2016).
45. J. Herrmann, U. Griebner, N. Zhavoronkov, a. Husakou, D. Nickel, J. C. Knight, W. J. Wadsworth, P. S. J. Russell, and G. Korn, "Experimental

Evidence for Supercontinuum Generation by Fission of Higher-Order Solitons in Photonic Fibers," Phys. Rev. Lett. **88**, 173901 (2002).

46. P. Beaud, W. Hodel, B. Zysset, and H. P. Weber, "Ultrashort Pulse Propagation, Pulse Breakup, and Fundamental Soliton Formation in a Single-Mode Optical Fiber," J. Quantum Electron. **23**, 1938–1946 (1987).
47. A. V. Gorbach and D. V. Skryabin, "Light trapping in gravity-like potentials and expansion of supercontinuum spectra in photonic-crystal fibres," Nat. Photonics **1**, 653–657 (2007).
48. B. Bureau, C. Boussard, S. Cui, R. Chahal, M. L. Anne, V. Nazabal, O. Sire, O. Loréal, P. Lucas, V. Monbet, J.-L. Doualan, P. Camy, H. Tariel, F. Charpentier, L. Quetel, J.-L. Adam, and J. Lucas, "Chalcogenide optical fibers for mid-infrared sensing," Opt. Eng. **53**, 027101 (2014).
49. G. S. Athanasiou, J. Ernst, D. Furniss, T. M. Benson, J. Chauhan, J. Middleton, C. Parmenter, M. Fay, N. Neate, V. Shiryaev, M. F. Churbanov, and A. B. Seddon, "Toward Mid-Infrared, Subdiffraction, Spectral-Mapping of Human Cells and Tissue: SNIM (Scanning Near-Field Infrared Microscopy) Tip Fabrication," J. Light. Technol. **34**, 1212–1219 (2016).
50. A. B. Seddon, "A Prospective for New Mid-Infrared Medical Endoscopy Using Chalcogenide Glasses," Int. J. Appl. Glas. Sci. **2**, 177–191 (2011).
51. L. Huot, P. Moselund, P. Tidemand-lichtenberg, L. Leick, and C. Pederse, "Upconversion imaging using an all-fiber," Opt. Lett. **41**, 2466–2469 (2016).
52. S. Hocdé, O. Loréal, O. Sire, C. Boussard-Plédel, B. Bureau, B. Turlin, J. Keirsse, P. Leroyer, and J. Lucas, "Metabolic imaging of tissues by infrared fiber-optic spectroscopy: an efficient tool for medical diagnosis.," J. Biomed. Opt. **9**, 404–7 (2004).
53. A. B. Seddon, T. M. Benson, S. Sujecki, N. Abdel-Moneim, Z. Tang, D. Furniss, L. Sojka, N. Stone, N. Jayakrupakar, G. R. Lloyd, and others, "Towards the mid-infrared optical biopsy," SPIE BiOS **9703**, 970302 (2016).
54. B. J. Eggleton, B. Luther-Davies, and K. Richardson, "Chalcogenide photonics," Nat. Photonics **5**, 141–148 (2011).
55. G. Tao, H. Ebendorff-Heidepriem, A. M. Stolyarov, S. Danto, J. V. Badding, Y. Fink, J. Ballato, and A. F. Abouraddy, "Infrared fibers," Adv. Opt. Photonics **7**, 379–458 (2015).
56. E. A. Romanova, Y. S. Kuzyutkina, A. I. Konyukhov, N. Abdel-Moneim, A. B. Seddon, T. M. Benson, S. Guizard, and A. Mouskeftaras, "Nonlinear optical response and heating of chalcogenide glasses upon irradiation by the ultrashort laser pulses," Opt. Eng. **53**, 071812 (2014).
57. R. Kitamura, L. Pilon, and M. Jonasz, "Optical constants of silica glass from extreme ultraviolet to far infrared at near room temperature," Appl. Opt. **46**, 8118 (2007).
58. O. Humbach, H. Fabian, U. Grzesik, U. Haken, and W. Heitmann, "Analysis of OH absorption bands in synthetic silica," J. Non. Cryst. Solids **203**, 19–26 (1996).
59. J. Swiderski, "High-power mid-infrared supercontinuum sources: Current status and future perspectives," Prog. Quantum Electron. **38**,

189–235 (2014).
60. X. Zhu and N. Peyghambarian, "High-power ZBLAN glass fiber lasers: Review and prospect," Adv. Optoelectron. **2010**, (2010).
61. M. Liao, W. Gao, T. Cheng, X. Xue, Z. Duan, D. Deng, H. Kawashima, T. Suzuki, and Y. Ohishi, "Five-octave-spanning supercontinuum generation in fluoride glass," Appl. Phys. Express **6**, 032503 (2013).
62. P. M. Moselund, C. Petersen, L. Leick, J. S. Dam, P. Tidemand-lichtenberg, and C. Pedersen, "Highly Stable , All-fiber , High Power ZBLAN Supercontinuum Source Reaching 4.75 μm used for Nanosecond mid-IR Spectroscopy," in *In Advanced Solid-State Lasers Congress* (2013), p. JTh5A.9.
63. O. P. Kulkarni, V. V Alexander, M. Kumar, M. J. Freeman, M. N. Islam, F. L. Terry, M. Neelakandan, and A. Chan, "Supercontinuum generation from ~1.9 to 4.5 μm in ZBLAN fiber with high average power generation beyond 3.8 μ m using a thulium-doped fiber amplifier," J. Opt. Soc. Am. B **28**, 2486–2498 (2011).
64. V. S. Shiryaev and M. F. Churbanov, "Trends and prospects for development of chalcogenide fibers for mid-infrared transmission," J. Non. Cryst. Solids **377**, 225–230 (2013).
65. R. E. Slusher, G. Lenz, J. Hodelin, J. Sanghera, L. B. Shaw, and I. D. Aggarwal, "Large Raman gain and nonlinear phase shifts in high-purity As2Se3 chalcogenide fibers," J. Opt. Soc. Am. **21**, 1146–1155 (2004).
66. T. Wang, X. Gai, W. Wei, R. Wang, Z. Yang, X. Shen, S. Madden, and B. Luther-Davies, "Systematic z-scan measurements of the third order nonlinearity of chalcogenide glasses," Opt. Mater. Express **4**, 1011 (2014).
67. Y. Yu, B. Zhang, X. Gai, C. Zhai, S. Qi, W. Guo, Z. Yang, R. Wang, D. Choi, S. Madden, and B. Luther-davies, "1.8-10 μm mid-infrared supercontinuum generated in a step-index chalcogenide fiber using low peak pump power," Opt. Lett. **40**, 1081–1084 (2015).
68. P. Toupin, L. Brilland, J. Trolès, and J.-L. Adam, "Small core Ge-As-Se microstructured optical fiber with single-mode propagation and low optical losses," Opt. Mater. Express **2**, 1359 (2012).
69. V. Q. Nguyen, J. S. Sanghera, F. H. Kung, P. C. Pureza, and I. D. Aggarwal, "Very large temperature-induced absorptive loss in high Te-containing chalcogenide fibers," J. Light. Technol. **18**, 1395–1401 (2000).
70. Z. G. Lian, W. Pan, D. Furniss, T. M. Benson, A. B. Seddon, T. Kohoutek, J. Orava, and T. Wagner, "Embossing of chalcogenide glasses: monomode rib optical waveguides in evaporated thin films.," Opt. Lett. **34**, 1234–1236 (2009).
71. J. Orava, T. Kohoutek, a L. Greer, and H. Fudouzi, "Soft imprint lithography of a bulk chalcogenide glass," Opt. Mater. Express **1**, 796–802 (2011).
72. S. Danto, E. Koontz, Y. Zou, T. O. Ogbuu, B. Gleason, P. Wachtel, J. D. Musgraves, J. Hu, and K. Richardson, "Nanoscale optical features via hot-stamping of As 2 Se 3 glass," SPIE Optifab **8884**, 88841T (2013).
73. T. Kohoutek, J. Orava, and H. Fudouzi, "Soft-mould imprinting of chalcogenide glasses," in *Advanced Architectures in Photonics* (2014),

Vol. 1, pp. 9–10.
74. C. Florea, J. Sanghera, L. Busse, B. Shaw, and I. Aggarwal, "Improved laser damage threshold for chalcogenide glasses through surface microstructuring," **7946**, 794610–794610–8 (2011).
75. B. D. MacLeod, D. S. Hobbs, and E. Sabatino III, "Moldable AR microstructures for improved laser transmission and damage resistance in CIRCM fiber optic beam delivery systems," 80160Q–80160Q–14 (2011).
76. C. Florea, J. Sanghera, L. Busse, B. Shaw, F. Miklos, and I. Aggarwal, "Reduced Fresnel losses in chalcogenide fibers obtained through fiber-end microstructuring.," Appl. Opt. **50**, 17–21 (2011).
77. C. Agger, C. Petersen, S. Dupont, H. Steffensen, J. K. Lyngso, C. Thomsen, S. Keiding, and O. Bang, "ZBLAN supercontinuum generation - Detailed comparison between measurement and simulation," J. Opt. Soc. Am. B **29**, 635–644 (2012).
78. Z. G. Lian, Q. Q. Li, D. Furniss, T. M. Benson, and A. B. Seddon, "Solid microstructured chalcogenide glass optical fibers for the near- and mid-infrared spectral regions," IEEE Photonics Technol. Lett. **21**, 1804–1806 (2009).
79. C. Caillaud, G. Renversez, L. Brilland, D. Mechin, L. Calvez, J. L. Adam, and J. Troles, "Photonic bandgap propagation in all-solid chalcogenide optical fibers," Materials (Basel). **7**, 6120–6129 (2014).
80. G. Demetriou, J.-P. Bérubé, R. Vallée, Y. Messaddeq, C. R. Petersen, D. Jain, O. Bang, C. Craig, D. W. Hewak, and A. K. Kar, "Refractive index and dispersion control of ultrafast laser inscribed waveguides in gallium lanthanum sulphide for near and mid-infrared applications," Opt. Express **24**, 6350–6358 (2016).
81. J. Requejo-Isidro, A. K. Mairaj, V. Pruneri, D. W. Hewak, M. C. Netti, and J. J. Baumberg, "Self refractive non-linearities in chalcogenide based glasses," J. Non. Cryst. Solids **317**, 241–246 (2002).
82. U. Møller, Y. Yu, I. Kubat, C. R. Petersen, X. Gai, L. Brilland, D. Méchin, C. Caillaud, J. Troles, B. Luther-Davies, and O. Bang, "Multi-milliwatt mid-infrared supercontinuum generation in a suspended core chalcogenide fiber," Opt. Express **23**, 3282–3291 (2015).
83. R. Salem, Z. Jiang, D. Liu, R. Pafchek, D. Gardner, P. Foy, M. Saad, D. Jenkins, A. Cable, and P. Fendel, "Mid-infrared supercontinuum generation spanning 1.8 octaves using step-index indium fluoride fiber pumped by a femtosecond fiber laser near 2 μm," Opt. Express **23**, 30592 (2015).
84. J. Troles, L. Brilland, P. Toupin, Q. Coulombier, S. D. Le, D. M. Nguyen, M. Thual, and T. Chartier, "Chalcogenide Suspended-Core Fibers: Manufacturing and Non-Linear Properties at 1.55 μm," in *ICTON, IEEE, We.B6.2* (2011).
85. S. Xing, D. Grassani, S. Kharitonov, A. Billat, and C.-S. Brès, "Characterization and modeling of microstructured chalcogenide fibers for efficient mid-infrared wavelength conversion," Opt. Express **24**, 9741 (2016).
86. I. Shavrin, S. Novotny, and H. Ludvigsen, "Mode excitation and

supercontinuum generation in a few-mode suspended-core fiber," Opt. Express **21**, 32141–32150 (2013).
87. I. Kubat and O. Bang, "Multimode supercontinuum generation in chalcogenide glass fibres," Opt. Express **24**, 2513 (2016).
88. F. Poletti and P. Horak, "Dynamics of femtosecond supercontinuum generation in multimode fibers," Opt. Express **17**, 11301–11312 (2009).
89. C. W. Rudy, A. Marandi, K. L. Vodopyanov, and R. L. Byer, "Octave-spanning supercontinuum generation in in situ tapered As2S3 fiber pumped by a thulium-doped fiber laser," Opt. Lett. **38**, 2865–8 (2013).
90. A. Marandi, C. W. Rudy, V. G. Plotnichenko, E. M. Dianov, K. L. Vodopyanov, and R. L. Byer, "Mid-infrared supercontinuum generation in tapered chalcogenide fiber for producing octave-spanning frequency comb around 3 μm," Opt. Express **20**, 24218–24225 (2012).
91. N. Granzow, M. A. Schmidt, W. Chang, L. Wang, Q. Coulombier, J. Troles, P. Toupin, I. Hartl, K. F. Lee, M. E. Fermann, L. Wondraczek, and P. S. J. Russell, "Mid-infrared supercontinuum generation in As2S3 -silica "nano-spike" step-index waveguide," Opt. Express **21**, 1596–1603 (2013).
92. S. Shabahang, G. Tao, M. P. Marquez, H. Hu, T. R. Ensley, P. J. Delfyett, and A. F. Abouraddy, "Nonlinear characterization of robust multimaterial chalcogenide nanotapers for infrared supercontinuum generation," J. Opt. Soc. Am. B **31**, 450 (2014).
93. A. Al-kadry, C. Baker, M. El Amraoui, Y. Messaddeq, and M. Rochette, "Broadband supercontinuum generation in As2Se3 chalcogenide wires by avoiding the two-photon absorption effects.," Opt. Lett. **38**, 1185–7 (2013).
94. I. Kubat, C. S. Agger, P. M. Moselund, and O. Bang, "Mid-infrared supercontinuum generation to 4.5 μm in uniform and tapered ZBLAN step-index fibers by direct pumping at 1064 or 1550 nm," J. Opt. Soc. Am. B **30**, 2743–2757 (2013).
95. G. Renversez, M. Duhant, W. Renard, Q. Coulombier, and J. Trol, "Nonlinear effects above 2 μm in chalcogenide suspended core microstructured optical fibers: modeling and experiments," in *PHO, IEEE* (2011), pp. , 61–62.
96. T. Grósz, A. P. Kovács, M. Kiss, and R. Szip, "Measurement of higher order chromatic dispersion in a photonic bandgap fiber : comparative study of spectral interferometric methods," Appl. Opt. **53**, 1929–1937 (2014).
97. G. M. Ponzo, M. N. Petrovich, X. Feng, P. Horak, F. Poletti, P. Petropoulos, and D. J. Richardson, "Fast and broadband fiber dispersion measurement with dense wavelength sampling," Opt. Express **22**, 943 (2014).
98. P. Hlubina, "Spectral interferometry-based chromatic dispersion measurement of fibre including the zero-dispersion wavelength," J. Eur. Opt. Soc. Rap. Public. **12017**, 1–5 (2012).
99. P. Hlubina, D. Ciprian, and M. Kadulová, "Wide spectral range measurement of modal birefringence in polarization-maintaining fibres," Meas. Sci. Technol. **20**, 025301 (2009).

100. F. Gan, "Optical properties of fluoride glasses: a review," J. Non. Cryst. Solids **184**, 9–20 (1995).
101. K. M. Davis, K. Miura, N. Sugimoto, and K. Hirao, "Writing waveguides in glass with a femtosecond laser," Opt. Lett. **21**, 1729 (1996).
102. R. R. Thomson, A. S. Bockelt, E. Ramsay, S. Beecher, A. H. Greenaway, A. K. Kar, and D. T. Reid, "Shaping ultrafast laser inscribed optical waveguides using a deformable mirror," Opt. Express **16**, 12786–12793 (2008).
103. J. R. Weiblen, C. M. Florea, L. E. Busse, L. B. Shaw, C. R. Menyuk, I. D. Aggarwal, and J. S. Sanghera, "Irradiance Enhancement and Increased Laser Damage Threshold in As2S3 Motheye Antireflective Structures," Opt. Lett. **40**, 4799–4802 (2015).
104. L. E. Busse, C. Florea, B. Shaw, V. Nguyen, J. S. Sanghera, I. Aggarwal, and F. Kung, "Antireflective surface structures on IR fibers for high power transmission," in *Advanced Solid-State Lasers Congress Technical Digest* (OSA, 2013), p. AM2A.5.
105. Y. Du, X. Wu, M. Zhu, and Z. Le, "Theoretical and experimental research on laser-induced damage of cylindrical subwavelength grating," Opt. Express **23**, 24296–24307 (2015).
106. C. David, E. Deckardt, D. B. Psi, M. Schnieper, J. Söchtig, and C. Z. Csem-z, "Nano-Structured Ar-Surfaces Replicated By Hot Embossing," **21**, 5232–5232 (2001).
107. Y. Kanamori, M. Okochi, and K. Hane, "Fabrication of antireflection subwavelength gratings at the tips of optical fibers using UV nanoimprint lithography.," Opt. Express **21**, 322–8 (2013).
108. Y. J. Yoo, K. S. Chang, S. W. Hong, and Y. M. Song, "Design of ZnS antireflective microstructures for mid- and far-infrared applications," Opt. Quantum Electron. **47**, 1503–1508 (2015).
109. P. B. Corkum, P. P. Ho, R. R. Alfano, and J. T. Manassah, "Generation of infrared supercontinuum covering 3-14 , um in dielectrics and semiconductors," Opt. Lett. **10**, 624–626 (1985).
110. J. J. Pigeon, Y. S. Tochitsky, C. Gong, and C. Joshi, "Supercontinuum generation from 2-20 μm in GaAs pumped by picosecond CO2 laser pulses," Opt. Lett. **39**, 3246–3249 (2014).
111. S. Coen, A. Chau, R. Leonhardt, J. D. Harvey, J. C. Knight, W. J. Wadsworth, and P. S. J. Russell, "Supercontinuum generation by stimulated Raman scattering and parametric four-wave mixing in photonic crystal fibers," J. Opt. Soc. Am. B **19**, 753–764 (2002).
112. L. B. Shaw, P. A. Thielen, F. H. Kung, V. Q. Nguyen, and J. S. Sanghera, "IR Supercontinuum Generation in As-Se Photonic Crystal Fiber," in *OSA/ASSP* (2005), p. TuC5.
113. W. Gao, M. El Amraoui, M. Liao, H. Kawashima, Z. Duan, D. Deng, T. Cheng, T. Suzuki, Y. Messaddeq, and Y. Ohishi, "Mid-infrared supercontinuum generation in a suspended-core As2S3 chalcogenide microstructured optical fiber," Opt. Express **21**, 1071–1075 (2013).
114. R. R. Gattass, L. Brandon Shaw, V. Q. Nguyen, P. C. Pureza, I. D. Aggarwal, and J. S. Sanghera, "All-fiber chalcogenide-based mid-infrared supercontinuum source," Opt. Fiber Technol. **18**, 345–348 (2012).

115. C. Xia, Z. Xu, M. N. Islam, F. L. Terry, M. J. Freeman, A. Zakel, and J. Mauricio, "10.5 W time-averaged power mid-IR supercontinuum generation extending beyond 4 μm with direct pulse pattern modulation," IEEE J. Sel. Top. Quantum Electron. **15**, 422–434 (2009).
116. C. Xia, M. Kumar, M.-Y. Cheng, R. S. Hegde, M. N. Islam, A. Galvanauskas, H. G. Winful, F. L. Terry, M. J. Freeman, M. Poulain, and G. Mazé, "Power scalable mid-infrared supercontinuum generation in ZBLAN fluoride fibers with up to 1.3 watts time-averaged power.," Opt. Express **15**, 865–71 (2007).
117. W. Yang, B. Zhang, K. Yin, X. Zhou, and J. Hou, "High power all fiber mid-IR supercontinuum generation in a ZBLAN fiber pumped by a 2 μm MOPA system," **21**, 19732–19742 (2013).
118. Y. Yu, X. Gai, T. Wang, P. Ma, R. Wang, Z. Yang, D.-Y. Choi, S. Madden, and B. Luther-Davies, "Mid-infrared supercontinuum generation in chalcogenides," Opt. Mater. Express **3**, 1075 (2013).
119. I. Kubat, C. Rosenberg Petersen, U. V. Møller, A. Seddon, T. Benson, L. Brilland, D. Méchin, P. M. Moselund, and O. Bang, "Thulium pumped mid-infrared 0.9–9μm supercontinuum generation in concatenated fluoride and chalcogenide glass fibers," Opt. Express **22**, 3959–3967 (2014).
120. W. Yuan, "2–10 μm mid-infrared supercontinuum generation in As2Se3 photonic crystal fiber," Laser Phys. Lett. **10**, 095107 (2013).
121. C. R. Petersen, P. M. Moselund, C. Petersen, U. Møller, and O. Bang, "Spectral-temporal composition matters when cascading supercontinua into the mid-infrared," Opt. Express **24**, 749–758 (2016).
122. L. Sojka, S. Sujecki, Z. Tang, T. M. Benson, a. B. Seddon, E. Barney, D. Furniss, and E. Beres-Pawlik, "Broadband, mid-infrared emission from Pr3+ doped GeAsGaSe chalcogenide fiber, optically clad," Opt. Mater. (Amst). **36**, 1076–1082 (2014).
123. J. S. Sanghera, L. Brandon Shaw, and I. D. Aggarwal, "Chalcogenide glass-fiber-based mid-IR sources and applications," IEEE J. Sel. Top. Quantum Electron. **15**, 114–119 (2009).
124. J. McCarthy, H. Bookey, S. Beecher, R. Lamb, I. Elder, and a. K. Kar, "Spectrally tailored mid-infrared super-continuum generation in a buried waveguide spanning 1750 nm to 5000 nm for atmospheric transmission," Appl. Phys. Lett. **103**, 151103 (2013).
125. J. H. V. Price, X. Feng, A. M. Heidt, G. Brambilla, P. Horak, F. Poletti, G. Ponzo, P. Petropoulos, M. Petrovich, J. Shi, M. Ibsen, W. H. Loh, H. N. Rutt, and D. J. Richardson, "Supercontinuum generation in non-silica fibers," Opt. Fiber Technol. **18**, 327–344 (2012).
126. J. K. Ranka, R. S. Windeler, and a J. Stentz, "Visible continuum generation in air-silica microstructure optical fibers with anomalous dispersion at 800 nm.," Opt. Lett. **25**, 25–27 (2000).
127. A. M. Heidt, "Efficient Adaptive Step Size Method for the Simulation of Supercontinuum Generation in Optical Fibers," J. Light. Technol. **27**, 3984–3991 (2009).
128. B. Ung and M. Skorobogatiy, "Chalcogenide microporous fibers for linear and nonlinear applications in the mid-infrared," Opt. Express **18**, 650–

653 (2010).
129. A. Schliesser, N. Picqué, and T. W. Hänsch, "Mid-infrared frequency combs," Nat. Photonics **6**, 440–449 (2012).
130. T. Cheng, K. Nagasaka, T. Tuan, X. Xue, M. Matsumoto, H. Tezuka, T. Suzuki, and Y. Ohishi, "Mid-infrared supercontinuum generation spanning 2.0 to 15.1 μm in a chalcogenide step-index fiber," Opt. Lett. **41**, 2117–2120 (2000).
131. Y. Yu, X. Gai, P. Ma, D. Y. Choi, Z. Yang, R. Wang, S. Debbarma, S. J. Madden, and B. Luther-Davies, "A broadband, quasi-continuous, mid-infrared supercontinuum generated in a chalcogenide glass waveguide," Laser Photonics Rev. **798**, 792–798 (2014).
132. B. Zhang, Y. Yu, C. Zhai, S. Qi, Y. Wang, A. Yang, X. Gai, R. Wang, Z. Yang, and B. Luther-Davies, "High Brightness 2.2-12 μm Mid-Infrared Supercontinuum Generation in a Nontoxic Chalcogenide Step-Index Fiber," J. Am. Ceram. Soc. **4**, 1–4 (2016).
133. I. Kubat, C. S. Agger, U. Møller, A. B. Seddon, Z. Tang, S. Sujecki, T. M. Benson, D. Furniss, S. Lamrini, K. Scholle, P. Fuhrberg, B. Napier, M. Farries, J. Ward, P. M. Moselund, and O. Bang, "Mid-infrared supercontinuum generation to 12.5μm in large NA chalcogenide step-index fibres pumped at 4.5μm," Opt. Express **22**, 19169–19182 (2014).
134. J. Troles, Q. Coulombier, G. Canat, M. Duhant, W. Renard, P. Toupin, L. Calvez, G. Renversez, F. Smektala, M. El Amraoui, J. L. Adam, T. Chartier, D. Mechin, and L. Brilland, "Low loss microstructured chalcogenide fibers for large non linear effects at 1995 nm.," Opt. Express **18**, 26647–26654 (2010).
135. M. Chemnitz and M. A. Schmidt, "Single mode criterion - a benchmark figure to optimize the performance of nonlinear fibers," Opt. Express **24**, 16191–16205 (2016).
136. S. Xing, D. Grassani, S. Kharitonov, A. Billat, and C. S. Brès, "Small core Chalcogenide photonic crystal fiber for mid- infrared wavelength conversion : experiment and design," in *CLEO:2016* (2016), p. STh1O.6.
137. P. Toupin, L. Brilland, D. Mechin, J. L. Adam, and J. Troles, "Optical aging of chalcogenide microstructured optical fibers," J. Light. Technol. **32**, 2428–2432 (2014).
138. X. Jiang, N. Y. Joly, M. A. Finger, F. Babic, G. K. L. Wong, J. C. Travers, and P. S. J. Russell, "Deep-ultraviolet to mid-infrared supercontinuum generated in solid-core ZBLAN photonic crystal fibre," Nat. Photonics **9**, 133–139 (2015).
139. J. Swiderski, M. Michalska, and G. Maze, "Mid-IR supercontinuum generation in a ZBLAN fiber pumped by a gain-switched mode-locked Tm-doped fiber laser and amplifier system.," Opt. Express **21**, 7851–7857 (2013).
140. M. N. Islam, "All-fiber designs extend supercontinuum sources into the mid-IR region," Laser Focus World (2012).
141. P. M. Moselund, C. Petersen, S. Dupont, C. Agger, O. Bang, and S. R. Keiding, "Supercontinuum: broad as a lamp, bright as a laser, now in the mid-infrared," in *Proc. SPIE 8381* (2012), Vol. 8381, p. 83811A.
142. R. Al-Mahrous, R. Caspary, and W. Kowalsky, "A Thermal Splicing

Method to Join Silica and Fluoride Fibers With Low Attenuation," J. Light. Technol. **32**, 1669–1673 (2014).
143. R. Thapa, R. R. Gattass, V. Nguyen, G. Chin, D. Gibson, W. Kim, L. B. Shaw, and J. S. Sanghera, "Low-loss , robust fusion splicing of silica to chalcogenide fiber for integrated mid-infrared laser technology development," Opt. Lett. **40**, 5074–5077 (2015).
144. G. Stevens and T. Woodbridge, "Development of Low Loss Robust Soft-glass Fiber Splices," Work. Spec. Opt. Fibers their Appl. **1**, W3.21 (2013).
145. C. Agger, S. T. Sørensen, C. L. Thomsen, S. R. Keiding, and O. Bang, "Nonlinear soliton matching between optical fibers.," Opt. Lett. **36**, 2596–2598 (2011).
146. D. V Skryabin, F. Luan, J. C. Knight, and P. S. J. Russell, "Soliton self-frequency shift cancellation in photonic crystal fibers.," Science **301**, 1705–1708 (2003).
147. F. Biancalana, D. V. Skryabin, and a. V. Yulin, "Theory of the soliton self-frequency shift compensation by the resonant radiation in photonic crystal fibers," Phys. Rev. E - Stat. Nonlinear, Soft Matter Phys. **70**, 1–9 (2004).
148. P. Falk, M. H. Frosz, O. Bang, L. Thrane, P. E. Andersen, A. O. Bjarklev, K. P. Hansen, and J. Broeng, "Broadband light generation at approximately 1300 nm through spectrally recoiled solitons and dispersive waves.," Opt. Lett. **33**, 621–623 (2008).
149. C. R. Petersen, P. M. Moselund, C. Petersen, U. Møller, and O. Bang, "Mid-IR supercontinuum generation beyond 7 μm using a silica-fluoride-chalcogenide fiber cascade," Proc. SPIE **9703**, 97030A (2016).
150. J. He, J. Miyazaki, N. Wang, H. Tsurui, and T. Kobayashi, "Biological imaging with nonlinear photothermal microscopy using a compact supercontinuum fiber laser source.," Opt. Express **23**, 9762–9771 (2015).
151. H. Tu, Y. Liu, D. Turchinovich, M. Marjanovic, J. K. Lyngsø, J. Lægsgaard, E. J. Chaney, Y. Zhao, S. You, W. L. Wilson, B. Xu, M. Dantus, and S. A. Boppart, "Stain-free histopathology by programmable supercontinuum pulses," Nat. Photonics **10**, 534–540 (2016).
152. R. Su, M. Kirillin, E. W. Chang, E. Sergeeva, S. H. Yun, and L. Mattsson, "Perspectives of mid-infrared optical coherence tomography for inspection and micrometrology of industrial ceramics," Opt Express **22**, 15804–15819 (2014).
153. C. a. Michaels, T. Masiello, and P. M. Chu, "Fourier transform spectrometry with a near infrared supercontinuum source," 2009 Conf. Lasers Electro-Optics 2009 Conf. Quantum Electron. Laser Sci. Conf. **63**, 1–2 (2009).
154. Y. Yu, X. Gai, P. Ma, K. Vu, Z. Yang, R. Wang, D.-Y. Choi, S. Madden, and B. Luther-Davies, "Experimental demonstration of linearly polarized 2–10 μm supercontinuum generation in a chalcogenide rib waveguide," Opt. Lett. **41**, 958–961 (2016).
155. J. Kilgus, P. Müller, and M. Brandstetter, "Application of supercontinuum radiation for mid-infrared spectroscopy," in *Proc. of SPIE, Optical Sensing and Detection IV* (2016), p. 98990K.

156. A. Aalto, G. Genty, T. Laurila, and J. Toivonen, "Incoherent broadband cavity enhanced absorption spectroscopy using supercontinuum and superluminescent diode sources," Opt. Express **23**, 25225 (2015).
157. M.-L. Anne, C. Le Lan, V. Monbet, C. Boussard-Plédel, M. Ropert, O. Sire, M. Pouchard, C. Jard, J. Lucas, J. L. Adam, P. Brissot, B. Bureau, and O. Loréal, "Fiber evanescent wave spectroscopy using the mid-infrared provides useful fingerprints for metabolic profiling in humans.," J. Biomed. Opt. **14**, 054033 (2013).
158. P. Lucas, M. A. Solis, D. Le Coq, C. Juncker, M. R. Riley, J. Collier, D. E. Boesewetter, C. Boussard-Plédel, and B. Bureau, "Infrared biosensors using hydrophobic chalcogenide fibers sensitized with live cells," Sensors Actuators, B Chem. **119**, 355–362 (2006).
159. S. MacDonald, K. Michel, D. LeCoq, C. Boussard-Pl??del, and B. Bureau, "Optical analysis of infrared spectra recorded with tapered chalcogenide glass fibers," Opt. Mater. (Amst). **25**, 171–178 (2004).
160. R. O. W. Ang, D. I. T. Ang, G. U. T. Ao, and B. A. L. U. Avies, "High-resolution chalcogenide fiber bundles for infrared imaging," Opt. Lett. **40**, 4384–4387 (2015).
161. M. A. Pleitez, T. Lieblein, A. Bauer, O. Hertzberg, H. von Lilienfeld-Toal, and W. Mäntele, "In Vivo Noninvasive Monitoring of Glucose Concentation in Human Epidermins by Pulsed Mid-Infrared Photoacoustic Spectroscopy," Anal. Chem. **85**, 1013–1020 (2013).
162. J. Nallala, G. R. Lloyd, N. Shepherd, and N. Stone, "High-resolution FTIR imaging of colon tissues for elucidation of individual cellular and histopathological features.," Analyst **141**, 630–639 (2016).
163. M. Farries, J. Ward, S. Valle, G. Stephens, P. Moselund, K. van der Zanden, and B. Napier, "Mid infra-red hyper-spectral imaging with bright super continuum source and fast acousto-optic tuneable filter for cytological applications.," J. Phys. Conf. Ser. **619**, 012032 (2015).
164. S. Dupont, C. Petersen, J. Thøgersen, C. Agger, O. Bang, and S. R. Keiding, "IR microscopy utilizing intense supercontinuum light source," Opt. Express **20**, 4887–92 (2012).
165. A. P. M. Michel, S. Liakat, K. Bors, and C. F. Gmachl, "In vivo measurement of mid-infrared light scattering from human skin," Biomed. Opt. Express **4**, 520–530 (2013).
166. A. Hausmann, P. Sanciolo, T. Vasiljevic, E. Ponnampalam, N. Quispe-Chavez, M. Weeks, and M. Duke, "Direct contact membrane distillation of dairy process streams," Membranes (Basel). **1**, 48–58 (2011).
167. B. Luther-davies, Y. Yu, B. Zhang, X. Gai, C. Zhai, S. Qi, W. Guo, R. Wang, D. Choi, S. Madden, U. Møller, I. Kubat, C. R. Petersen, L. Brilland, M. David, C. Caillaud, J. Troles, and O. Bang, "Mid infrared supercontinuum generation from chalcogenide glass waveguides and fibers," in *NLO* (2015), p. NTu1A.4.
168. H. Ou, S. Dai, P. Zhang, Z. Liu, X. Wang, F. Chen, H. Xu, B. Luo, Y. Huang, and R. Wang, "Ultrabroad supercontinuum generated from a highly nonlinear Ge–Sb–Se fiber," Opt. Lett. **41**, 3201–3204 (2016).
169. D. Deng, L. Liu, T. H. Tuan, Y. Kanou, and M. Matsumoto, "Mid-infrared Supercontinuum Covering 3-10 μm Using a As2Se3 Core and As2S5

Cladding Step-index Chalcogenide Fiber," in *Advanced Solid-State Lasers Conference* (2015), p. ATu2A.32.

170. L.-R. Robichaud, J.-C. Gauthier, V. Fortin, S. Chatigny, J.-F. Couillard, J.-L. Delarosbil, R. Vallée, and M. Bernier, "Supercontinuum Generation up to 8 μm in a Low Loss As2Se3 Step-Index Fiber," in *Advanced Photonics* (2016), p. JW4A.2.
171. F. Théberge, N. Thiré, J.-F. Daigle, P. Mathieu, B. E. Schmidt, Y. Messaddeq, R. Vallée, and F. Légaré, "Multioctave infrared supercontinuum generation in large-core As2S3 fibers," Opt. Lett. **39**, 6474 (2014).
172. D. D. Hudson, M. Baudisch, D. Werdehausen, B. J. Eggleton, and J. Biegert, "1.9 octave supercontinuum generation in a As2S3 step-index fiber driven by mid-IR OPCPA," Opt. Lett. **39**, 5752–5755 (2014).
173. S. Kedenburg, T. Steinle, F. Mörz, A. Steinmann, and H. Giessen, "High-power mid-infrared high repetition-rate supercontinuum source based on a chalcogenide step-index fiber," Opt. Lett. **40**, 2668–2671 (2015).
174. C. Kneis, T. Robin, B. Cadier, L. Brilland, C. Caillaud, J. Troles, I. Manek-Hönninger, M. Eichhorn, and C. Kieleck, "Generation of broadband mid-infrared supercontinuum radiation in cascaded soft-glass fibers," in *Proc. of SPIE* (2016), Vol. 9728, pp. 97282A1–6.